

The Ellipticity of M31 Globular Clusters

by

Laura Marie Markle

B.Sc., York University 1987
B.Ed., York University 1987

A THESIS SUBMITTED IN PARTIAL FULFILLMENT
OF THE REQUIREMENTS FOR THE DEGREE OF
MASTER OF SCIENCE

in the Department
of

Physics and Astronomy

ACCEPTED
CULTY OF GRADUATE STUDIES

We accept this thesis as conforming
to the required standard

DEAN

Dec 05, 1989

Supervisor: Dr. C. J. Pritchett

~~Dr. S. van den Bergh~~

Dr. F. D. A. Hartwick

Dr. J. A. Burke

Dr. T. W. Dingle

Dr. D. Crampton

©Laura Marie Markle, 1989
University of Victoria

*All rights reserved. This thesis may not be reproduced
in whole or in part, by zerography or other means,
without the permission of the author.*



National Library
of Canada

Bibliothèque nationale
du Canada

Canadian Theses Service Service des thèses canadiennes

Ottawa, Canada
K1A 0N4

The author has granted an irrevocable non-exclusive licence allowing the National Library of Canada to reproduce, loan, distribute or sell copies of his/her thesis by any means and in any form or format, making this thesis available to interested persons.

The author retains ownership of the copyright in his/her thesis. Neither the thesis nor substantial extracts from it may be printed or otherwise reproduced without his/her permission.

L'auteur a accordé une licence irrévocable et non exclusive permettant à la Bibliothèque nationale du Canada de reproduire, prêter, distribuer ou vendre des copies de sa thèse de quelque manière et sous quelque forme que ce soit pour mettre des exemplaires de cette thèse à la disposition des personnes intéressées.

L'auteur conserve la propriété du droit d'auteur qui protège sa thèse. Ni la thèse ni des extraits substantiels de celle-ci ne doivent être imprimés ou autrement reproduits sans son autorisation.

ISBN 0-315-62348-9

abstract

Supervisor: Dr. C. J. Pritchett

The ellipticity and orientation of seventeen globular clusters associated with the Andromeda Nebula (M31) have been measured using an isophotal method and a moment method. The measured ellipticities range from 0.024 to 0.212 with a mean value of 0.097 ± 0.017 . No ellipticity variation is observed for these clusters. The M31 globular clusters are flatter than those associated with the Milky Way but their ellipticity distribution resembles that of the Large Magellanic Cloud globulars. The mechanism flattening the M31 globular clusters appears to be axial rotation of a size exceeding that of the Galactic globulars and/or anisotropic velocities of the cluster stars.


Supervisor: Dr. C. J. Pritchett


Dr. S. van den Bergh Dr. F. D. A. Hartwick


Dr. J. A. Burke Dr. T. W. Dingle


Dr. D. Crampton

acknowledgements

As in any work culminating in years of toil, there are many people who should be thanked for encouraging me to try, for seeing me through and for making it possible. In an attempt not to offend by omission, I shall mention only those individuals who deserve my deepest appreciation: Chris Pritchett, who suggested the topic and provided support and advice throughout the project while on sabbatical; Michael de Robertis for his insatiable interest, enthusiasm, and eagerness to assist in any manner and at any time; Eileen Friel who has *truly* been an inspiration; Sidney van den Bergh, for sharing his plethora of information and his data; and Russ Robb and Phil Fischer who kept me laughing through it all.

Contents

abstract	ii
acknowledgements	iii
1 Introduction	1
2 The Data	3
2.1 The Observations	3
2.2 Image Identification	5
3 Image Analysis Techniques	8
3.1 The Isophotal Method	9
3.1.1 Software	10
3.1.2 Simulating the CFHT CCD Data	14
3.1.3 Limitations of the Isophotal Method	17
3.2 The Moment Method	37
3.2.1 The Software	39
3.2.2 Limitations of the Moment Method	40
3.3 Comparing the Methods	55
4 Image Analysis	58

5 Results	81
6 Discussion	91
6.1 Selection Effects	95
6.2 Possible Causes of Flattening	104
7 Conclusion	119
8 References	121
9 Appendix A	124
10 Appendix B	126
11 Appendix C	128
12 Appendix D	129

List of Tables

1	Cluster Data	4
2	Observational Data	6
3	The Mean Ellipticity and Orientation Measured	82
4	The Mean Ellipticity Measured at Various Brightness Levels	85
5	A Comparison of Mean Ellipticities of M31 Globular Clusters	86
6	Mean Ellipticities of Local Group Globular Clusters	92

List of Figures

1	The residual isophotal axial ratio of a model globular cluster.	18
2	The residual orientation of the isophotal semi-major axis of a model globular cluster.	19
3	The residual isophotal axial ratio of a point source convolved with a Gaussian function.	21
4	The residual isophotal axial ratio of a point source convolved with an elliptical ($\epsilon = 1 - b/a = 0.20$) Gaussian function.	22
5	The residual orientation of the isophotal semi-major axis of a point source convolved with an elliptical ($\epsilon = 1 - b/a = 0.20$) Gaussian function.	23
6	The residual isophotal axial ratio of a model globular cluster convolved with an elliptical ($\epsilon = 1 - b/a = 0.20$) Gaussian function.	25
7	The residual orientation of the isophotal semi-major axis of a model globular cluster convolved with an elliptical ($\epsilon = 1 - b/a = 0.20$) Gaussian function.	26
8	The residual isophotal axial ratio of a model globular cluster convolved with an elliptical ($\epsilon = 1 - b/a = 0.40$) Gaussian function.	27

9	The residual orientation of the isophotal semi-major axis of a model globular cluster convolved with an elliptical ($\epsilon = 1 - b/a = 0.40$) Gaussian function.	28
10	The residual isophotal axial ratio of a model globular cluster convolved with an elliptical ($\epsilon = 1 - b/a = 0.01$) Gaussian function. . .	30
11	The residual orientation of the isophotal semi-major axis of a model globular cluster convolved with an elliptical ($\epsilon = 1 - b/a = 0.01$) Gaussian function.	31
12	The residual isophotal axial ratio of a noisy model globular cluster. .	32
13	The residual orientation of the isophotal semi-major axis of a noisy model globular cluster.	33
14	The residual isophotal axial ratio of a larger model globular cluster.	35
15	The residual isophotal axial ratio of a smaller model globular cluster.	36
16	The residual ellipticity calculated by the moment method for model globular cluster.	41
17	The residual orientation of the semi-major axis calculated by the moment method for model globular cluster.	42
18	A comparison of the residual ellipticity computed by the moment method for a model globular cluster in the presence and absence of noise.	44
19	A comparison of the residual orientation computed by the moment method for a model globular cluster in the presence and absence of noise.	45
20	The residual ellipticity calculated by the moment method for a point source convolved with an elliptical ($\epsilon = 0.20$) Gaussian function. . .	46

21	The residual orientation calculated by the moment method for a point source convolved with an elliptical ($\epsilon = 0.20$) Gaussian function.	47
22	A comparison of the residual ellipticity computed for a convolved ($\epsilon = 0.20$) model globular cluster when smearing-subtracted moments are and are not employed.	49
23	A comparison of the residual orientation computed for a convolved ($\epsilon = 0.20$) model globular cluster when smearing-subtracted moments are and are not employed.	50
24	A comparison of the residual ellipticity computed for a convolved ($\epsilon = 0.01$) model globular cluster when smearing-subtracted moments are and are not employed.	51
25	A comparison of the residual orientation computed for a convolved ($\epsilon = 0.01$) model globular cluster when smearing-subtracted moments are and are not employed.	52
26	A comparison of the residual ellipticity calculated by the isophotal and moment methods for a model globular cluster.	56
27	A comparison of the residual orientation calculated by the isophotal and moment methods for a model globular cluster.	57
28	The variation of isophotal axial ratio with effective radius and the intensity profile of G1 observed through a V filter for 60s.	60
29	The variation of isophotal axial ratio with effective radius and the intensity profile of G1 observed through a B filter for 300s.	61
30	The variation of isophotal axial ratio with effective radius and the intensity profile of G64 observed through a V filter for 400s.	62
31	The variation of isophotal axial ratio with effective radius and the intensity profile of G72 observed through a B filter for 500s.	63

32	The variation of isophotal axial ratio with effective radius and the intensity profile of G72 observed through a B filter for 1000s.	64
33	The variation of isophotal axial ratio with effective radius and the intensity profile of G73 observed through a B filter for 500s.	65
34	The variation of isophotal axial ratio with effective radius and the intensity profile of G76 observed through a B filter for 400s.	66
35	The variation of isophotal axial ratio with effective radius and the intensity profile of G78 observed through a B filter for 400s.	67
36	The variation of isophotal axial ratio with effective radius and the intensity profile of G119 observed through a V filter for 120s.	68
37	The variation of isophotal axial ratio with effective radius and the intensity profile of G148 observed through a V filter for 120s.	69
38	The variation of isophotal axial ratio with effective radius and the intensity profile of G185 observed through a B filter for 400s.	70
39	The variation of isophotal axial ratio with effective radius and the intensity profile of G205 observed through a B filter for 400s.	71
40	The variation of isophotal axial ratio with effective radius and the intensity profile of G213 observed through a B filter for 400s.	72
41	The variation of isophotal axial ratio with effective radius and the intensity profile of G217 observed through a V filter for 120s.	73
42	The variation of isophotal axial ratio with effective radius and the intensity profile of G217 observed through a V filter for 400s.	74
43	The variation of isophotal axial ratio with effective radius and the intensity profile of G219 observed through a V filter for 120s.	75
44	The variation of isophotal axial ratio with effective radius and the intensity profile of G229 observed through a V filter for 120s.	76

45	The variation of isophotal axial ratio with effective radius and the intensity profile of G257 observed through a V filter for 120s.	77
46	The variation of isophotal axial ratio with effective radius and the intensity profile of G272 observed through a B filter for 400s.	78
47	The variation of isophotal axial ratio with effective radius and the intensity profile of G280 observed through a V filter for 60s.	79
48	The variation of isophotal axial ratio with effective radius and the intensity profile of G280 observed through a B filter for 400s.	80
49	A comparison of the ellipticity of M31 globular clusters that are in common with Lupton (1989).	88
50	A comparison of the ellipticity of M31 globular clusters measured in B for clusters in common with this work.	90
51	A comparison of the distribution of globular cluster ellipticity for the globulars associated with the Milky Way, Magellanic Clouds and M31.	93
52	No correlation of ellipticity with B is observed for the M31 globular clusters of this work.	96
53	No correlation of ellipticity with V is observed for the M31 globular clusters of this work.	97
54	No correlation of measured ellipticity with celestial direction is observed for the the M31 globular clusters in this work.	98
55	No correlation of ellipticity with celestial direction is observed for the the M31 globular clusters measured by SSB.	99
56	No correlation of ellipticity with absorption is observed for the M31 globular clusters of this work.	101
57	No correlation of ellipticity with absorption is observed for the M31 globular clusters measured by SSB.	102

58	No correlation of ellipticity with UV flux measured by Cowley and Burstein (1988) is observed.	106
59	No correlation of ellipticity with intrinsic colour is observed for the M31 globular clusters of this work.	107
60	No correlation of ellipticity with intrinsic colour is observed for M31 globular clusters in the combined sample of SSB and SSG.	108
61	No correlation of ellipticity with orientation is observed for the M31 globular clusters of this work.	110
62	No correlation of ellipticity with orientation is observed for the M31 globular clusters in the sample measured by SSB.	111
63	The apparent correlation of ellipticity with projected galactocentric distance.	112
64	No correlation of ellipticity with projected galactocentric distance is observed for M31 globular clusters in the combined sample of SSB and SSG.	113
65	No correlation of the orientation of the semi-major axis with projected galactocentric distance is observed for M31 globular clusters of this work.	114
66	No correlation of the orientation of the semi-major axis with projected galactocentric distance is observed for M31 globular clusters measured by SSB.	115
67	The apparent correlation of ellipticity with radial velocity for the M31 globular cluster sample of SSB.	116

Chapter 1

Introduction

The globular clusters associated with the great spiral galaxy in Andromeda, Messier 31 (M31), were described by Hubble (1932) as resembling “soft, hazy star images, but [built] up with increasing exposure in a manner perceptibly different from true stellar images.” On the basis of structure, luminosity, diameters and colours, Hubble provisionally identified these “nebulous stars” as globular clusters associated with the Andromeda Galaxy. Many authors have since added to Hubble’s original list of 140 M31 globular clusters (see, for example, Crampton *et al.*, 1985 and references therein) increasing the total number to over 500, approximately five times as many as the Milky Way boasts.

Globular clusters are the oldest known subunits of galaxies. They contain 10^4 to 10^5 stars tightly packed by gravity into a region 30 to 100 lightyears in diameter. The name “globular cluster” was assigned to these groups of stars because the majority of the ones associated with the Galaxy appear to be nearly spherical in shape. Recent studies have shown that the slight flattening observed for some Milky Way globular clusters can be attributed to cluster rotation (Pryor *et al.* 1986; Meylan and Mayor (1986, 1985); Mayor *et al.* 1984; Lupton *et al.* 1985).

By contrast, the globular clusters associated with the nearby irregular galaxies, the Large and Small Magellanic Clouds, are more frequently elliptical (Geisler and Hodge 1980; Frenk and Fall 1982; Geyer and Richtler 1981; Kontizas *et al.* 1985; Kontizas *et al.*, 1989). Rotational velocities are not available for these clusters and the source of such large ellipticities remains unclear. A possible explanation for the difference in cluster shape between the Clouds and the Galaxy is simply that globular cluster formation varies with galactic type. An examination of the ellipticity of the globular clusters associated with M31 would therefore be instructive in the investigation of trends in globular shape with galactic type and within the Local Group of galaxies.

The globular clusters of M31 were first reported to be flattened by Spasova and Staneva (1984) using photographic plates. The ellipticity of the clusters was determined isophotally by solving the equation of the ellipse which approximated the contour. More recently, Lupton (1989) has obtained cluster ellipticities by applying a maximum likelihood method originally described by Frenk and Fall (1982) to his digital images. The purpose of this project is threefold:

- to determine isophotally and by a moment method, the ellipticity and orientation of some of the brighter globular clusters associated with the Andromeda Galaxy as imaged by a Charge Coupled Device (CCD);
- to compare these measures with previous work and explore possible trends in the ellipticity of globular clusters among Local Group galaxies;
- to investigate possible sources for the observed flattening of the globular clusters associated with the Andromeda Galaxy.

Chapter 2

The Data

2.1 The Observations

The data analyzed in this project (see Table 1) were obtained by C. J. Pritchett and S. van den Bergh at the prime focus of the 3.6 m Canada-France-Hawaii Telescope (CFHT) in October 1985 through a B filter using the RCA1 CCD detector. The gain and readout noise for these observations was 28.6 electrons/A.D.U. and 75 electrons respectively (Christian, 1988). Additional data were obtained in October 1987 at the prime focus of the CFHT using the RCA2 CCD detector and a V filter. The gain was 11.6 electrons/A.D.U. and the readout noise was 51 electrons for these data (Christian, 1988). The data were bias subtracted and flat fielded by C. J. Pritchett at the University of Victoria using his image processing software package R2D2. The double-density RCA2 observations were reduced in size from 640×1024 square pixels to 320×512 square pixels by averaging pixels in 2×2 blocks. This reduction in size permitted the 1987 data to be easily viewed on the International Imaging System (I²S) Model 70 image processor. Since the reduced observations correspond in size to the 1985 data, the linear scale of all the

Table 1: Cluster Data

Name	RA (1950.0)	Dec	V	B-V	D_p (kpc)	Other Designations
G1	00 30 05.6	39 18 09	13.72	0.88	33.0	M II
G64	00 37 48.9	41 05 18	15.12	0.78	6.1	V301, BB12
G72	00 38 09.0	41 02 27	14.99	0.96	5.1	V44, BB19
G73	00 38 11.6	41 24 59	14.96	0.83	6.8	H III, BB20
G76	00 38 15.5	40 19 21	14.26	0.84	8.9	V12
G78	00 38 17.6	40 57 19	14.26	1.13	4.7	V42, BB23
G119	00 39 09.4	40 30 44	15.04	0.82	5.9	V23, BB58
G148	00 39 34.8	40 57 36	15.04	0.75	1.3	V62, BB86
G185	00 40 00.5	40 58 17	14.54	0.99	0.3	V70, BB127
G205	00 40 25.5	41 05 08	14.83	1.27	1.5	V93, BB151
G213	00 40 30.3	40 50 57	14.68	0.90	2.2	V64, BB158
G217	00 40 33.4	41 11 21	15.05	1.04	2.6	V100, BB163
G219	00 40 34.2	39 32 48	15.09	0.69	16.1	M IV
G229	00 40 46.6	41 04 52	15.04	0.79	2.3	V95, BB178
G257	00 41 14.3	41 13 54	15.06	0.87	4.2	V106, BB206
G272	00 41 29.9	41 02 56	14.75	0.86	4.1	V101, BB218
G280	00 41 45.1	41 05 12	14.18	0.95	4.9	V282, BB225

Notes to Table 1:

“G” number is from Sargent *et al.* (1977)

V, B-V, and projected galactocentric distance D_p from Crampton *et al.* (1985)

BB = Battistini *et al.* (1980)

H = Hubble (1932)

M = Mayall and Eggen (1953)

V = Vetešnik (1962)

observations is 0.4119 arcseconds on the sky per pixel (see Appendix A for details).

The clusters range in visual magnitude from 15.12 to 13.72 (Crampton *et al.*, 1985) and were selected based upon their brightness. The exposure times range from 60 to 1000 seconds and the seeing was < 1.4 arcseconds in the mean (see Table 2 and Appendix A). The data were analyzed at the University of Victoria using the VAX 11/750 computer.

2.2 Image Identification

A list of the globular clusters of this project can be found in Table 1. These clusters have been identified by many authors (Crampton *et al.* 1985, Battistini *et al.* 1980, Sargent *et al.* 1977, Mayall and Eggen 1953, Hubble 1932) as members of the M31 globular cluster system and their coordinates are well determined. The identification of the clusters on the CFHT CCD frames could not be determined using their published celestial coordinates since the telescope's celestial coordinates for each observation were unavailable. The identification of each cluster was therefore determined by visual inspection of each frame using the I²S and the finder charts in Hodge's Atlas of the Andromeda Galaxy (1981). With the exception of G1, Hodge's Atlas identified each of the clusters in this project. The identification of G1 was made possible by means of Figure 1 of Pritchett and van den Bergh (1984).

Since the identification of the globular clusters in each of the CFHT CCD frames could not be determined using the known celestial coordinates of the clusters but instead were based upon visual comparisons with published finder charts, it was suggested (Richer, 1988) that the objects identified for this project as globular

Table 2: Observational Data

Name	Filter	Exposure Time (s)	CCD Detector	Seeing (arcseconds)	
				R.A.	Dec.
G1	V	60	RCA2	1.05	1.01
	B	300	RCA1	1.29	1.27
G64	V	400	RCA2	0.83	0.86
G72	B	500	RCA1	1.13	1.32
	B	1000	RCA1	1.18	1.48
G73	B	500	RCA1	1.09	1.33
G76	B	400	RCA1	1.24	1.23
G78	B	400	RCA1	1.22	1.15
G119	V	120	RCA2	0.98	1.08
G148	V	120	RCA2	1.20	1.18
G185	B	400	RCA1	1.41	1.29
G205	B	400	RCA1	1.18	1.40
G213	B	400	RCA1	1.19	1.25
G217	V	120	RCA2	0.99	1.12
	V	400	RCA2	0.97	0.80
G219	V	120	RCA2	0.83	0.70
G229	V	120	RCA2	1.00	1.05
G257	V	120	RCA2	0.91	1.08
G272	B	400	RCA1	1.10	1.19
G280	V	60	RCA2	1.10	1.04
	B	400	RCA1	1.11	1.20

clusters associated with M31 may be foreground double stars or background galaxies, not clusters. These hypotheses were explored and proved to be untenable (see Appendix B). Thus, the images identified as globular clusters on each of the CCD frames are neither overlapping stellar images nor distant elliptical galaxies.

Chapter 3

Image Analysis Techniques

The globular clusters of M31 were first reported to be flattened by Spasova and Staneva (1984) using photographic plates. The ellipticity of the clusters was determined isophotally by solving the equation of the ellipse which approximated the contour. More recently, Lupton (1989) has obtained cluster ellipticities using a maximum likelihood method originally described by Frenk and Fall (1982). In this project, the ellipticity and orientation of some of the brighter globular clusters associated with the Andromeda Galaxy have been determined using an isophotal technique and a moment technique described by Trumpler and Weaver (1953). These two methods are independent but, *in principle*, are consistent in their measures of ellipticity (see, however, Section 3.3).

3.1 The Isophotal Method

Interpolation of the discrete CCD images to construct isophotes representative of the original image is permissible for the CFHT CCD data in this project because the requirements of the sampling theorem are satisfied. The sampling theorem states that it is possible to recover, with full accuracy, the intervening values of a band-limited function (Bracewell, 1965). In other words, a one dimensional function whose Fourier transform is zero for frequencies greater than some cutoff frequency, S_c , is fully specified by values spaced at equal intervals *not* exceeding $(2S_c)^{-1}$.

In the case of astronomical observations seeing, as defined in Appendix A, band-limits the power spectrum but it does not produce the required sharp cutoff in the Fourier transform; a high frequency tail is present because seeing is, very approximately, Gaussian in form and the Fourier transform of a Gaussian function is a Gaussian with a high frequency tail. The utilization of a two-dimensional detector such as a CCD pixel will further smear the power spectrum and therefore aids in producing a sharp cutoff in the Fourier transform of the function. Hence the smeared power spectrum closely approximates a band-limited function whose Fourier transform is zero at frequencies greater than some cutoff frequency S_c and according to sampling theory, the power spectrum is fully specified by values spaced at intervals less than or equal to $(2S_c)^{-1}$ where $S_c^{-1} \sim \text{FWHM}$. So, the sampling theorem requires that the sample size be $\lesssim \frac{1}{2}\text{FWHM}$ for a one dimensional function and is approximately applicable to two dimensional functions. The FWHM, or seeing, for each CCD frame in this project is listed in Table 2 and the sample size is 1 pixel or 0.4119 arcseconds (see Appendix A). Almost all the observations in this project have been oversampled; the the mean seeing for G219 is 1.87 arcseconds

which, for a two dimensional function, sufficiently approximates the critical value of 2. Therefore, according to the sampling theorem, the globular cluster images in this project may be reconstructed by interpolation.

3.1.1 Software

The image processing software package R2D2 employed in the analysis of the data of this project linearly interpolates the pixels of the CFHT CCD images to obtain isophotes. The input parameters required by R2D2, which was written by C. J. Pritchett at the University of Victoria, are the extreme contour levels, the incremental value for the isophotes, an estimate of the centroid of the image being contoured and a tolerance limit on this estimate.

Once the image centroid, tolerance and intensity or contour level have been specified, the pixels comprising the CCD frame are scanned for adjacent pixels whose recorded intensities bound the specified contour level. These pixels are interpolated in each of the CCD's axial directions, namely x and y , using a first-order Newton interpolatory divided difference formula:

$$I(x, y) = I(x_o, y_o) + \left[\frac{I(x_1, y_1) - I(x_o, y_o)}{x_1 - x_o} \right] (x - x_o) \quad (1)$$

where $I(x, y)$ is the specified contour level and the intensity, I , of pixels (x_o, y_o) and (x_1, y_1) is known. Rearranging, the x -ordinate of the interpolated point, whose intensity corresponds to the required contour level, can be determined:

$$x = x_o + \left[\frac{I(x, y) - I(x_o, y_o)}{I(x_1, y_1) - I(x_o, y_o)} \right] (x_1 - x_o) \quad (2)$$

A similar expression defines the y -ordinate of the interpolated point which lies on the required isophote. Caution is exercised to ensure each point comprising the interpolated isophote is unique.

The centroid, (\bar{x}, \bar{y}) , of each isophote is determined as follows:

$$\bar{x} = \frac{1}{A} \iint_R x dx dy \quad (3)$$

$$\bar{y} = \frac{1}{A} \iint_R y dx dy \quad (4)$$

where R is the region of area A bounded by the isophote. The area is given by:

$$A = \iint_R dx dy \quad (5)$$

The “effective” radius, R_{eff} , of the isophote, that is the radius of a circle containing the same area as the region enclosed by the isophote, is determined as follows:

$$R_{eff} = \left(\frac{A}{\pi} \right)^{\frac{1}{2}} \quad (6)$$

(Pritchett, 1979) where A is defined in Equation 5

If the centroid of the isophote is not within the specified tolerance, or if the isophotal effective radius does not exceed 2.54 pixels, then the isophote is rejected and its shape, orientation and semi-major axis are not computed.

An ellipse is fitted to each isophote deemed acceptable by the above criteria and a nonlinear least-squares method, which incorporates an iterative outlier rejection technique, is employed to compute the shape, orientation and semi-major axis of the isophote. The outlier rejection technique is incorporated to avoid biasing the fit and hence the determination of isophotal attributes by the presence of noisy pixels.

A nonlinear method is employed because the equation of the ellipse (the model) is not linear in its parameters. The least-squares method is still employed for simplicity and the merit function (and hence normal equations) for the method reflect the nonlinearity of the model. The model to be fitted is given by:

$$y(x; \vec{c}) = a\sqrt{1 - e^2} \left[1 - e^2 \cos^2(\theta - \theta_0) \right]^{-\frac{1}{2}} \quad (7)$$

where \vec{c} is the vector of all parameters being fitted namely, a , the semi-major axis, e , the eccentricity, and θ_o , the orientation of the ellipse. The right-hand side of Equation 7 is the general equation of an ellipse with arbitrary orientation and centroid expressed in polar coordinates. The ellipticity of an ellipse is defined as:

$$\epsilon = 1 - \left(\frac{b}{a}\right) \quad (8)$$

where

$$\frac{b}{a} = \sqrt{1 - e^2} \quad (9)$$

and b is the semi-minor axis of the ellipse. The χ^2 merit function of the model is:

$$\chi^2(\vec{c}) = \sum_{i=1}^N \left[\frac{y_i - y(x_i; \vec{c})}{\sigma_i} \right]^2 \quad (10)$$

where σ_i^2 describes the uncertainty of the i^{th} data point; it is the inverse of the weighting factor for each data point and is assigned a value of unity. Equation 10 yields the maximum likelihood that the model represents the data.

According to the method of least-squares, the optimum values of the M unknown parameters c_k , ($k = 1, 2, \dots, M$) are obtained by minimizing χ^2 with respect to each of the parameters simultaneously. That is,

$$\frac{\partial \chi^2}{\partial c_k} = \frac{\partial}{\partial c_k} \sum_{i=1}^N \left[\frac{y_i - y(x_i; \vec{c})}{\sigma_i} \right]^2 = 0 \quad (11)$$

$$k = 1, 2, \dots, M$$

With nonlinear dependences, the minimization of the χ^2 merit function must proceed iteratively. The set of linear equations to be simultaneously solved for the vector of parameters \vec{c} is:

$$\sum_{l=1}^M \alpha_{kl} \delta c_l = \beta_k \quad (12)$$

where

$$\alpha_{kl} \equiv \frac{1}{2} \frac{\partial^2 \chi^2}{\partial c_k \partial c_l} \quad (13)$$

is the curvature matrix $[\alpha]$, δc_i is the increment which, when added to the current approximation gives the next approximation to be used in the iteration, and

$$\beta_k = -\frac{1}{2} \frac{\partial \chi^2}{\partial c_k} \quad (14)$$

Once an acceptable minimum of Equation 10 has been found, the standard errors in the fitted parameters \vec{c} are computed from the covariance matrix $[V]$ where

$$[V] \equiv [\alpha]^{-1} \quad (15)$$

An outlier rejection technique is incorporated in the iterative procedure to fit an ellipse to the isophote because the least-squares method assumes a normal distribution of errors. The probability of occurrence of outliers in the assumed Gaussian distribution is so small that the maximum likelihood method (*i.e.*, the least-squares method) is willing to distort the whole fit to try to bring the extreme values, mistakenly, into line. Therefore, prior to commencing the next iteration to improve the fit of an ellipse to the isophote (*i.e.*, the next iteration to further minimize Equation 10), the model data is tested for outliers using the test statistic:

$$T_i = \left| \frac{x_i - \bar{x}}{s} \right| \quad (16)$$

The supposed outlier, x_i , is excluded from computation of the mean, \bar{x} , and standard deviation, s , of the model data.

If the test statistic T_i equals or exceeds 2.3, then the null hypothesis that the tested extreme value originated in the population from which the rest of the sample came, can be rejected at the 0.02 confidence level. (Strictly speaking, this confidence level only applies to a sample with a Gaussian distribution.)

Once the χ^2 merit function defined in Equation 10 has been minimized and the parameters have been tabulated along with their errors, the next contour level

specified in the list of input parameters for R2D2 is processed. The procedure continues until all the required isophotes are processed.

3.1.2 Simulating the CFHT CCD Data

Several artificial CCD frames were created to simulate the CFHT CCD data of this project so that the capabilities of the programs employed in the determination of the shape of the CCD images of globular clusters associated with M31 could be determined. The image processing software package R2D2, written by C. J. Pritchett of the University of Victoria, was used to create a frame containing a de Vaucouleurs (1953) $r^{1/4}$ galaxy of known centroid, ellipticity and position angle and five stellar images of various specified intensities. The magnitude of these point sources were chosen to encompass the range observed for the CFHT data. Although globular clusters are best described by a King model which is *not* a $r^{1/4}$ law, King (1962) has demonstrated that in the outer parts of elliptical galaxies which are described by a de Vaucouleurs $r^{1/4}$ law, the brightness distribution is adequately represented by a King globular cluster model. Hence the intensity (I) in each pixel of the artificial globular cluster image was computed in R2D2 using:

$$\log I = A + BR^{1/4} \quad (17)$$

where A was defined as 10^4 Analog-to-Digital Units (A.D.U.) and B as $-\sqrt{2^{1/4}}$ pixels $^{-1/4}$. The image created using the DEVAUC command in R2D2 as described above, was several times larger than the CFHT globular cluster images of this project. In an attempt to replicate the extent and intensity profile of the data, this unrealistic artificial image was reduced in size by averaging the pixels in 5×5 blocks using the SCRUNCH command in R2D2. The resulting image has a size, intensity profile, integrated brightness (in A.D.U./pixel), FWHM and full width at

0.1 max typical of the CFHT CCD data of this project and henceforth is referred to as the “base” frame.

A Gaussian noise spectrum was added to the base frame to simulate the instrumental noise observed for the CFHT data in this project. The noise associated with the CFHT data was found to have a maximum value of 4.2 A.D.U. using the following relation:

$$Noise = \frac{\sqrt{sky * gain + (readout\ noise)^2}}{gain} \quad (18)$$

where the gain was 28.6 electrons per A.D.U., the readout noise was 75 electrons and the maximum sky was determined to be 299.8 A.D.U. by the above mentioned outlier iterative technique. The modal magnitude of the Gaussian noise spectrum added to the base frame was verified as being within 0.5 A.D.U. of the peak noise measured for the data in this project.

To simulate the effects of seeing (defined in Appendix A) observed in the CFHT data, the base frame containing stars and a galaxy with known centroid, shape and orientation was convolved with an elliptical Gaussian seeing function of the form:

$$\exp \left[-\frac{1}{2}(g^2 + h^2) \right] \quad (19)$$

where

$$g = \frac{x - m_x}{\sigma_x} \quad (20)$$

and

$$h = \frac{y - m_y}{\sigma_y} \quad (21)$$

The values of σ_x and σ_y were chosen from Table 2 to reproduce the maximum and minimum elliptical point-spread functions, in pixels, observed in the CFHT data for this project, namely $(\sigma_x, \sigma_y) = (1.22, 1.52)$ and $(1.28, 1.27)$ (recall FWHM

$\equiv 2.355\sigma$ and 1 pixel $\equiv 0.4119$ arcseconds). The base frame was convolved with these elliptical Gaussian seeing functions so that seeing effects could be examined in the absence of noise.

In order to confirm that the point-spread functions of the convolved artificial frames corresponded to those of the CFHT frames, the seeing for the artificial frames was determined in the same manner as the CFHT data (see Appendix A). The deviation in the point-spread function of the simulated frames from the CHFT frames being modelled was 0.03 arcseconds in each of the x and y directions.

3.1.3 Limitations of the Isophotal Method

The attributes of the linearly interpolated isophotes of the globular cluster in each of the model frames were determined using R2D2 as described in Section 3.1.1. Figures 1 through 11 illustrate the intensity profile of the model globular cluster and the corresponding variation in computed axial ratio and orientation of the cluster isophotes as a function of isophotal effective radius *prior* to the addition of a noise spectrum to the images. The isophotes were interpolated in increments of 2 A.D.U. The errors associated with the axial ratio and orientation describe the fit of the ellipse to the isophote and are not related to the CFHT observations (see Section 3.1.1).

Since the deviation of globular cluster shape from circularity is small for Galactic clusters (see, for example, White and Shawl 1987) and the globulars associated with the Andromeda Nebula are similar to those of the Milky Way in size, colour, spacial distribution and range of metallicity (Crampton *et al.*, 1985; van den Bergh, 1988), the deviation of shape from circularity is expected to be similarly small. The error in the determination of globular shape for the simulated frames by the isophotal technique therefore should not exceed 1% as this is the anticipated scale of ellipticity variation among clusters. The desired degree of accuracy in the determination of axial ratio using R2D2 is obtained for isophotes with effective radii exceeding 2.54 pixels as demonstrated in Figure 1. For this range of isophotal effective radii, the orientation is within 3° of the known value (see Figure 2).

As mentioned in Section 3.1.1, the determination of isophotal attributes is not permitted by the software when the effective radius does not exceed 2.54 pixels (which corresponds to 1.05 arcseconds for the CFHT CCD data of this project). The inability to determine isophotal attributes at small effective radii is unimportant for large images but prevents the accurate determination of image shape and

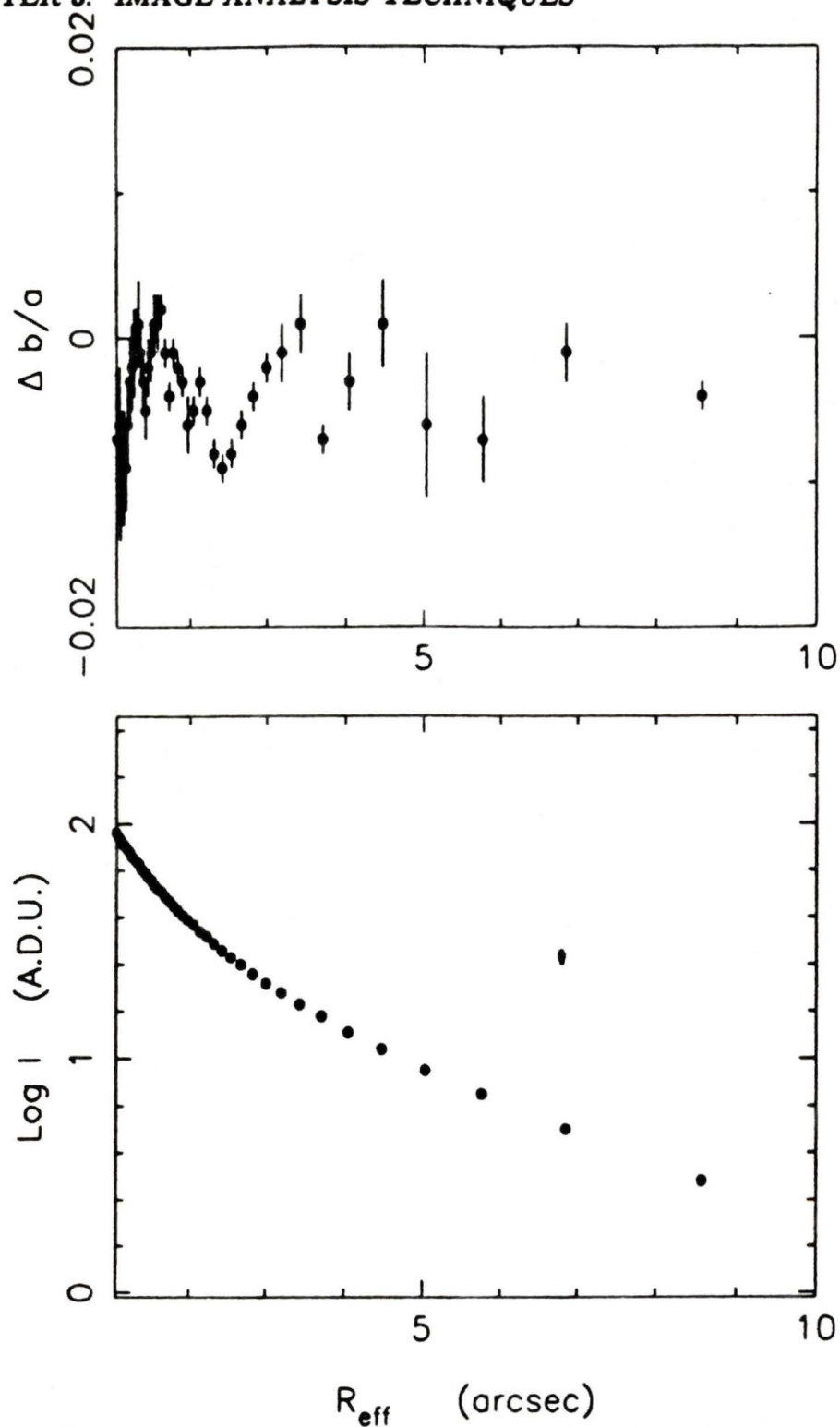


Figure 1: The residual isophotal axial ratio as a function of isophotal effective radius and the intensity profile of a model globular cluster image. The isophotal increment is 2 A.D.U. and the error bars are calculated from the residuals of the fit of an ellipse to the isophote.

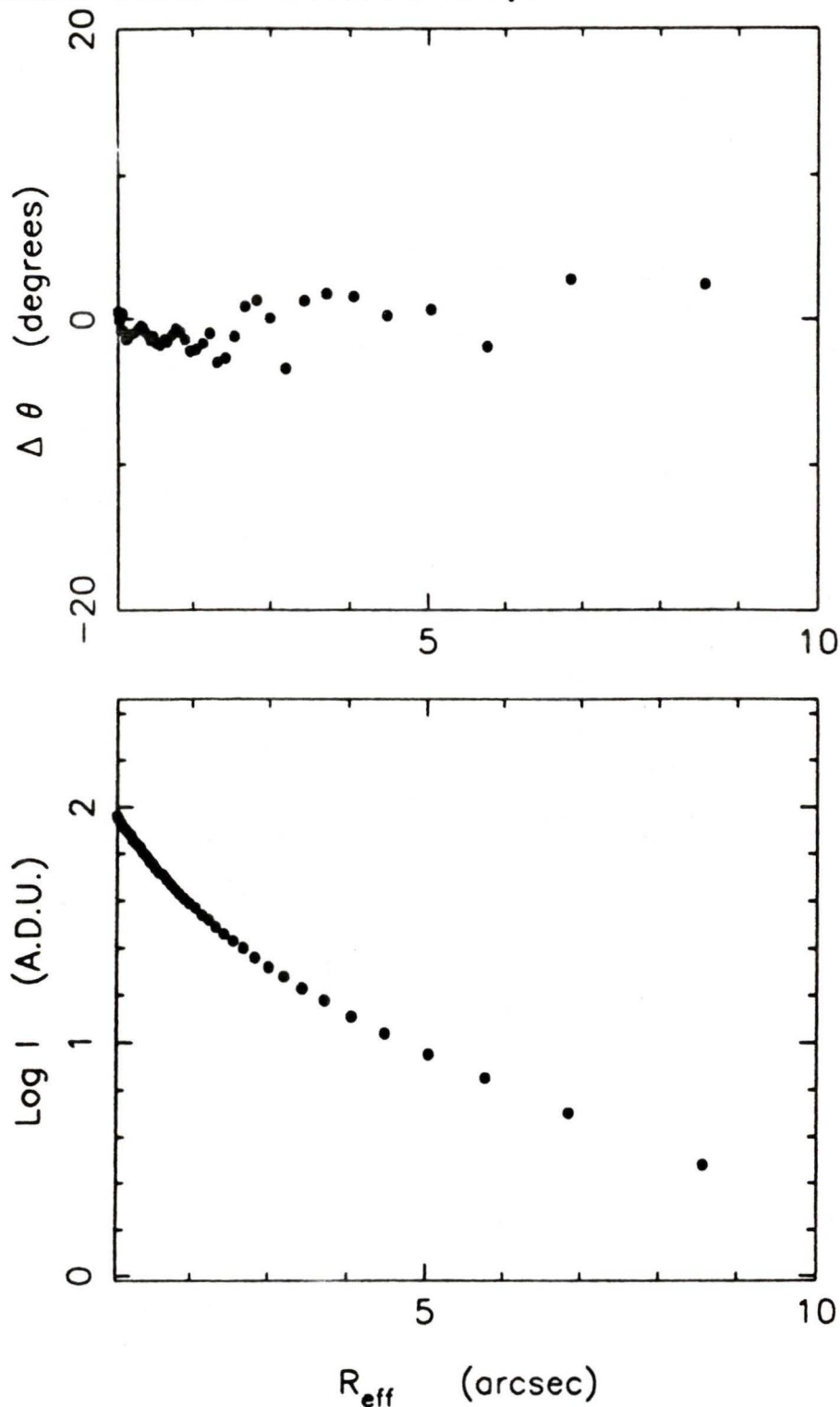


Figure 2: The residual orientation of the isophotal semi-major axis as a function of isophotal effective radius and the intensity profile of a model globular cluster image. The isophotal increment is 2 A.D.U. and the error bars are the size of the symbols.

orientation for small images such as stars. It is possible however, to apply a bicubic spline interpolant to a small stellar image to magnify the image and permit the isophotal attributes to be accurately determined because the CFHT CCD data of this project satisfies the criteria of the sampling theorem (see Section 3.1). To demonstrate the effectiveness of this interpolation for ideal data, the base frame was convolved with an ideal (circular) Gaussian function. The resulting stellar image was magnified using the bicubic spline interpolation subroutines published by Press *et al.* in their text *Numerical Recipes* (1986) and this magnified image was then linearly interpolated at intervals of 2 A.D.U. to obtain stellar isophotes. Figure 3 illustrates the incredible accuracy and consistency with which the isophotal shape of a magnified stellar image is determined. It should be noted that isophotal orientation cannot be computed in this instance since a circle cannot be said to possess an orientation.

In the non-ideal case, that is when the seeing effects are best described by an elliptical point-spread function, the effect of this seeing function upon point sources is to produce a stellar image with an elliptical shape. This effect is illustrated in Figure 4 where the base frame has been convolved with an elliptical Gaussian function corresponding to the maximum elliptical seeing profile observed for the CFHT data, namely $\sigma_x = 1.22$, $\sigma_y = 1.52$. Recall that isophotal orientation is defined as the position angle of the semi-major axis of an elliptical isophote with respect to the horizontal axis of the CCD frame. Thus, when an elliptical point-spread function is convolved with a stellar point source, the computed isophotal orientation is the direction of the semi-major axis of the convolved elliptical function (see Figure 5).

The effects of an elliptical seeing function upon isophotal attributes described above have little effect upon the computed attributes in the wings of an extended

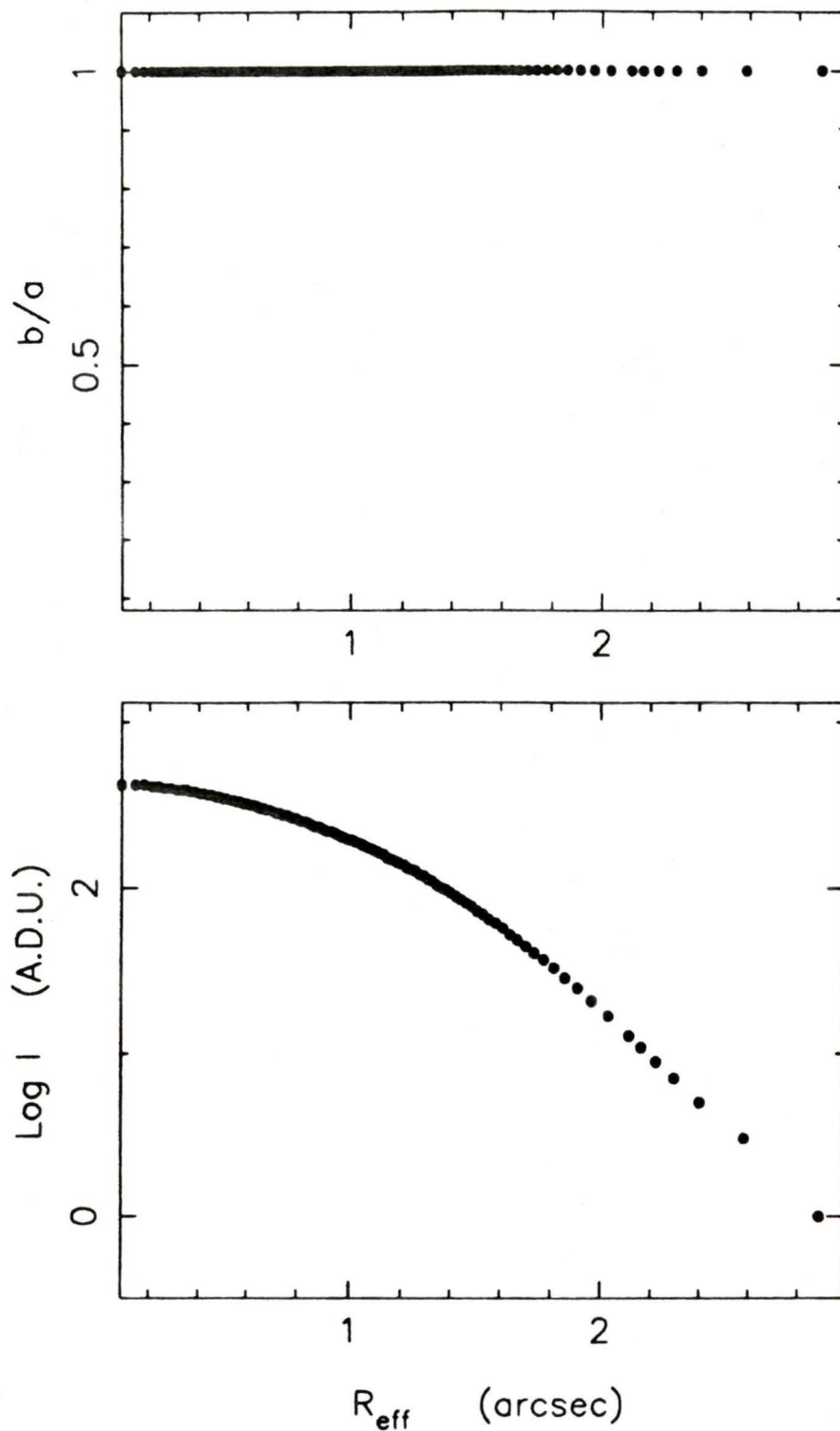


Figure 3: The residual isophotal axial ratio as a function of isophotal effective radius and the intensity profile of a point source convolved with a Gaussian function. The isophotal increment is 2 A.D.U. and the error bars are the size of the symbols.

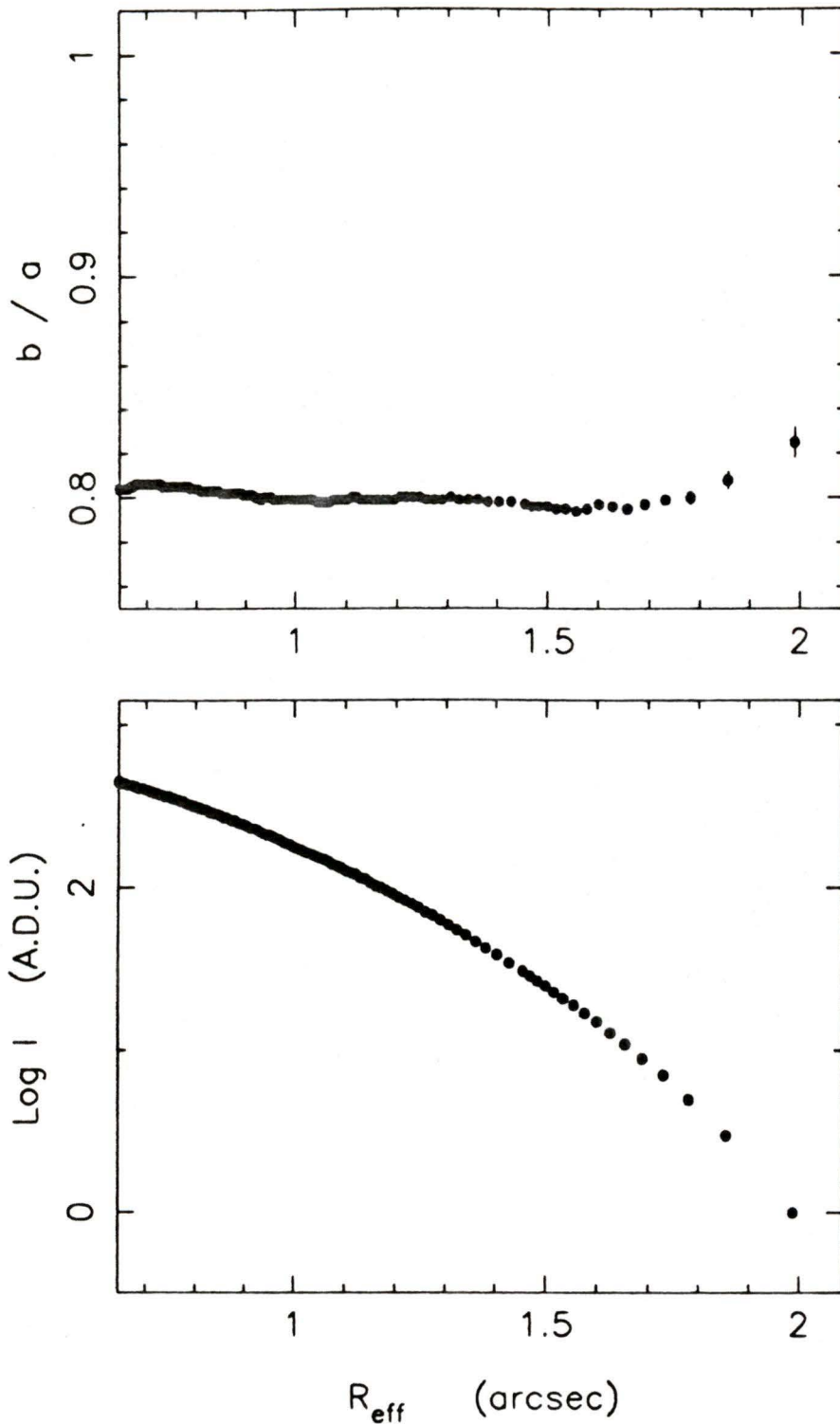


Figure 4: The residual isophotal axial ratio as a function of isophotal effective radius and the intensity profile of a point source convolved with an elliptical ($\epsilon = 1 - b/a = 0.20$) Gaussian function. The isophotal increment is 2 A.D.U. and the error bars are the size of the symbol.

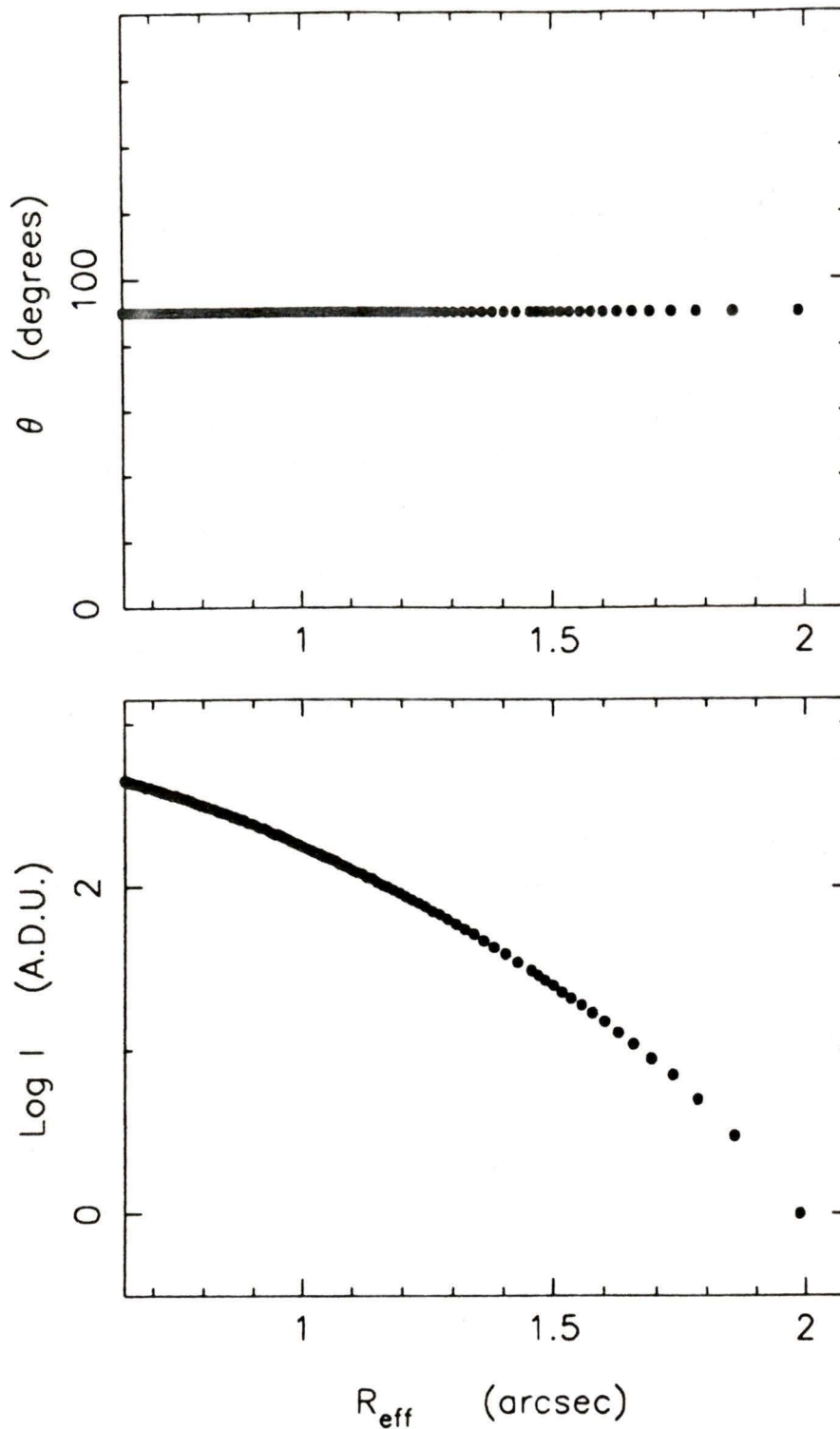


Figure 5: The residual orientation of the isophotal semi-major axis as a function of isophotal effective radius and the intensity profile of a point source convolved with an elliptical ($\epsilon = 1 - b/a = 0.20$) Gaussian function. The isophotal increment is 2 A.D.U. and the error bars are the size of the symbols.

object but do become increasingly important as isophotal effective radius decreases. As Figure 6 indicates, the convolved seeing function has very little effect upon the shape of the model globular cluster's isophotes with effective radii exceeding 3.3 arcseconds. Isophotes with smaller radii are however, more strongly affected by the convolved seeing function; the isophotal shape tends towards the shape of the convolved seeing function. Similarly, Figure 7 indicates that the orientation of the cluster isophotes is relatively unaffected ($\Delta\theta = \pm 10^\circ$) for isophotes with effective radii exceeding 2.9 arcseconds and the trend in orientation for isophotes with smaller effective radii is towards the semi-major axis of the convolved seeing function. These effects are not surprising since the seeing profile was convolved with an extended object and not a point source.

An obvious and important question which arises is whether this critical effective radius varies with the convolved point-spread function. Figure 8 illustrates the variation in axial ratio with effective radius of the base frame convolved with a point-spread function twice as elliptical as the maximum for the CFHT data. For this image, the effective radius where seeing effects upon isophotal shape becomes negligible is 4.9 arcseconds, which is 1.6 arcseconds larger than the previous critical value and the previously attained error of $\pm 10^\circ$ for isophotal orientation cannot be obtained at *any* effective radius for this image! (see Figure 9) Thus the effective radius where seeing effects upon isophotal shape and orientation becomes negligible is a function of the convolved point-spread function.

The critical effective radius for isophotal shape, when the *minimum* elliptical seeing function is convolved with the base frame, remains 3.3 arcseconds but decreases to 2.1 arcseconds for isophotal orientation (see Figures 10 and 11). Since isophotal shape is not computed to a sufficient degree of accuracy when the effective radius is less than 3.3 arcseconds, this effective radius will be used as a

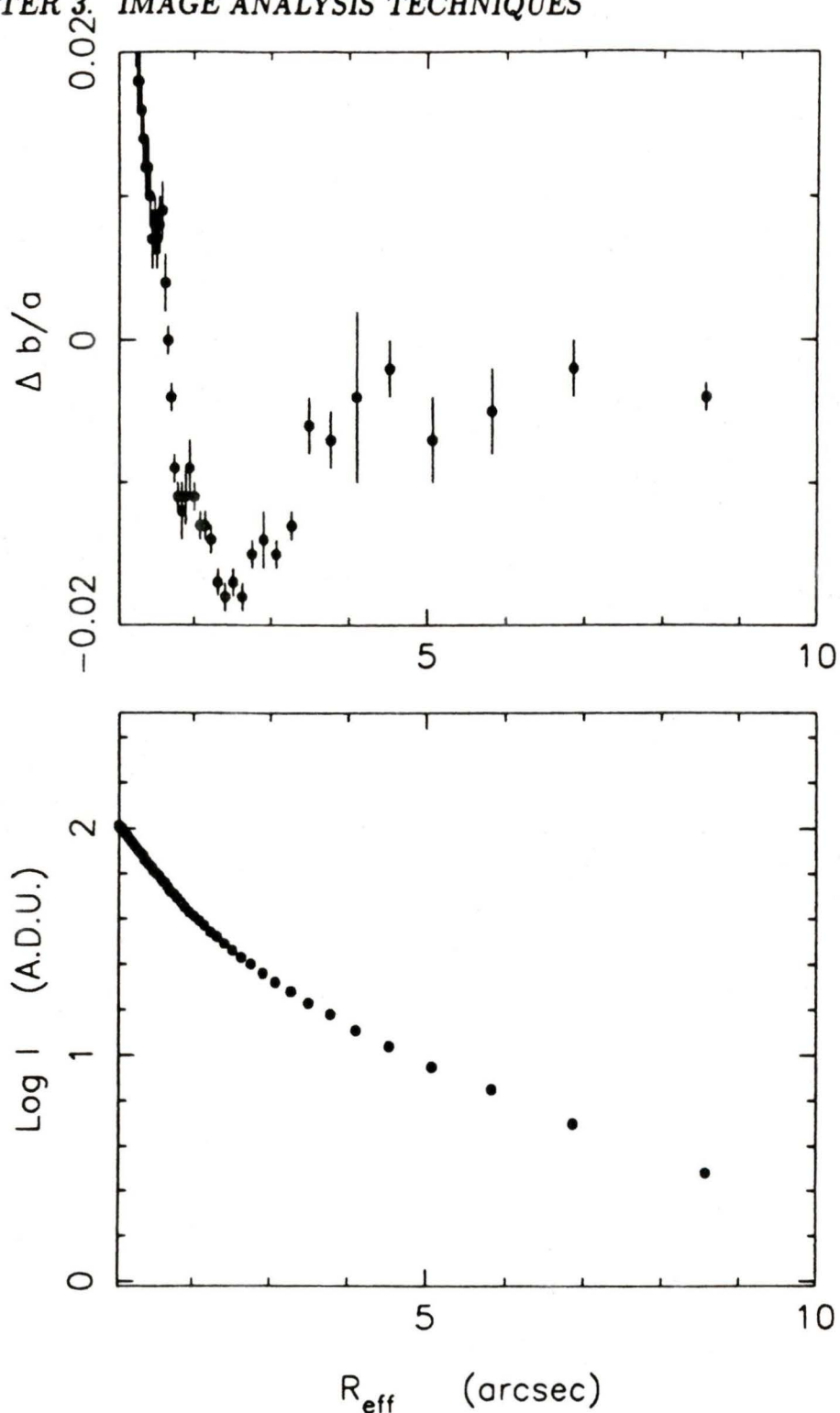


Figure 6: The residual isophotal axial ratio as a function of isophotal effective radius and the intensity profile of a model globular cluster convolved with an elliptical ($\epsilon = 1 - b/a = 0.20$) Gaussian function. The isophotal increment is 2 A.D.U.

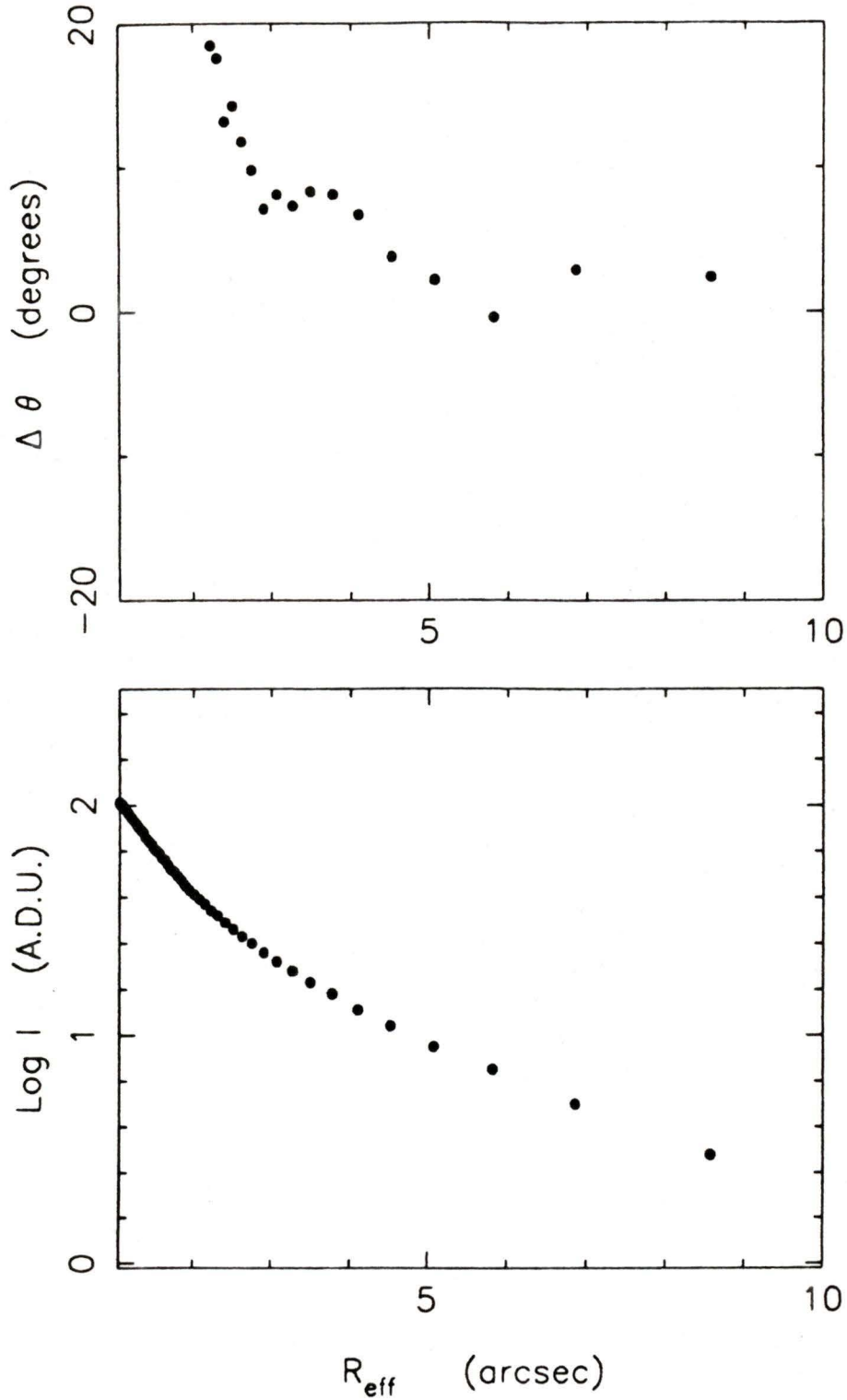


Figure 7: The residual orientation of the isophotal semi-major axis as a function of isophotal effective radius and the intensity profile of a model globular cluster convolved with an elliptical ($\epsilon = 1 - b/a = 0.20$) Gaussian function. The isophotal increment is 2 A.D.U. and the error bars are the size of the symbols.

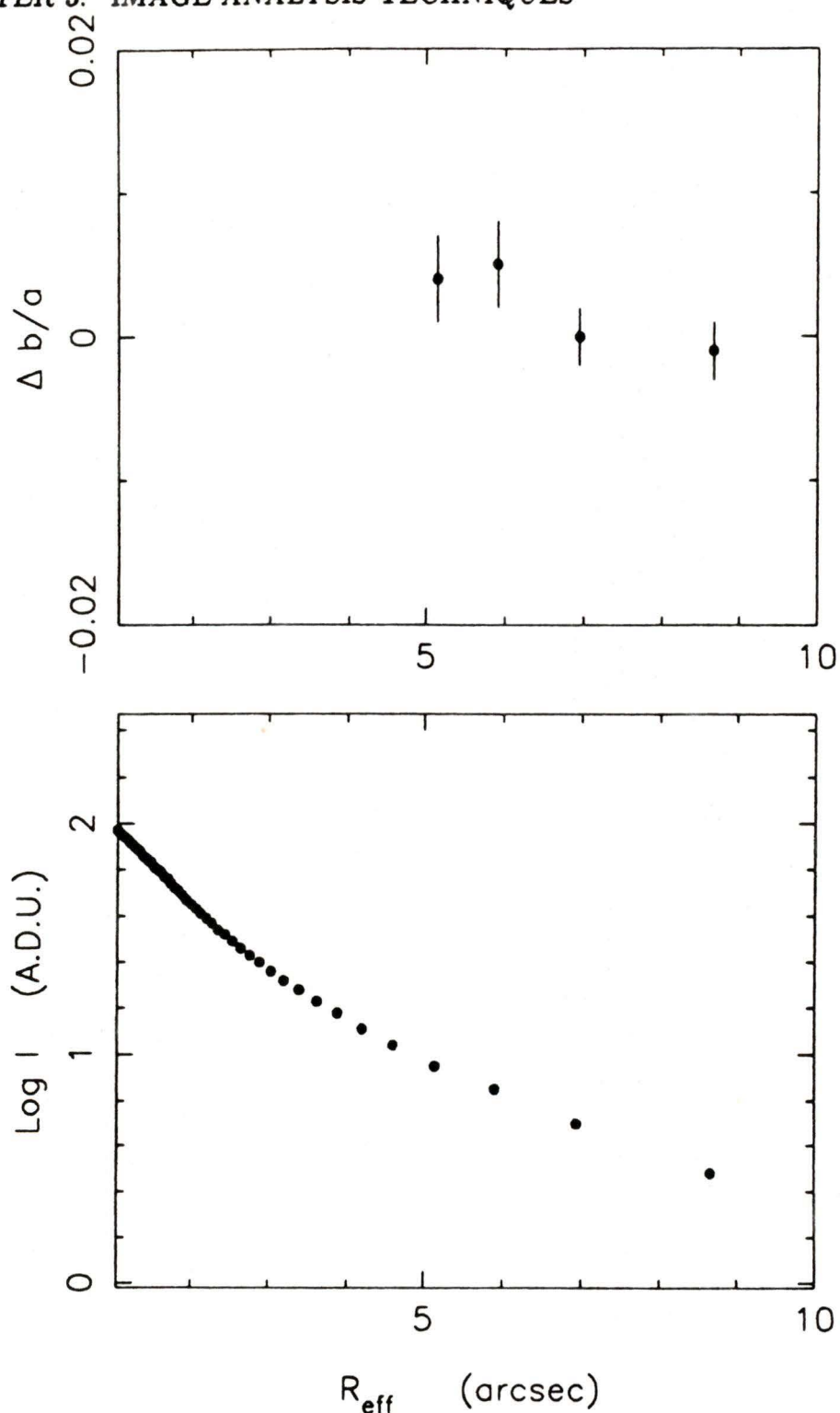


Figure 8: The residual isophotal axial ratio as a function of isophotal effective radius and the intensity profile of a model globular cluster convolved with an elliptical ($\epsilon = 1 - b/a = 0.40$) Gaussian function. The isophotal increment is 2 A.D.U.

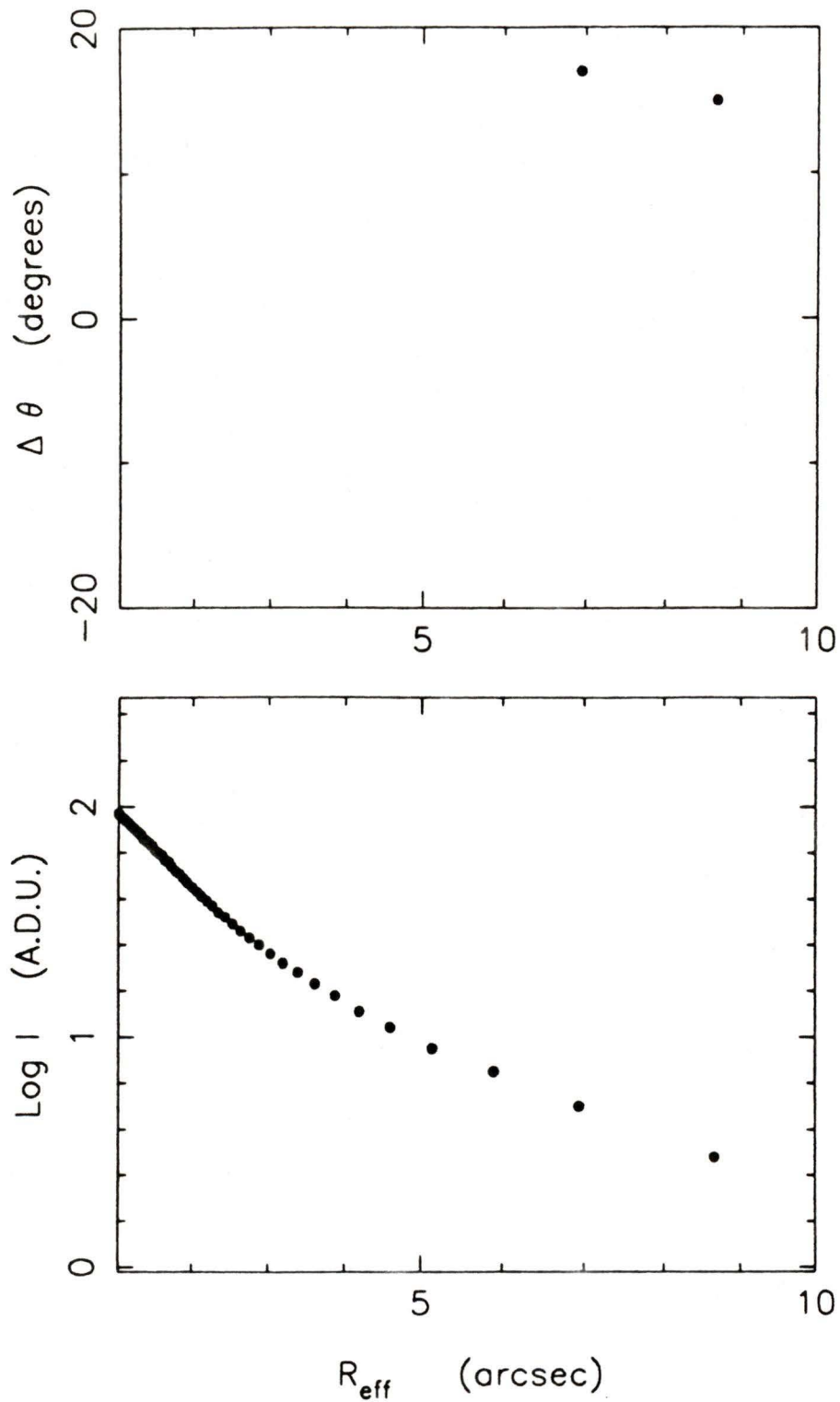


Figure 9: The residual orientation of the isophotal semi-major axis as a function of isophotal effective radius and the intensity profile of a model globular cluster convolved with an elliptical ($\epsilon = 1 - b/a = 0.40$) Gaussian function. The isophotal increment is 2 A.D.U. and the error bars are the size of the symbols.

critical value in the analysis of isophotal attributes for the CFHT CCD data of this project. When the CFHT images do not extend beyond this critical value, an approximate ellipticity and orientation will be obtained and the effect of the seeing upon these values noted. Magnifying these images using a bicubic spline interpolant would not improve the accuracy of the attributes since the critical value would be magnified by the same amount as the image. Hence isophotal shape and orientation would continue to be affected by the seeing profile, therefore preventing a sufficiently accurate determination of cluster attributes. To further complicate matters, the outermost isophotes of an image will be most strongly affected by the presence of noise and as Figures 12 and 13 indicate, the addition of a Gaussian noise spectrum of amplitude 4.2 A.D.U. (Equation 18) to the base frame greatly affects the accuracy of the determination of isophotal attributes.

In summary, isophotal attributes are computed when the isophotal effective radius exceeds 1.05 arcseconds. This constraint necessitates the application of a bicubic spline interpolant to the stellar images prior to the determination of isophotes for these images. Simulation of the seeing effects observed for the CFHT data in this project indicates that, in the absence of noise, the effects of the seeing profile upon isophotal attributes decrease as effective radius increases and a critical effective radius at which seeing effects become negligible can be specified for a given point-spread function. Simulation of the maximum and minimum elliptical seeing functions observed for the data in this project indicate isophotal axial ratio is determined within the desired accuracy of 1% for those isophotes with effective radii exceeding 3.3 arcseconds; isophotal orientation is computed within 10° of the known value for isophotes with effective radii exceeding this critical value. As Figures 14 and 15 demonstrate, this critical effective radius is independent of the size of the model globular cluster image. (The model globular in these figures was

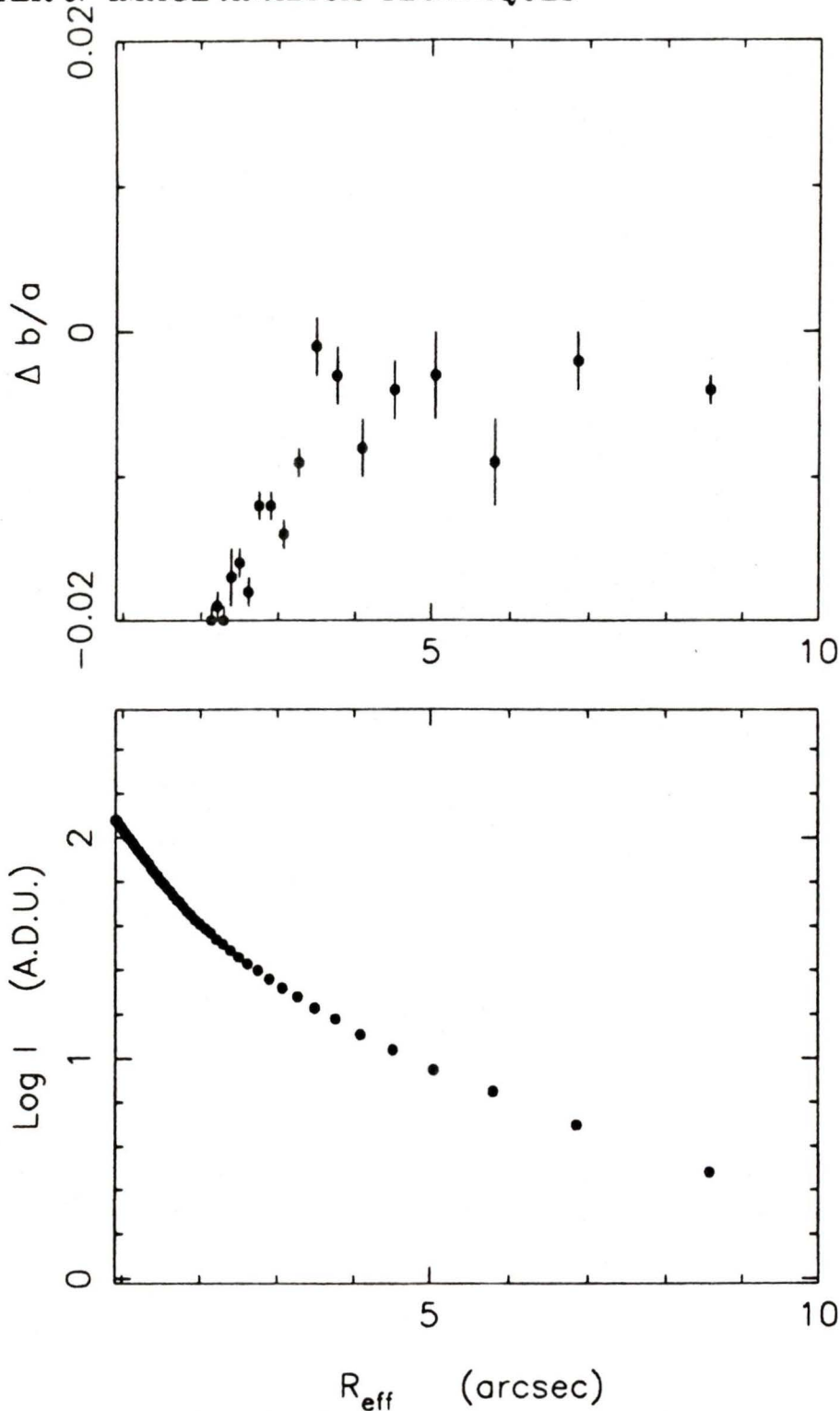


Figure 10: The residual isophotal axial ratio as a function of isophotal effective radius and the intensity profile of a model globular cluster convolved with an elliptical ($\epsilon = 1 - b/a = 0.01$) Gaussian function. The isophotal increment is 2 A.D.U.

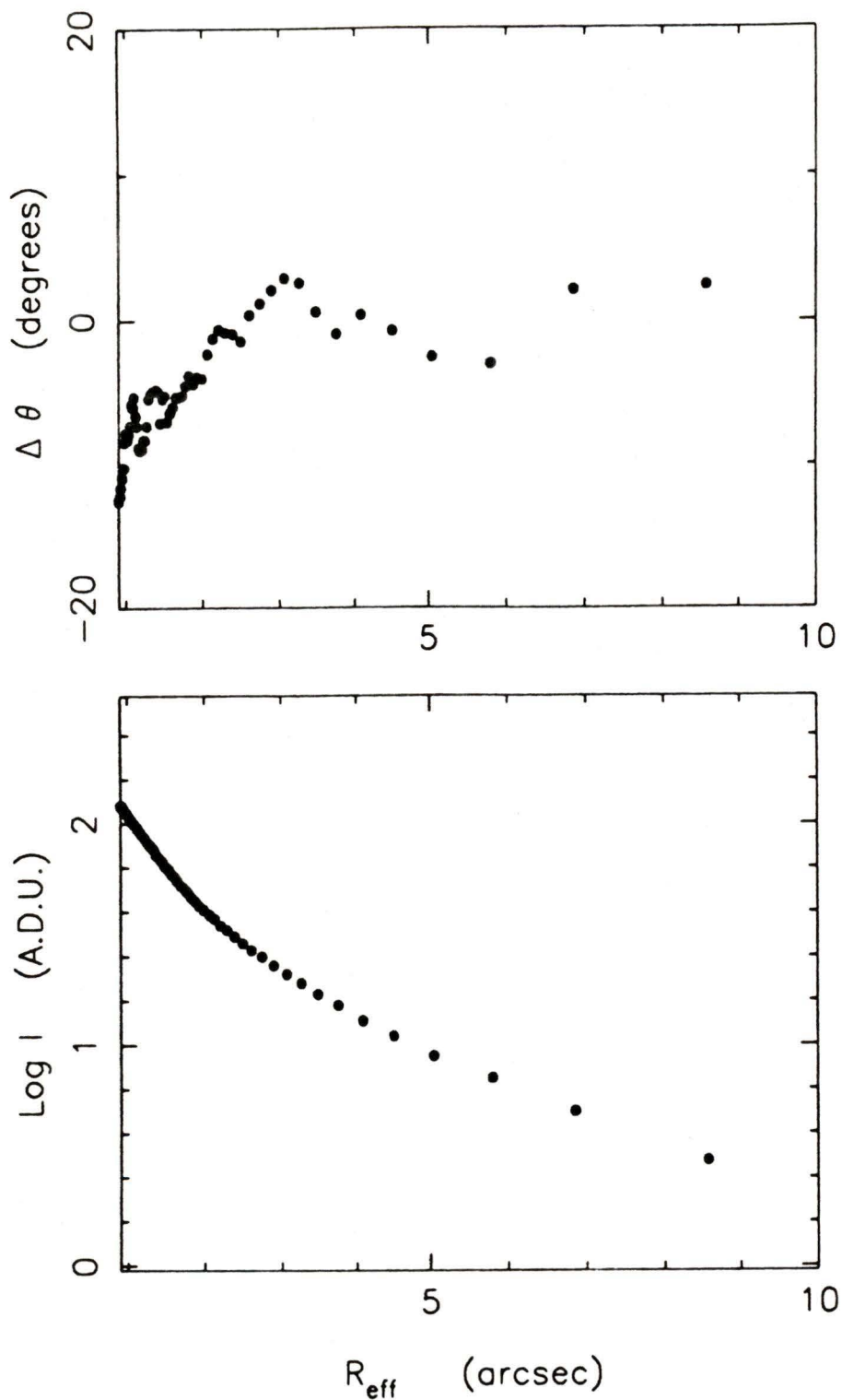


Figure 11: The residual orientation of the isophotal semi-major axis as a function of isophotal effective radius and the intensity profile of a model globular cluster convolved with an elliptical ($\epsilon = 1 - b/a = 0.01$) Gaussian function. The isophotal increment is 2 A.D.U. and the error bars are the size of the symbols.

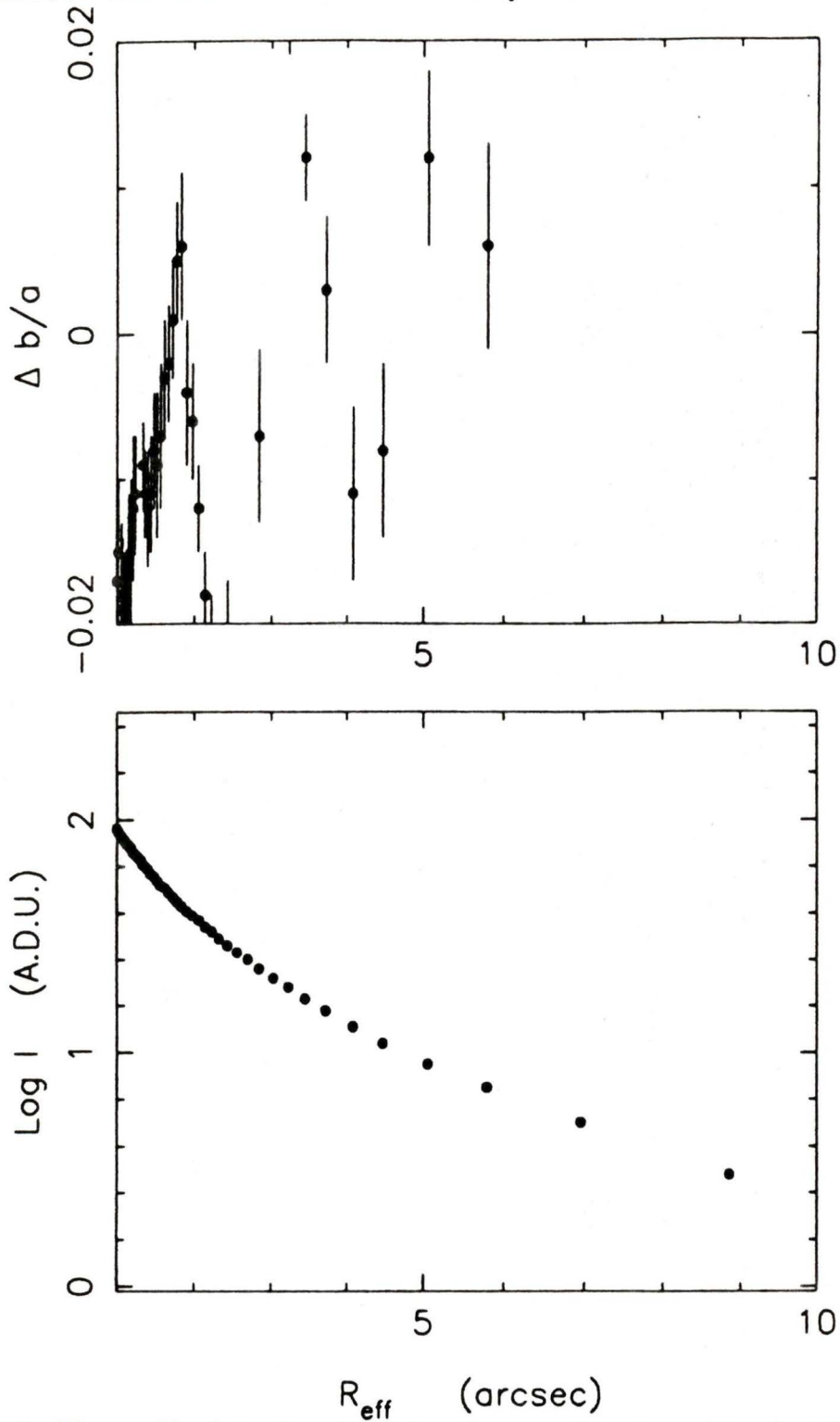


Figure 12: The residual isophotal axial ratio as a function of isophotal effective radius and the intensity profile of a model globular cluster with a Gaussian noise spectrum of amplitude 4.2 A.D.U. The isophotal increment is 2 A.D.U. and the error bars are calculated from the residuals of the fit of an ellipse to the isophote.

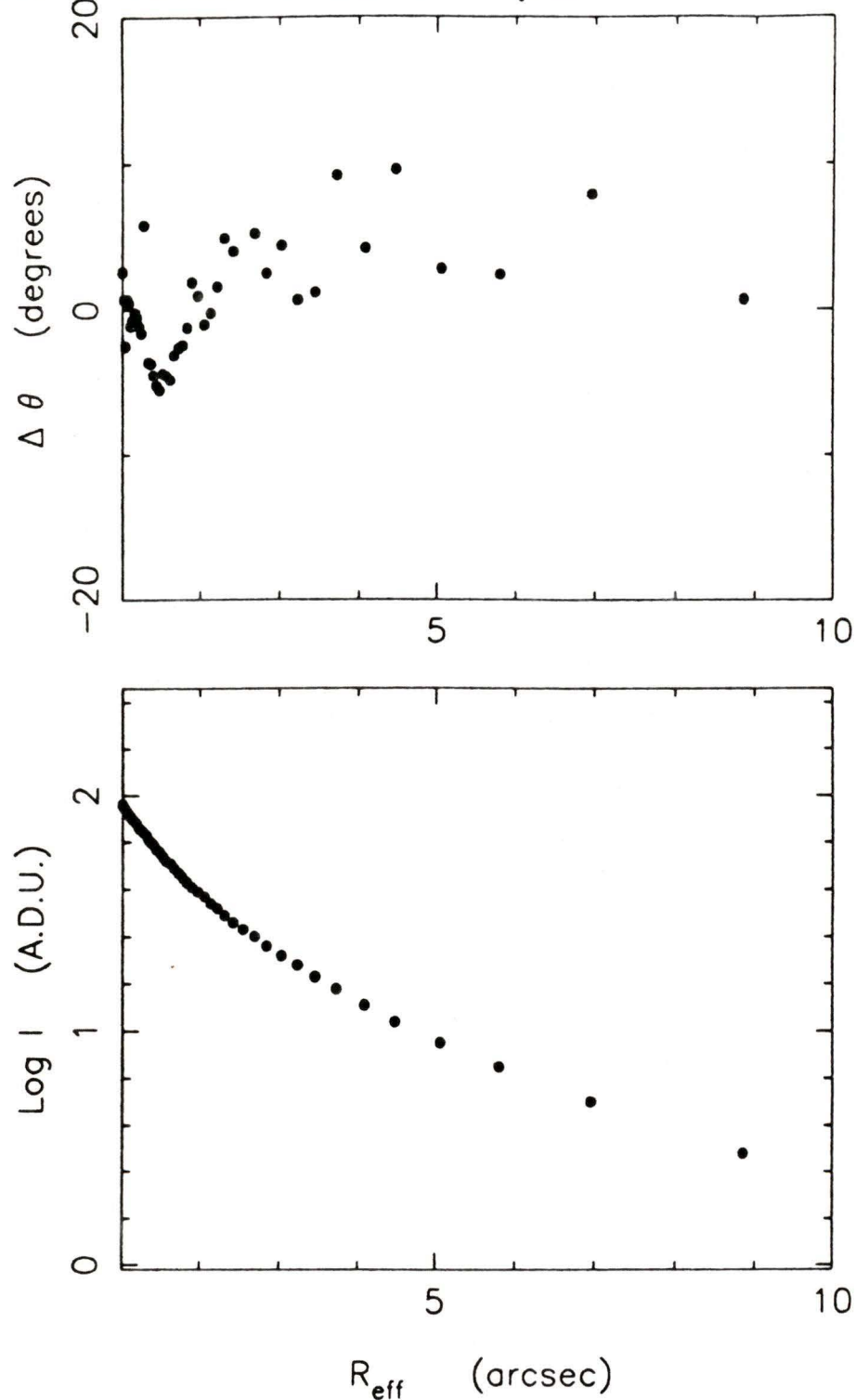


Figure 13: The residual orientation of the isophotal semi-major axis as a function of isophotal effective radius and the intensity profile of a model globular cluster with a Gaussian noise spectrum of amplitude 4.2 A.D.U. The isophotal increment is 2 A.D.U. and the error bars are the size of the symbols.

created by expanding and contracting the base frame respectively and convolving the image with the maximum seeing profile in Table 1.) For those CFHT CCD images in this project which do not extend beyond the critical effective radius of 3.3 arcseconds, an ellipticity and orientation will be estimated and the effects of seeing upon these values noted.

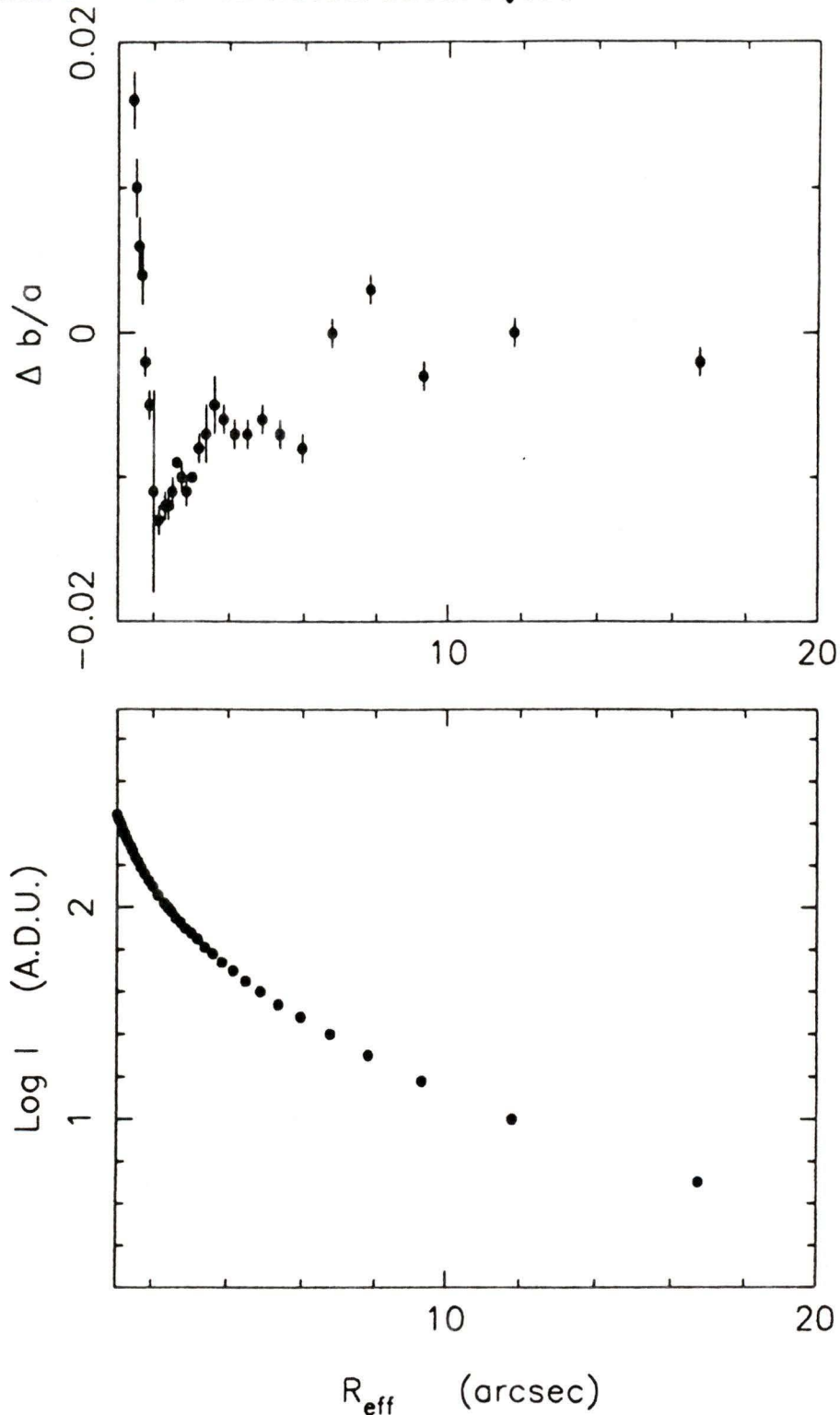


Figure 14: The residual isophotal axial ratio as a function of isophotal effective radius and the intensity profile of a model globular cluster convolved with an elliptical ($\epsilon = 1 - b/a = 0.20$) Gaussian function. This model is twice the size of the base frame. The isophotal increment is 10 A.D.U.

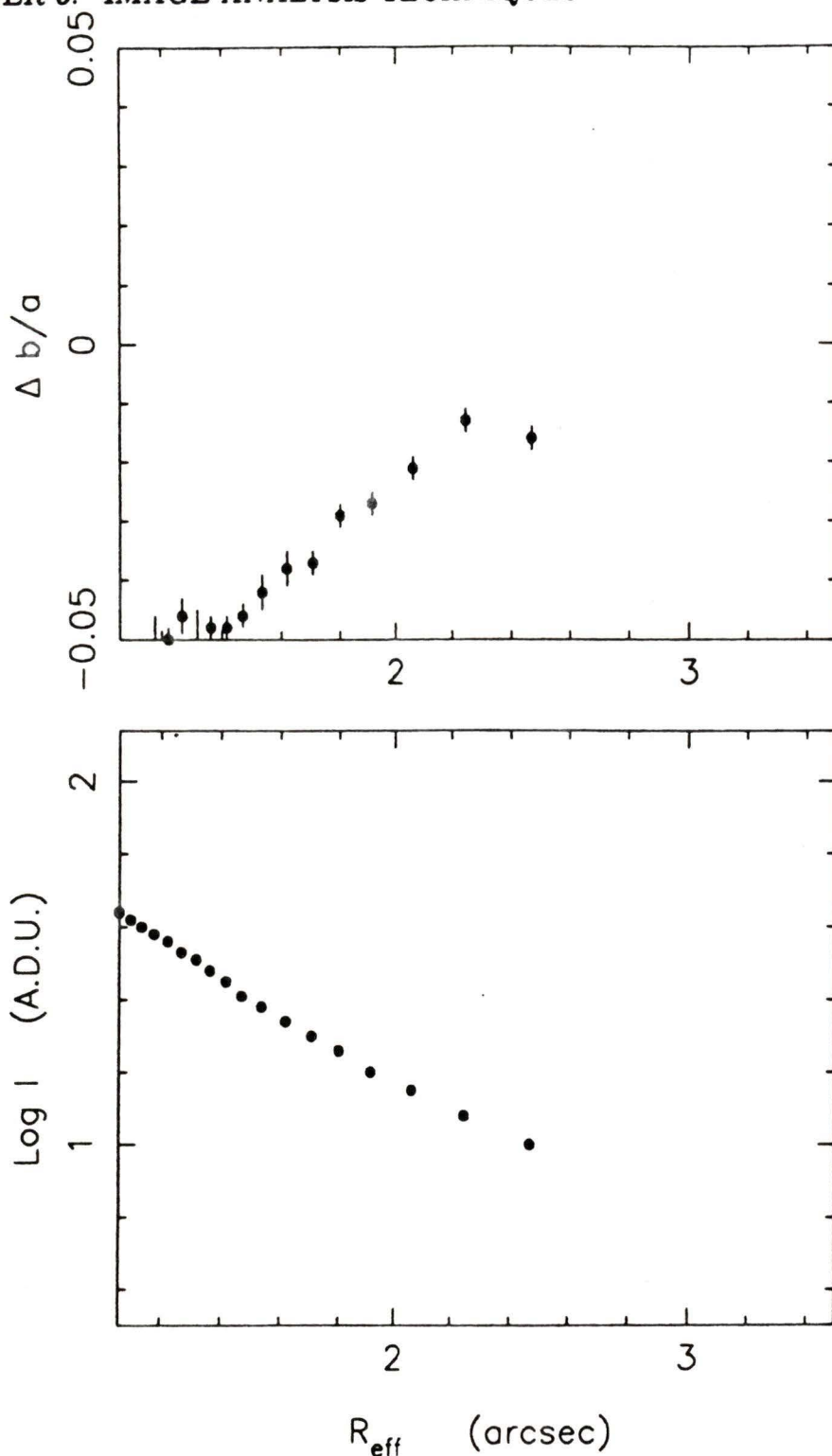


Figure 15: The residual isophotal axial ratio as a function of isophotal effective radius and the intensity profile of a model globular cluster convolved with an elliptical ($\epsilon = 1 - b/a = 0.20$) Gaussian function. This model is one-third the size of the base frame. The isophotal increment is 2 A.D.U.

3.2 The Moment Method

In most astronomical systems, the physical conditions affecting the distribution of a variable are of a continuous nature. For physical reasons we shall therefore generally assume the *relative frequency distribution* $\Phi(x)$ to be a smooth, continuous, bounded, non-negative function existing everywhere in the interval $-\infty$ to $+\infty$ or any other interval specifically stated. The quantity $\Phi(x)$ is the observed frequency of the result divided by the total number of times the result could have been observed; it represents the average fraction, or proportion, of the observations with a given value. The relative frequency function is defined in such a way that

$$\int_{-\infty}^{+\infty} \Phi(x) dx = 1 \quad (22)$$

In the case of a two-dimensional or bivariate distribution, the relative frequency function is given by $\Phi(x, y)$. Such a frequency function can be used to represent the average number of photons recorded by a CCD detector in pixel (x, y) . Specifically,

$$\Phi(x, y) = \frac{I(x, y)}{\iint I(x, y) dx dy} \quad (23)$$

where $I(x, y)$ is the flux in Analog-to-Digital Units (A.D.U) recorded in pixel (x, y) .

Some of the important features of a distribution may be described by its mean, or expectation, and by its moments. The expectation of a function $f(x, y)$ of the two variables x, y which has a given frequency function $\Phi(x, y)$ is defined by

$$E[f(x, y)] = \int_{-\infty}^{+\infty} \int_{-\infty}^{+\infty} f(x, y) \Phi(x, y) dx dy \quad (24)$$

The existence of such a mean presupposes that $f(x, y)$ is integrable with respect to $\Phi(x, y)$ over the entire x, y plane. The expectations of the non-fractional positive powers of the variable are termed the *general moments* of the function and are given by

$$E(x^i, y^k) = \int_{-\infty}^{+\infty} \int_{-\infty}^{+\infty} x^i y^k \Phi(x, y) dx dy \quad (25)$$

where i and k may take the values of all positive integers. The sum $i + k$ is called the *order* of the moment. Moments may also be taken about any arbitrary point; of special interest are the *central moments* formed around the general means x_o, y_o of the distribution. These moments are defined as:

$$M_{i,k} = E[(x - x_o)^i, (y - y_o)^k] = \int_{-\infty}^{+\infty} \int_{-\infty}^{+\infty} (x - x_o)^i (y - y_o)^k \Phi(x, y) dx dy \quad (26)$$

The point (x_o, y_o) is the centroid of the entire distribution and the central moments $M_{2,0}$ and $M_{0,2}$ represent the variances of x and y respectively; $M_{1,1}$ is the covariance of x and y . When considering CCD data, the two variables x and y represent position coordinates in a plane and a rotation of the coordinate system is possible and has a physical meaning. Hence, the variances of x and y , which depend on the arbitrary orientation of the coordinate system, are then not significant features of the distribution. An objective description must be based on parameters that are independent of the particular coordinate system used.

Trumpler and Weaver (1953) define the normal frequency function in which the variables become stochastically independent and derive the following expressions for the centroid, eccentricity and orientation of the distribution in terms of the central moments upon translation back to the the original x, y coordinate system:

$$x_o = \int \int x \Phi(x, y) dx dy \quad (27)$$

$$y_o = \int \int y \Phi(x, y) dx dy \quad (28)$$

$$e = \left(1 - \frac{M_{2,0} + M_{0,2} - \sqrt{(M_{2,0} + M_{0,2})^2 + 4M_{1,1}^2}}{M_{2,0} + M_{0,2} + \sqrt{(M_{2,0} + M_{0,2})^2 + 4M_{1,1}^2}} \right)^{\frac{1}{2}} \quad (29)$$

$$\tan \theta = \frac{2M_{1,1}}{M_{0,2} + \sqrt{(M_{2,0} + M_{0,2})^2 + 4M_{1,1}^2}} \quad (30)$$

Replacing $\Phi(x, y)$ by equation 23 in the expression defining the central moments of a distribution (equation 26) and using equations 27 through 30 permits the computation of the centroid, shape and orientation of CCD images. These relations, which were incorporated in the image processing software package VISTA written by Tod Lauer of Princeton University, were employed in the analysis of the M31 globular clusters of this project listed in Table 2.

3.2.1 The Software

The only input parameters required by Lauer's program are the CCD frame to be processed, the pixel coordinates of a region on the frame which encloses the image whose centroid, ellipticity and orientation are to be determined and a threshold or background sky level for the frame. The intensity threshold specified for the CFHT CCD observations was the median of pixel values in the frame. This value was estimated by an iterative outlier rejection technique in R2D2 where the tolerance for rejection was 2.3σ (see Section 3.1.1).

Prior to calculating the relative frequency function of the image defined in Equation 23, VISTA subtracts the specified threshold or sky level from the intensity recorded in each pixel. This subtraction reduces each frame to a zero intensity level. If the difference in intensities is zero or negative, the pixel is not included in the calculation of the relative frequency function. Thus only those pixels with an intensity level exceeding the specified threshold or sky value will be included in the calculation of the image's centroid, shape and orientation.

3.2.2 Limitations of the Moment Method

In order to ascertain the limitations of Lauer's software in the determination of the shape and orientation of CCD images, several artificial CCD frames which simulate the CFHT data of this project were analyzed. These are the same frames used to determine the limitations of the Isophotal Method in Section 3.1.3 and are described in Section 3.1.2. As before, the term "base frame" shall refer to the frame containing the model globular cluster and several point sources of various intensities.

The dependence of the calculated image attributes upon the size of the region enclosing the image was explored using the model globular cluster of known ellipticity, position angle and centroid created using R2D2. This globular, which simulates the M31 globular cluster images in this project, was analyzed for a wide range of regions. Since the deviation of M31 globular cluster shape from circularity is expected to be small, the error in the determination of cluster shape on the simulated frames by the moment method should not exceed 1% as this is the anticipated scale of ellipticity variation among clusters (see for example Table I in Spassova *et al.*, 1988). The desired degree of accuracy in the determination of ellipticity using VISTA is obtained for regions containing in excess of 50 pixels as demonstrated in Figure 16. The corresponding error in image orientation is $\pm 5^\circ$ for regions containing in excess of 50 pixels (see Figure 17).

Each randomly-shaped quadrilateral region containing N pixels was centered on the image and the threshold intensity level specified for each integrating region was 5 A.D.U. When $N < 350$ pixels, only a portion of the CCD image is enclosed by the specified region, therefore the number of pixels enclosed corresponds to the number of pixels employed in the computation of image moments. Hence, image attributes cannot be determined with sufficient accuracy using this moment method when a

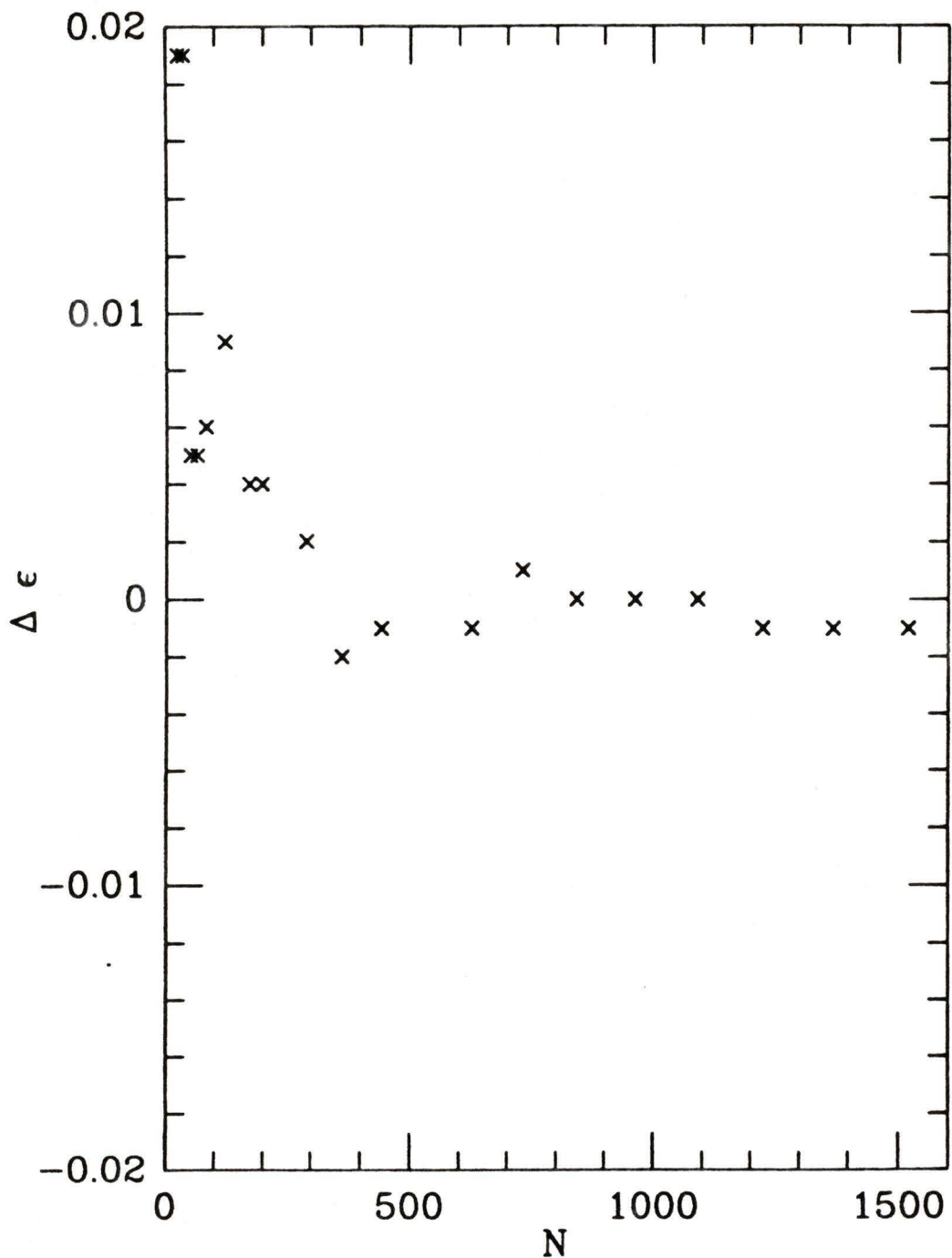


Figure 16: The residual ellipticity calculated for model globular cluster data over the specified region containing N pixels and centered on the image. A threshold level of 5 A.D.U. was specified. Image shape is determined to a sufficient accuracy for regions containing in excess of 50 pixels.

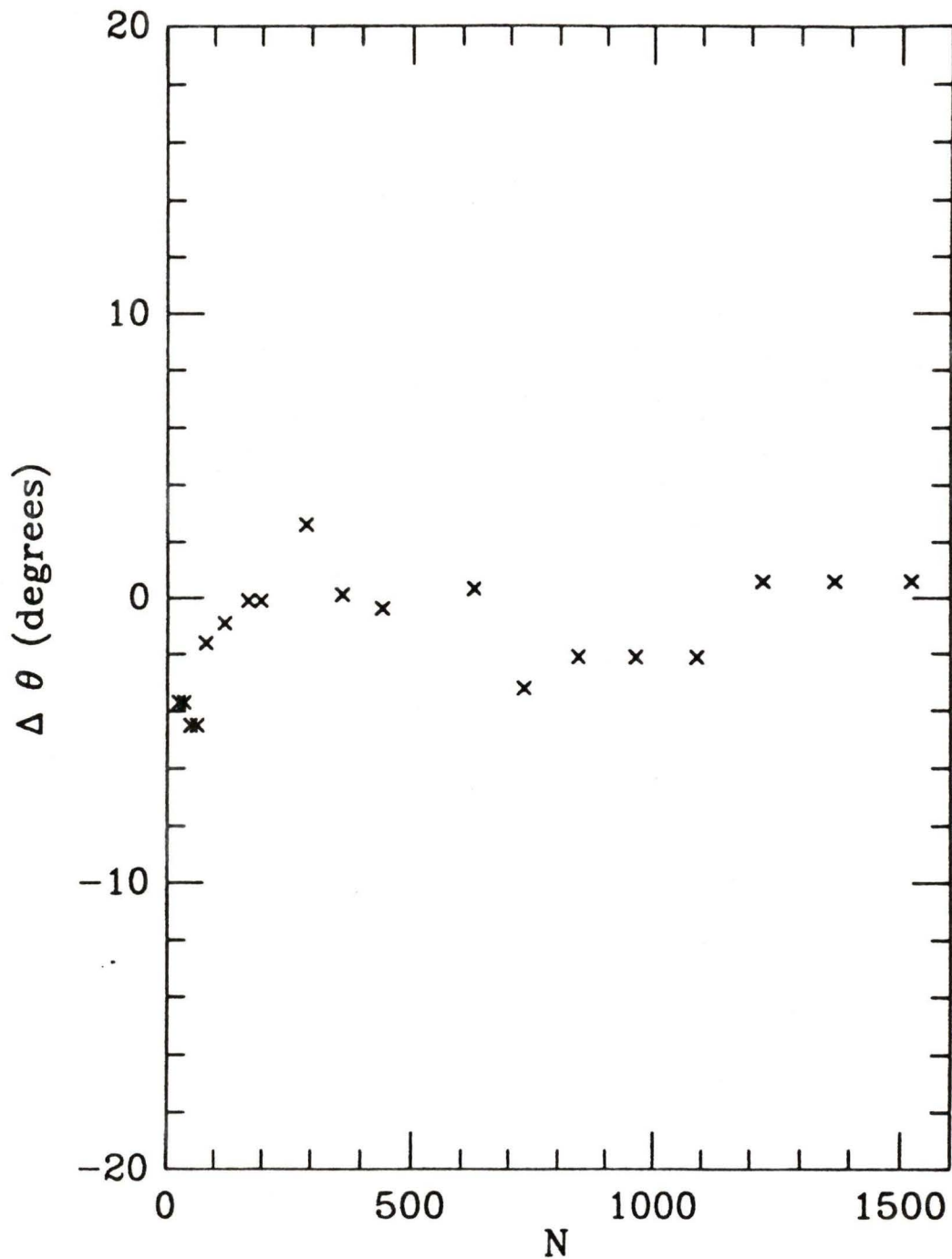


Figure 17: The residual orientation of the semi-major axis calculated for model globular cluster data over the specified region containing N pixels and centered on the image. A threshold level of 5 A.D.U. was specified.

CCD image is composed of fewer than 50 pixels. It should be noted that the model globular cluster being analyzed is uniform in shape and orientation. This is not necessarily true for the globular clusters of M31 (see, for example, Lupton 1989). The inclusion of more than one image in the specified region would prevent an accurate determination of the central moments and therefore produce an incorrect description of the shape and orientation of the globular cluster. The addition of a Gaussian noise spectrum of amplitude 4.2 A.D.U. (see Equation 18) to the base frame has a minimal effect upon the computation of image attributes as Figures 18 and 19 illustrate. The base frame is represented by the boxes and N is the number of pixels contained in the specified region.

The decrease in accuracy of the determination of image attributes for regions containing fewer than 50 pixels is unimportant for large images but prevents the accurate determination of image shape and orientation for small images such as stars just as in the isophotal method. Application of a bicubic spline interpolant, as described in Section 3.1.3, to the stellar images produces a magnified stellar image of a sufficient size to permit the accurate determination of image attributes by VISTA as demonstrated in Figure 20. Recall that the point-spread function defines the stellar image and the calculated attributes of stellar images therefore describe the convolved seeing function (see Appendix A). Figure 21 demonstrates the high degree of accuracy in the determination of stellar shape and orientation for a point source convolved with an elliptical ($\epsilon = 0.20$) seeing function. In this instance the convolved Gaussian function corresponds to the maximum elliptical seeing profile observed for the CFHT data of this project (see Table 2).

The central region of a globular cluster when subjected to seeing effects as defined in Appendix A, is analogous to a convolved stellar image. Hence the calculated shape and orientation of the bright inner region of a globular cluster image

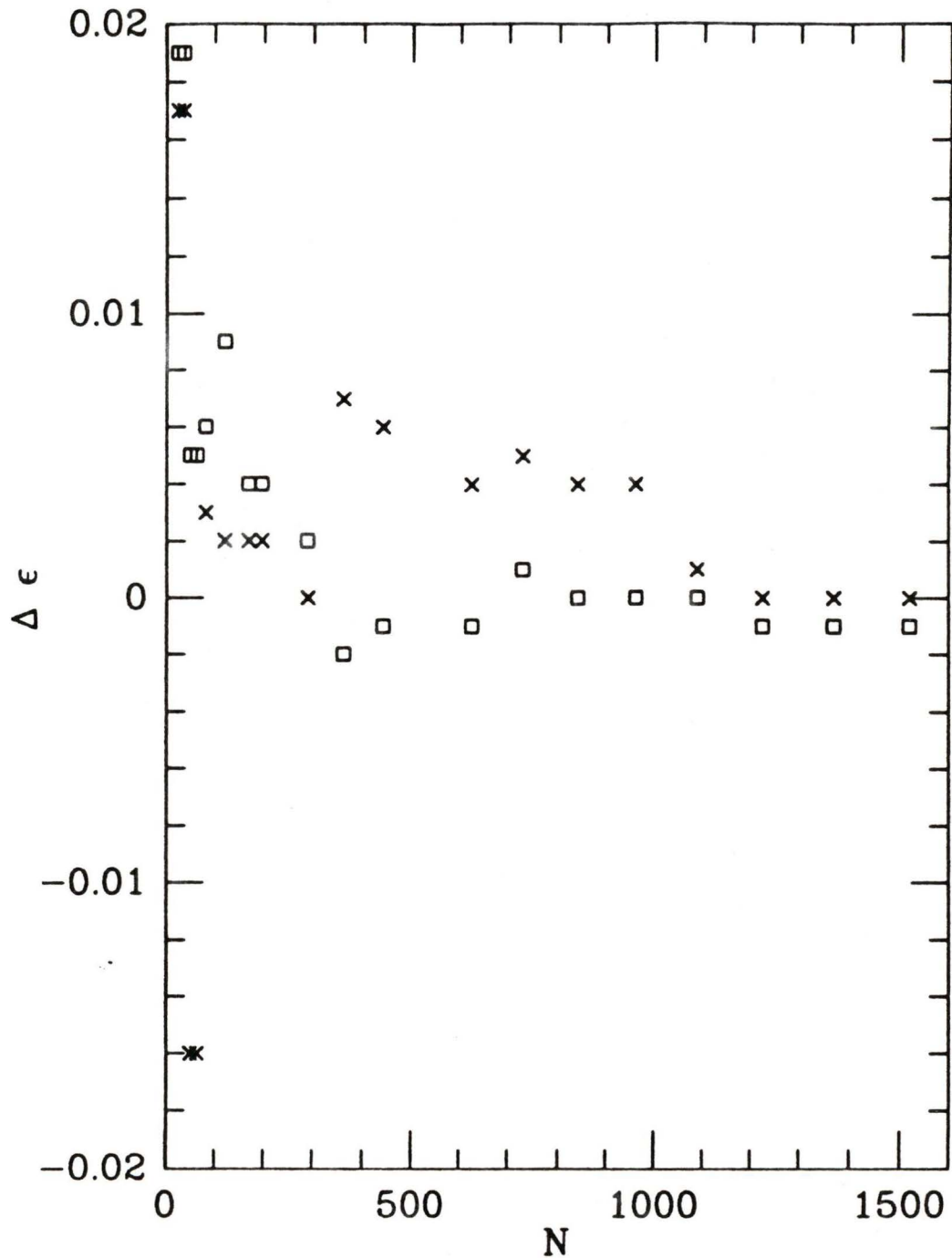


Figure 18: The addition of a Gaussian noise spectrum to the model globular cluster (crosses) has little effect upon the calculation of image ellipticity. The boxes represent the noise-free data. A threshold level of 5 A.D.U. was specified and the region containing N pixels was centered on the image.

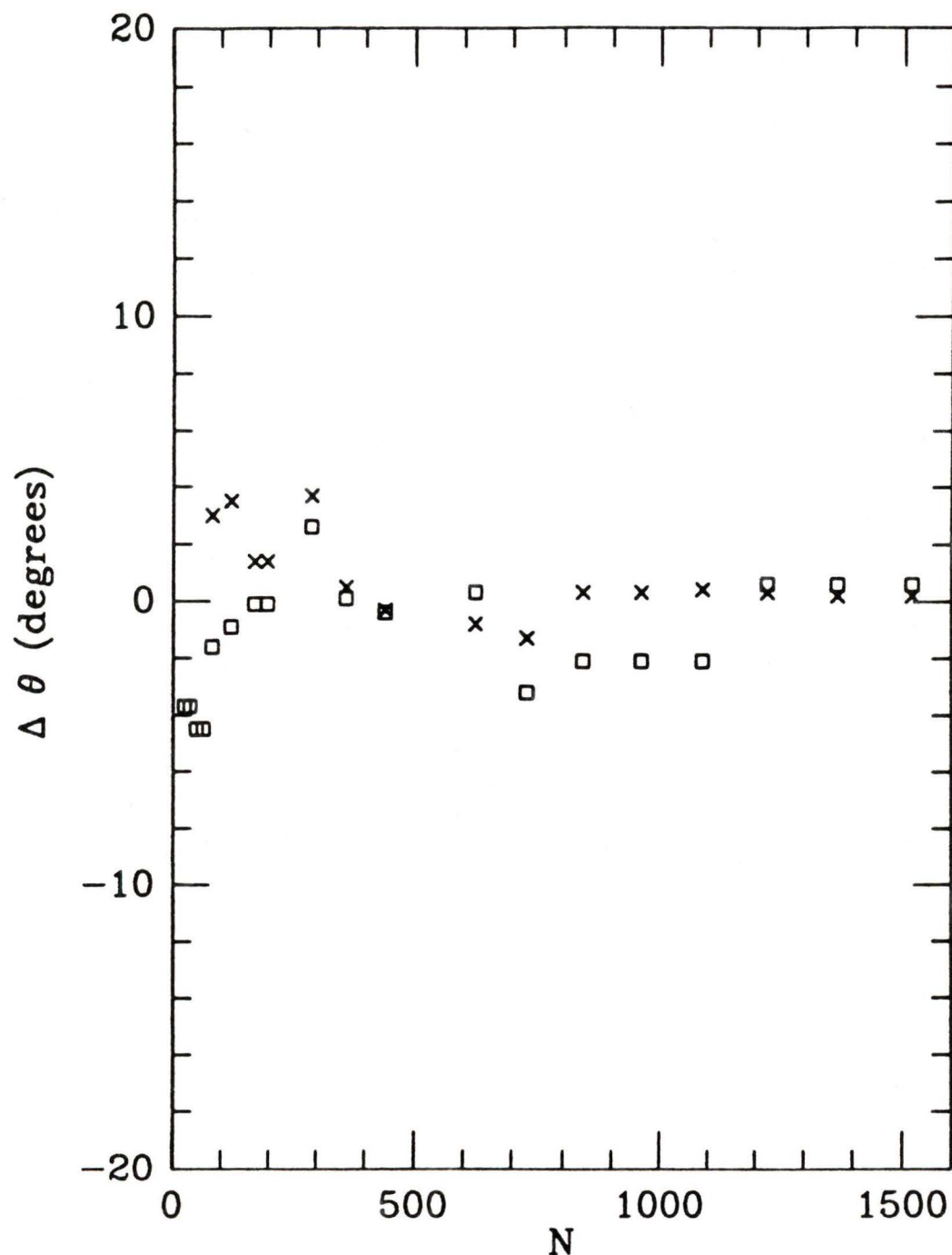


Figure 19: The addition of a Gaussian noise spectrum to the model globular cluster (crosses) has little effect upon the calculation of image orientation. The boxes represent the noise-free data. A threshold level of 5 A.D.U. was specified and the region containing N pixels was centered on the image.

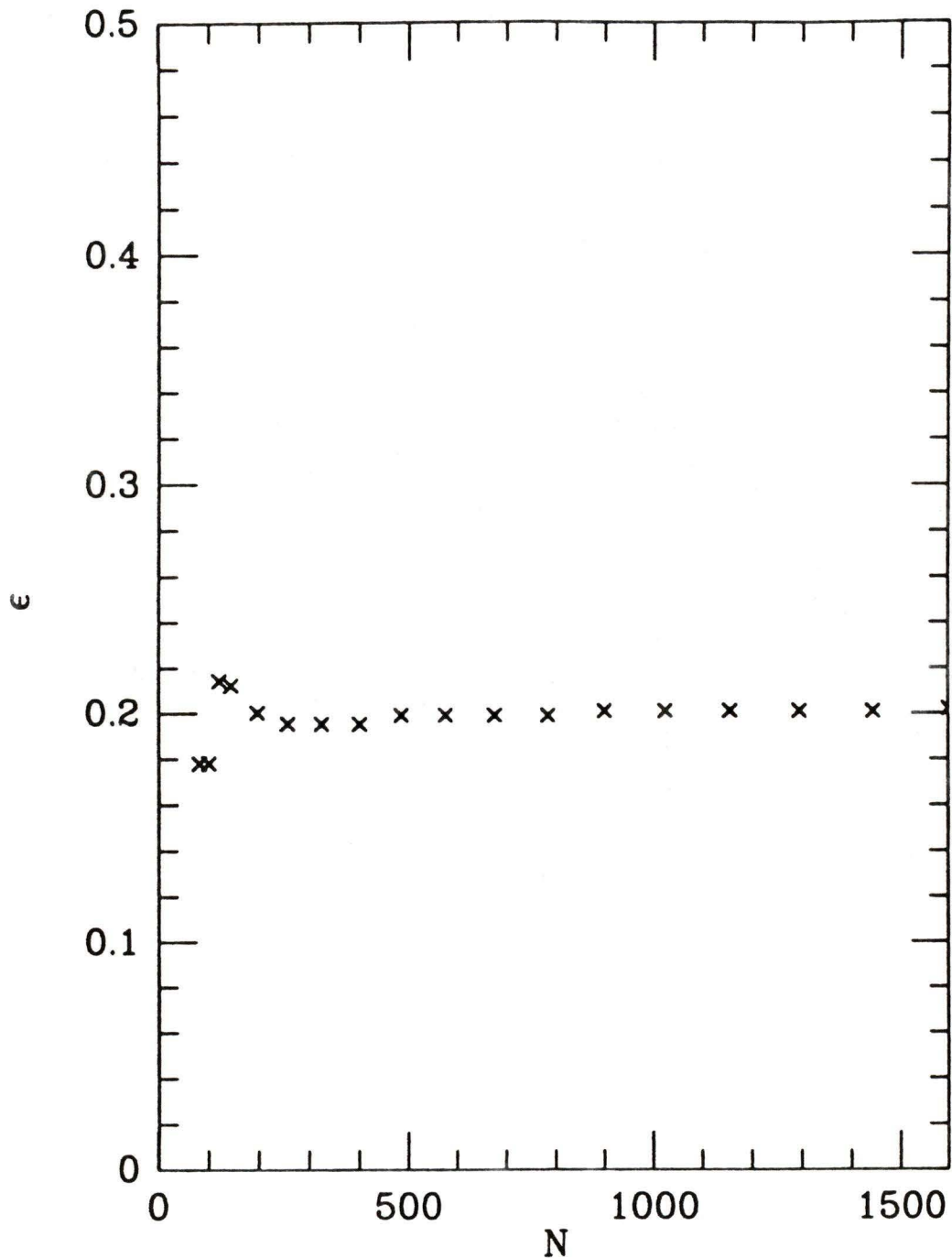


Figure 20: The residual ellipticity calculated for a point source convolved with an elliptical ($\epsilon = 0.20$) Gaussian function. A threshold level of 5 A.D.U. was specified and the region containing N pixels was centered on the stellar image.

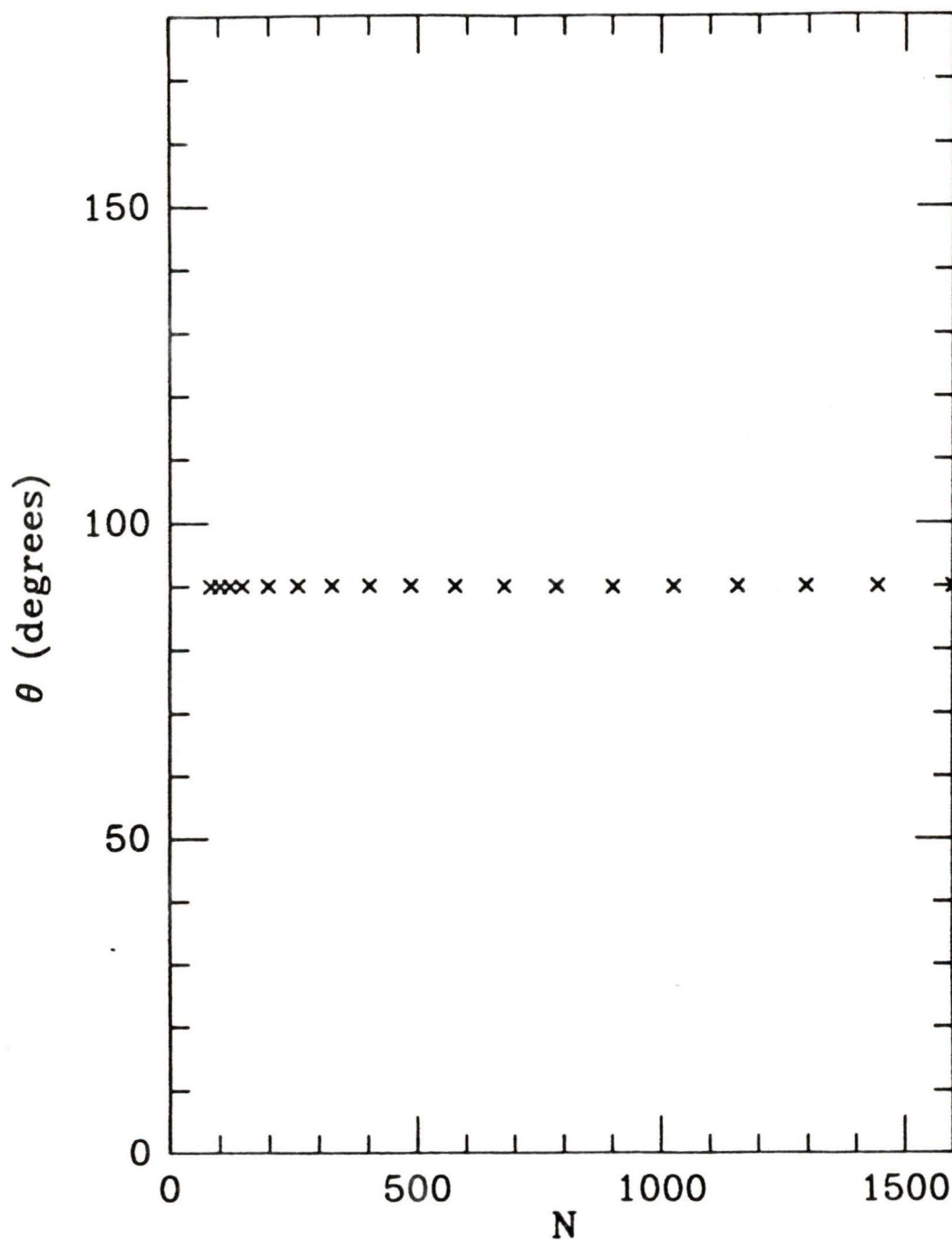


Figure 21: The residual orientation calculated for a point source convolved with an elliptical ($\epsilon = 0.20$) Gaussian function. A threshold level of 5 A.D.U. was specified and the region containing N pixels was centered on the stellar image.

will be that of the convolved seeing function. Since this moment method employs intensity-weighted moments in the calculation of image attributes, the convolved seeing function will strongly bias the computation of cluster shape and orientation.

An important property of the moment method not shared by the isophotal method, is the ability to remove guiding errors by subtracting averaged stellar moments from the cluster moments prior to the calculation of cluster shape and orientation (Valdes *et al.*, 1983). In particular,

$$M_{i,k}^r = M_{i,k}^o - \langle M_{i,k}^s \rangle \quad (31)$$

where the superscripts r , o , and s refer to the resultant (smearing subtracted), observed and stellar moments respectively.

The improvement in the determination of image shape and orientation is illustrated in Figures 22 through 25 where I is the specified sky or threshold level and the cross represents the convolved base frame prior to smearing-subtraction (*i.e.*, prior to the application of equation 31. The average stellar moments were computed using three convolved point sources on the model CCD frames. In figures 22 and 23, the convolved function was an elliptical ($\epsilon = 0.20$) Gaussian. In figures 24 and 25 the convolved Gaussian function was nearly circular ($\epsilon = 0.01$). The shapes of these functions correspond, respectively, to the maximum and minimum elliptical seeing functions observed for the CFHT CCD data in this project (see Table 2).

As illustrated in these figures, the accuracy of the moment method is improved as a result of the application of Equation 31 but the calculation of image attributes continues to be biased at large intensities when the convolved function is elliptical. As Table 2 indicates, the seeing function observed for the CFHT data of this project is generally elliptical in shape. An additional bias introduced in the computation of globular cluster shape by the moment method is the observation that globulars

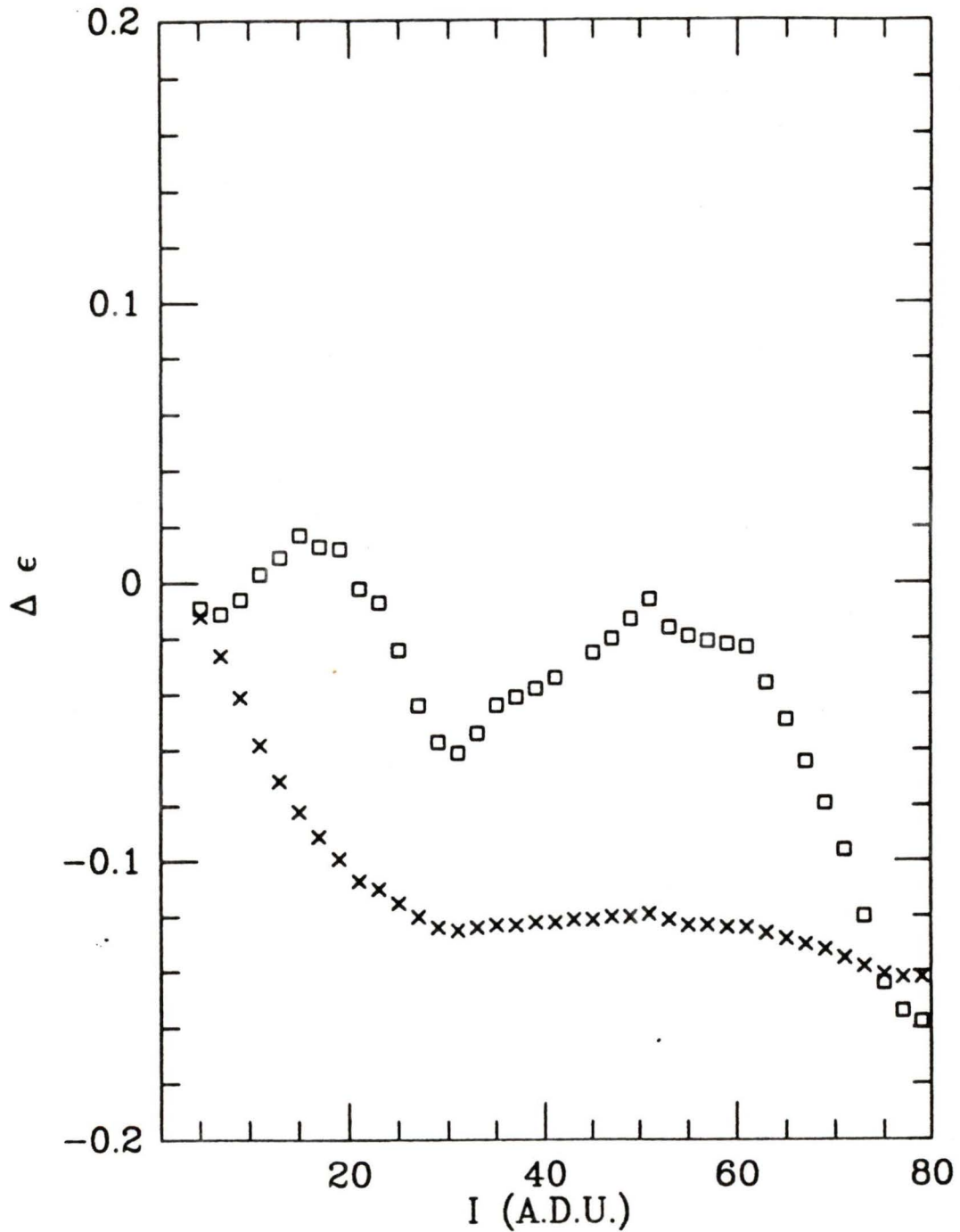


Figure 22: The residual ellipticity of a model globular cluster convolved with an elliptical ($\epsilon = 0.20$) Gaussian function (crosses). The boxes represent the ellipticity calculated at specified threshold intensities, I , when smearing-subtracted moments were employed. The region enclosing the image was constant in size.

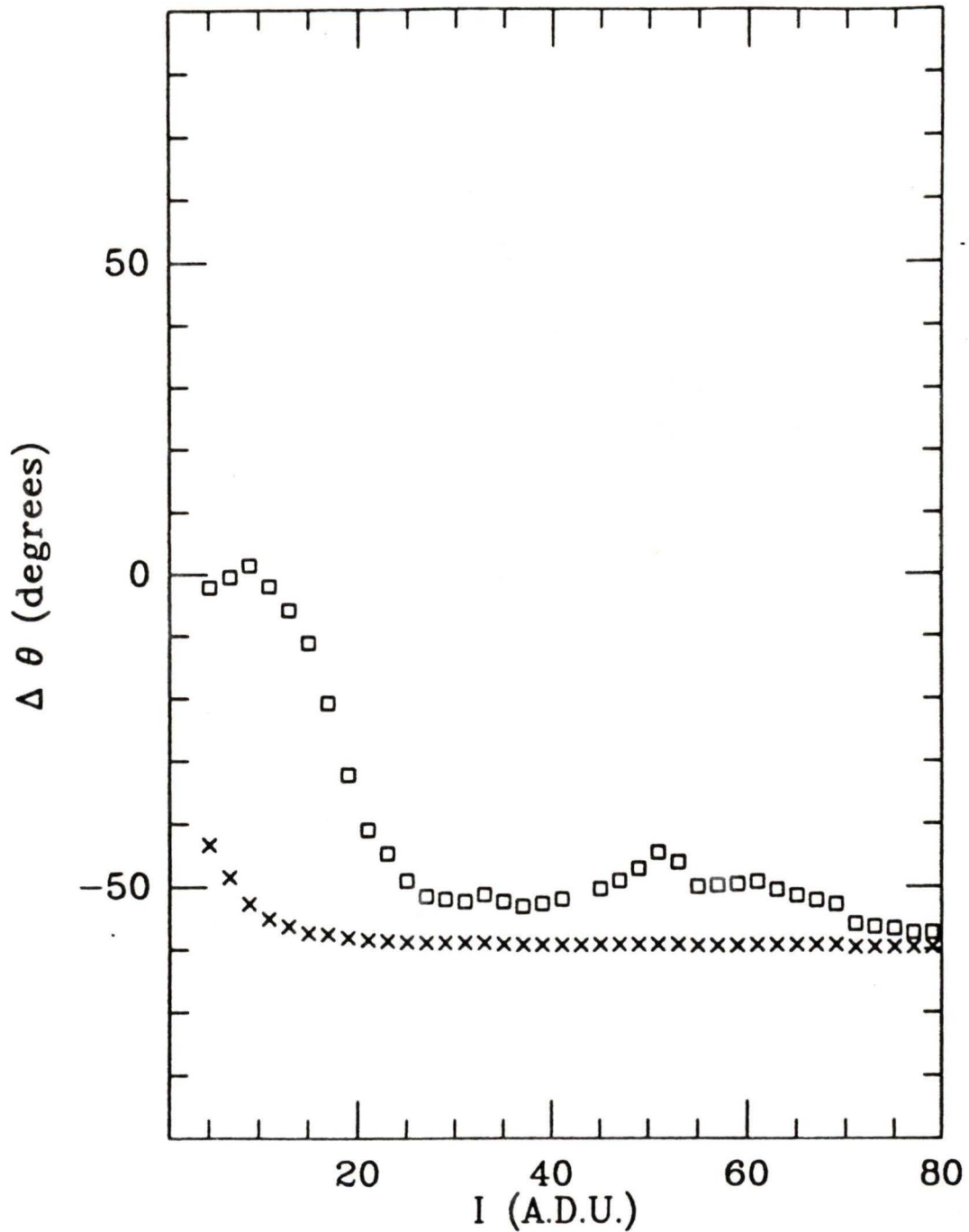


Figure 23: The residual orientation of the semi-major axis of a model globular cluster convolved with an elliptical ($\epsilon = 0.20$) Gaussian function (crosses). The boxes represent the orientation calculated at specified threshold intensities, I , when smearing-subtracted moments were employed. The region enclosing the image was constant in size.

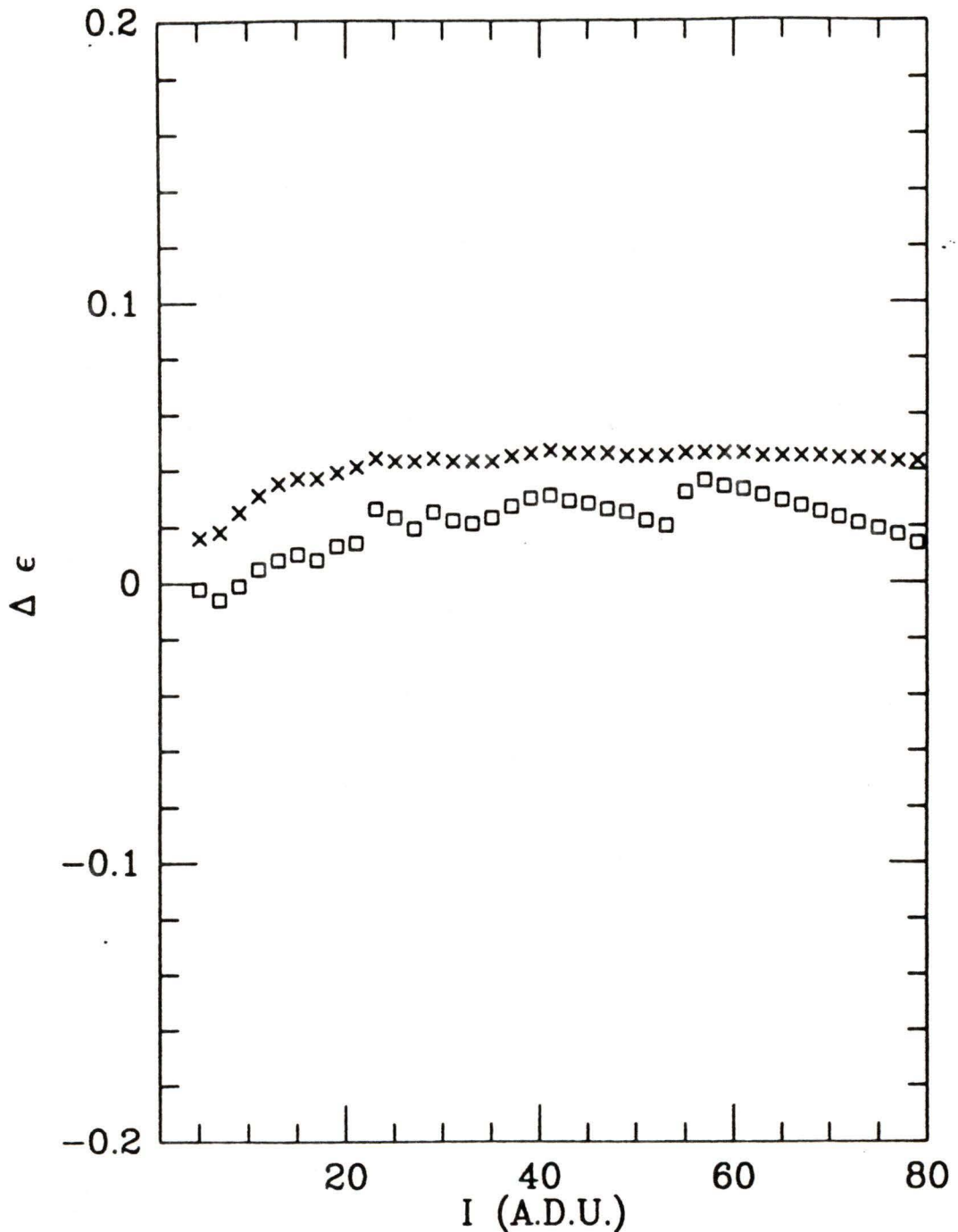


Figure 24: The residual ellipticity of a model globular cluster convolved with a nearly circular ($\epsilon = 0.01$) Gaussian function (crosses). The boxes represent the ellipticity calculated at specified threshold intensities, I , when smearing-subtracted moments were employed. The region enclosing the image was constant in size.

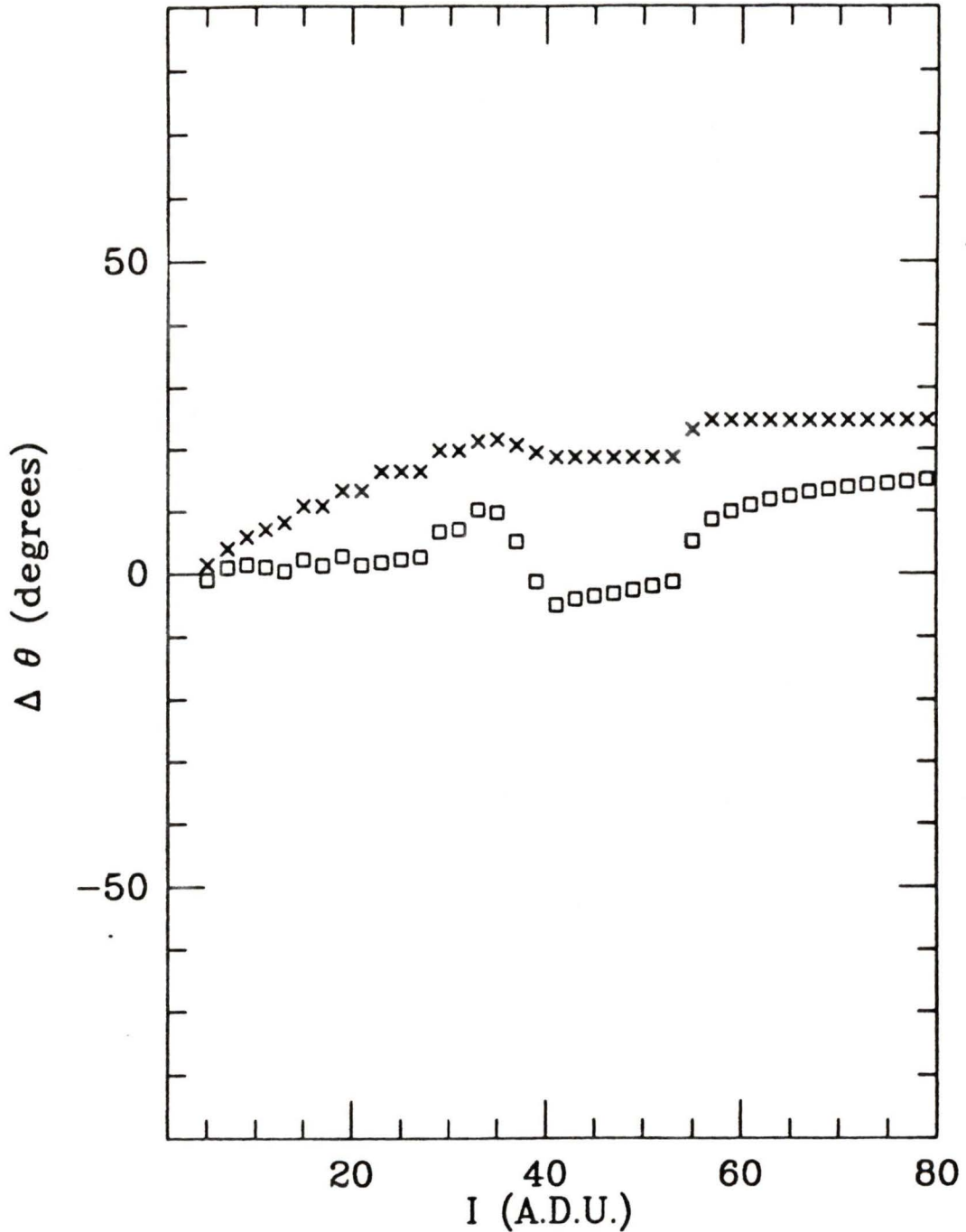


Figure 25: The residual orientation of the semi-major axis of a model globular cluster convolved with an elliptical ($\epsilon = 0.01$) Gaussian function (crosses). The boxes represent the orientation calculated at specified threshold intensities, I , when smearing-subtracted moments were employed. The region enclosing the image was constant in size.

tend to be intrinsically rounder at their centers; hence the measured ellipticity will tend to be lower than that measured with an isophotal technique. Therefore, the image attributes computed by this moment method for the M31 globular clusters of this project can only place bounds upon the actual shape and orientation of the globular. A further limitation on the use of this moment method arises from the fact that DAOPHOT computes the point-spread function of a frame by fitting a Gaussian function to the stellar image in each of the CCD's axial directions, (see Appendix A) hence the true orientation of the convolved seeing profile is not computed. Thus, the position angle of the point-spread function of the CFHT data which, unlike the model data may be off-axis, cannot be accurately determined and hence the cluster orientation measured by the moment method cannot be designated an upper or lower bound to the true globular orientation.

In summary, image shape and orientation are computed within $\pm 1\%$ and $\pm 5^\circ$ respectively in the absence of noise and seeing if the region enclosing the image contains in excess of 50 pixels. The maximum region size may be constrained by nearby stellar images. The addition of a Gaussian noise spectrum of amplitude 4.2 A.D.U. to the base frame has minimal effect upon the computation of image attributes (see Figures 18 and 19). However, convolving a realistic seeing profile with the base frame *does* affect the computation of the shape and orientation of an image but this bias can be somewhat alleviated by using Equation 31 to subtract the image-smearing due to seeing prior to the calculation of cluster attributes. However, as Figures 22 through 25 demonstrate, the image attributes continue to be biased if the convolved seeing function is elliptical. Therefore, the shape and orientation computed by this moment method for the M31 globular cluster data in this project can only place bounds upon the actual cluster attributes. Furthermore, since the position angle of the point-spread function is computed along the axes

of the CCD and not necessarily along the axes of the seeing profile, the globular orientation, measured by the moment method, cannot be designated an upper or lower bound to the true cluster orientation for the CFHT data of this project. Hence, this moment method is only capable of determining a limiting value of ellipticity for the M31 globular clusters listed in Table 1.

3.3 Comparing the Methods

A comparison of the determination of image shape and orientation using both the isophotal and moment methods previously described is demonstrated in Figures 26 and 27 where I is the isophotal or threshold intensity specified for the respective image processing software packages. In each figure the cross represents the isophotal method and the image whose attributes are illustrated is the artificial base frame created using R2D2 to simulate the data of this project as described in Section 3.1.2. These figures indicate that, *in principle*, the isophotal and moment methods are equivalent. However, the moment method employs intensity-weighted moments in the calculation of image attributes hence the image attributes computed in VISTA will be greatly biased by the convolved seeing function. The moment method is therefore only capable of placing bounds upon the actual image attributes. Thus, the estimated ellipticity and orientation of the M31 globular clusters of this project, quoted in Chapter 5, are those values calculated by the isophotal method even though the isophotal and moment methods are, *in principle*, consistent in their measures of ellipticity.

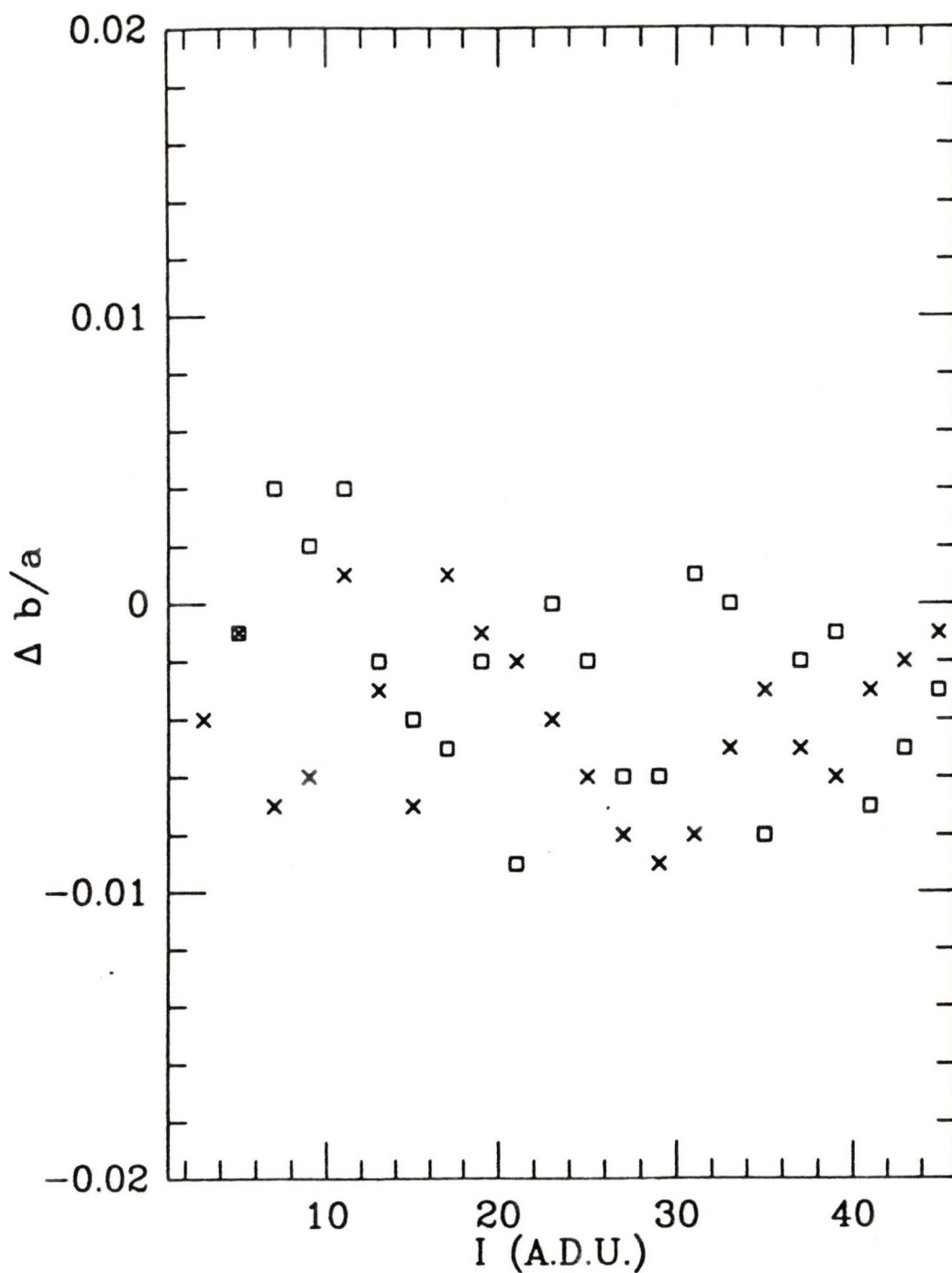


Figure 26: The axial ratio of model globular cluster data determined at various intensity levels, I , using the isophotal (crosses) and moment (boxes) methods described in the text.

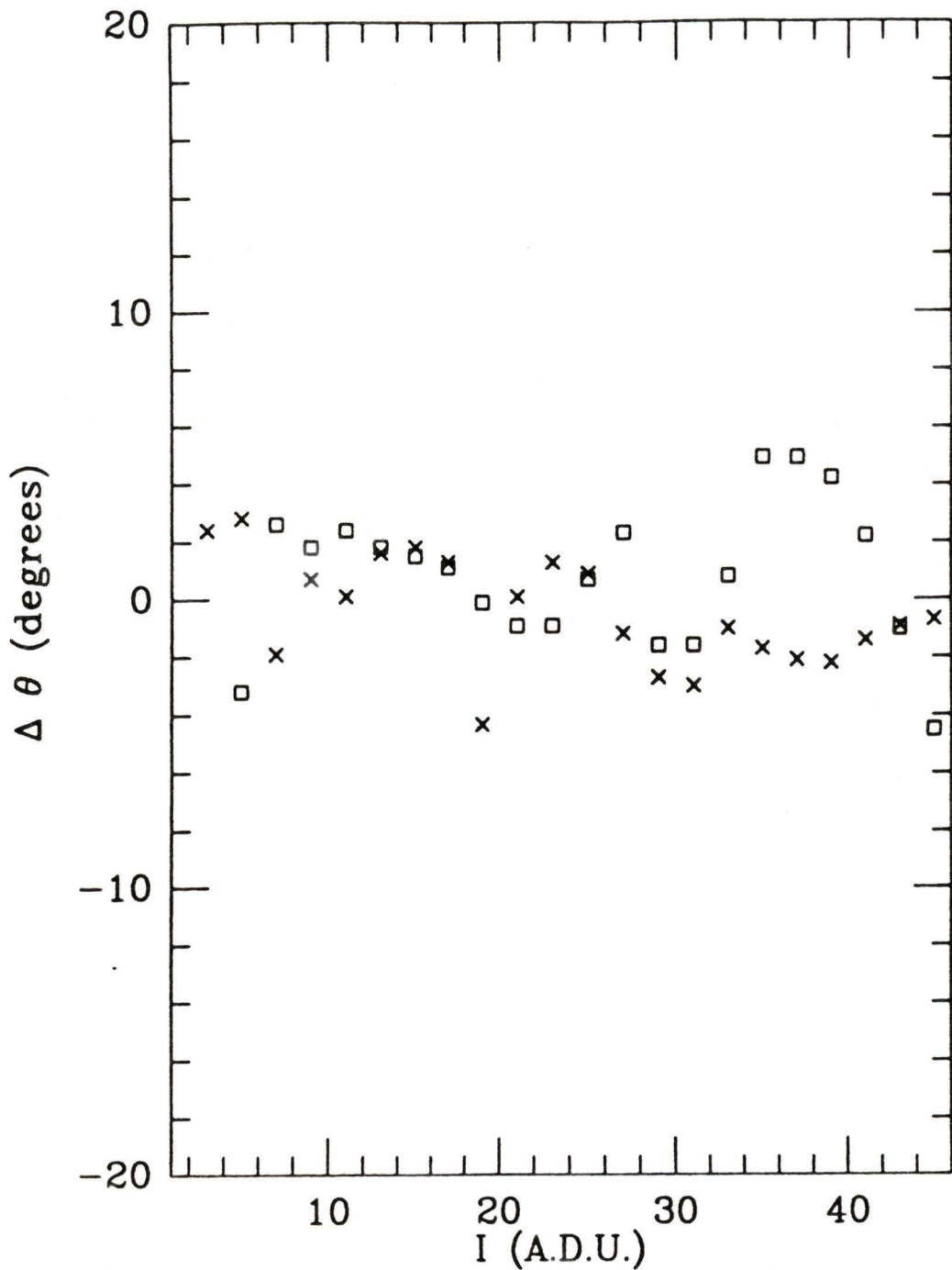


Figure 27: The orientation of the semi-major axis of model globular cluster data determined at various intensity levels, I , using the isophotal (crosses) and moment (boxes) methods described in the text.

Chapter 4

Image Analysis

The CFHT CCD observations of M31 globular clusters were bias subtracted and flat fielded by C. J. Pritchett at the University of Victoria using his data reduction software package R2D2. The median background intensity was determined for each frame using an iterative outlier rejection technique incorporated in R2D2. When a differential background light contribution was observed in the globular cluster data, a tilted plane was fitted to the data and the median background intensity was then determined using the iterative outlier rejection technique. A brightness gradient was observed only for the frame containing G185. Each frame was reduced to a common zero level by subtraction of its background intensity. The brightest unsaturated stellar images on each frame were then magnified four times using the bicubic spline interpolation subroutines of Press *et al.* (1986).

Isophotes for the resultant stellar image and its corresponding globular were linearly interpolated, using R2D2, at increments of 2 A.D.U. in the wings and 10 – 100 A.D.U. near the core. An ellipse was fitted to each isophote using a least-squares outlier rejection technique and the attributes of the ellipse were calculated as described in Section 3.1. Each contoured image was visually inspected to ensure

the outermost isophotes were not contaminated by extraneous images. Figures 28 through 48 illustrate the intensity profile and variation of isophotal axial ratio with effective radius for each M31 globular cluster observed in this project and a stellar image in each field. The open symbol represents the stellar image in each figure. The error bars are calculated from the residuals of the fit of an ellipse to the isophote and are not related to the CFHT observations (see Section 3.1.1).

A limiting ellipticity was computed for each globular at the outermost isophote using the moment method described in Section 3.2 (*i.e.*, by selecting the sky or threshold level in the moment method to be the intensity level of the outermost contour, a limiting ellipticity was computed using all the pixels contained within this isophote). Care was exercised to ensure the isophote was completely contained within the region specified for use in the moment method.

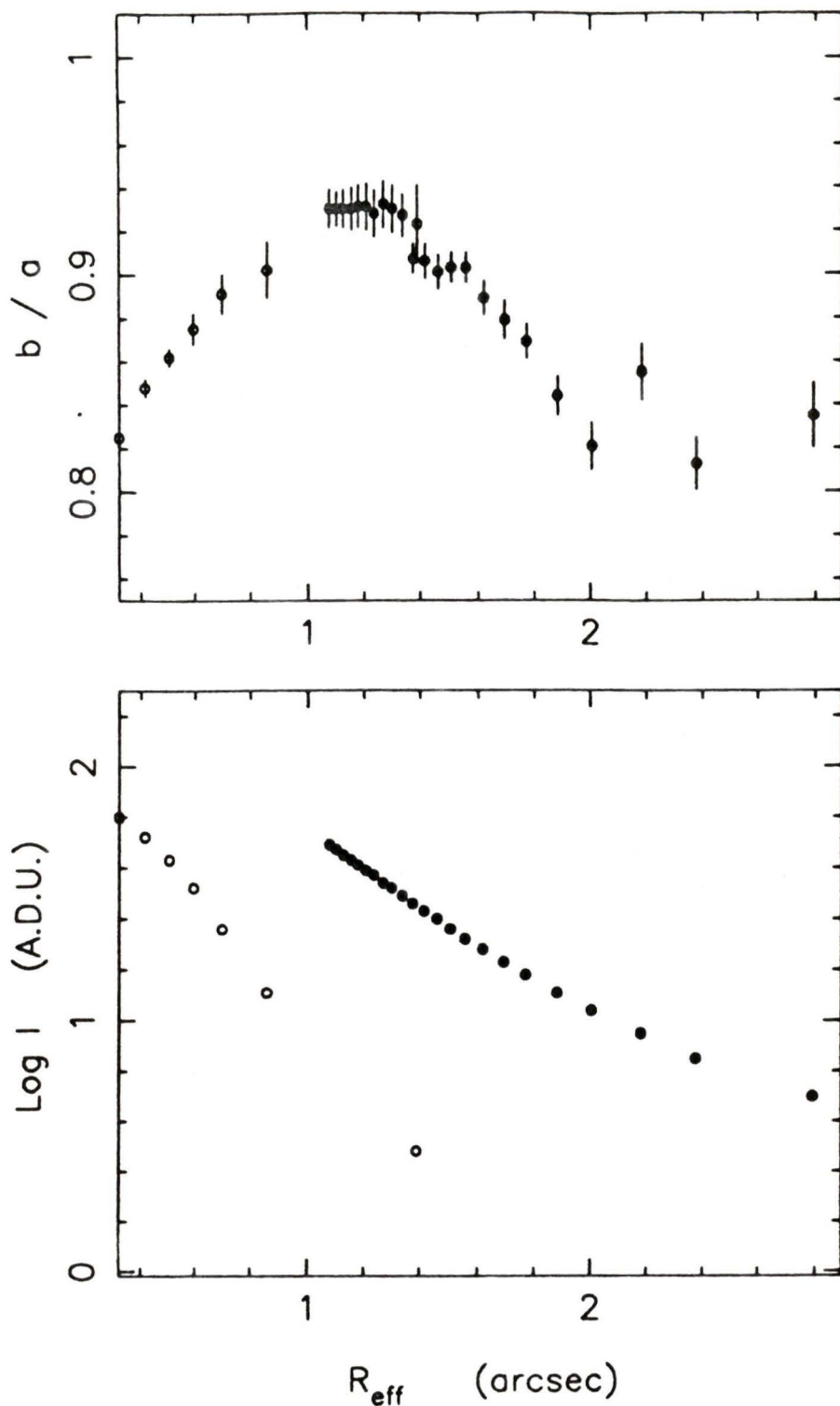


Figure 28: The variation of isophotal axial ratio with effective radius and the intensity profile of G1 (filled symbol) and a field star (open symbol). The observations were made through a V filter and the exposure time was 60s. The isophotal increment is 2 A.D.U. in the wings and 10 - 100 A.D.U. near the core.

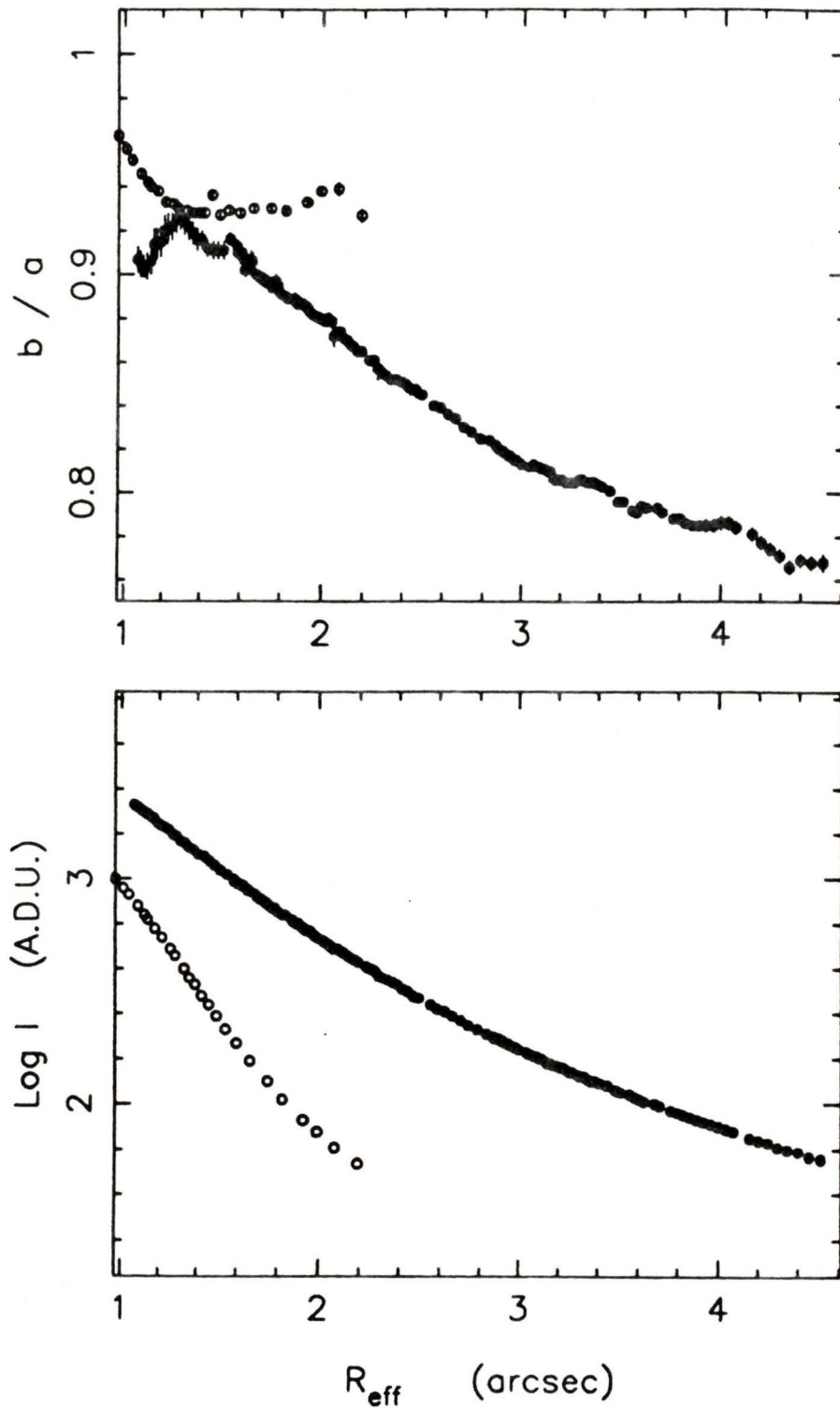


Figure 29: The variation of isophotal axial ratio with effective radius and the intensity profile of G1 (filled symbol) and a field star (open symbol). The observations were made through a B filter and the exposure time was 300s. The isophotal increment is 2 A.D.U. in the wings and 10 - 100 A.D.U. near the core.

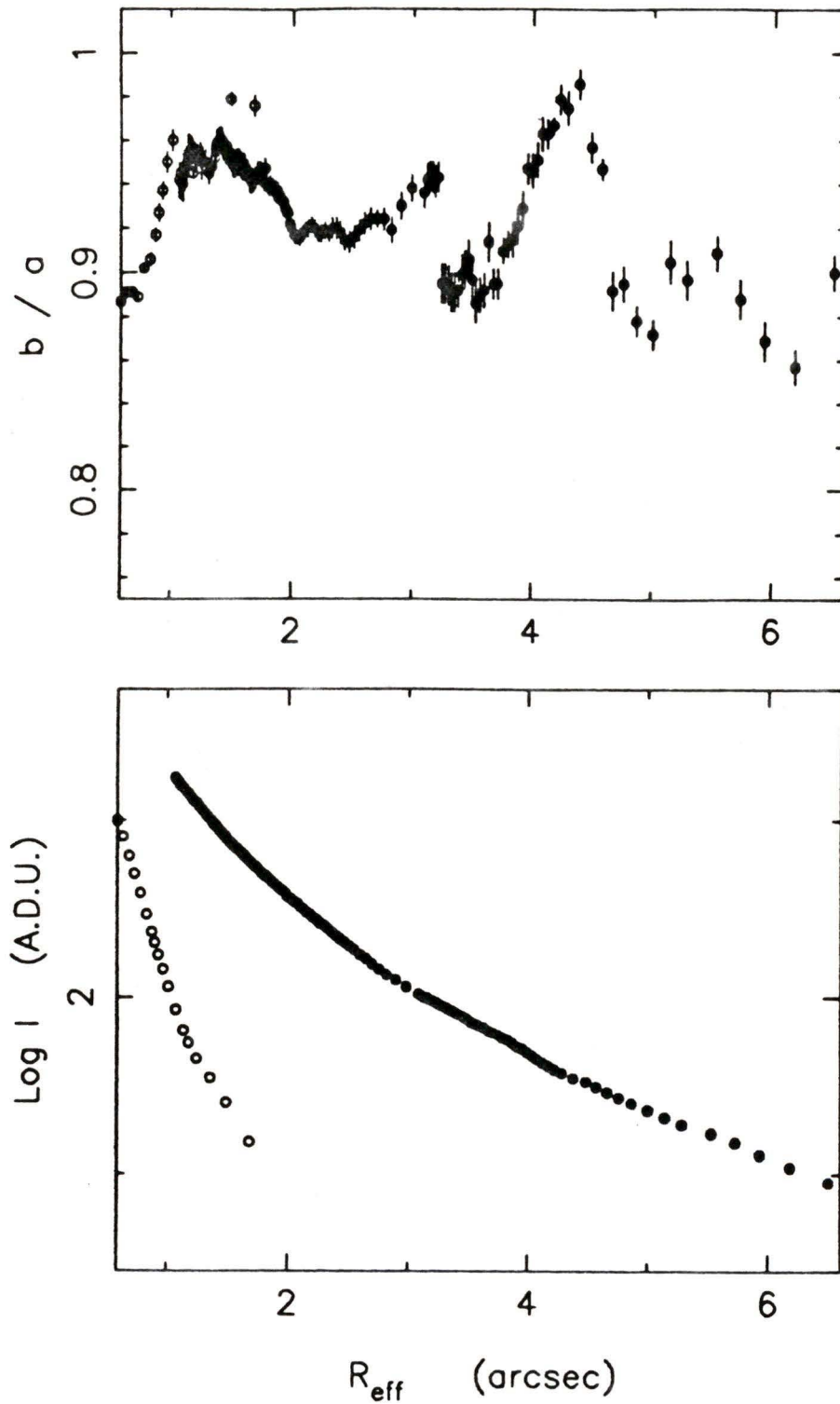


Figure 30: The variation of isophotal axial ratio with effective radius and the intensity profile of G64 (filled symbol) and a field star (open symbol). The observations were made through a V filter and the exposure time was 400s. The isophotal increment is 2 A.D.U. in the wings and 10 - 100 A.D.U. near the core.

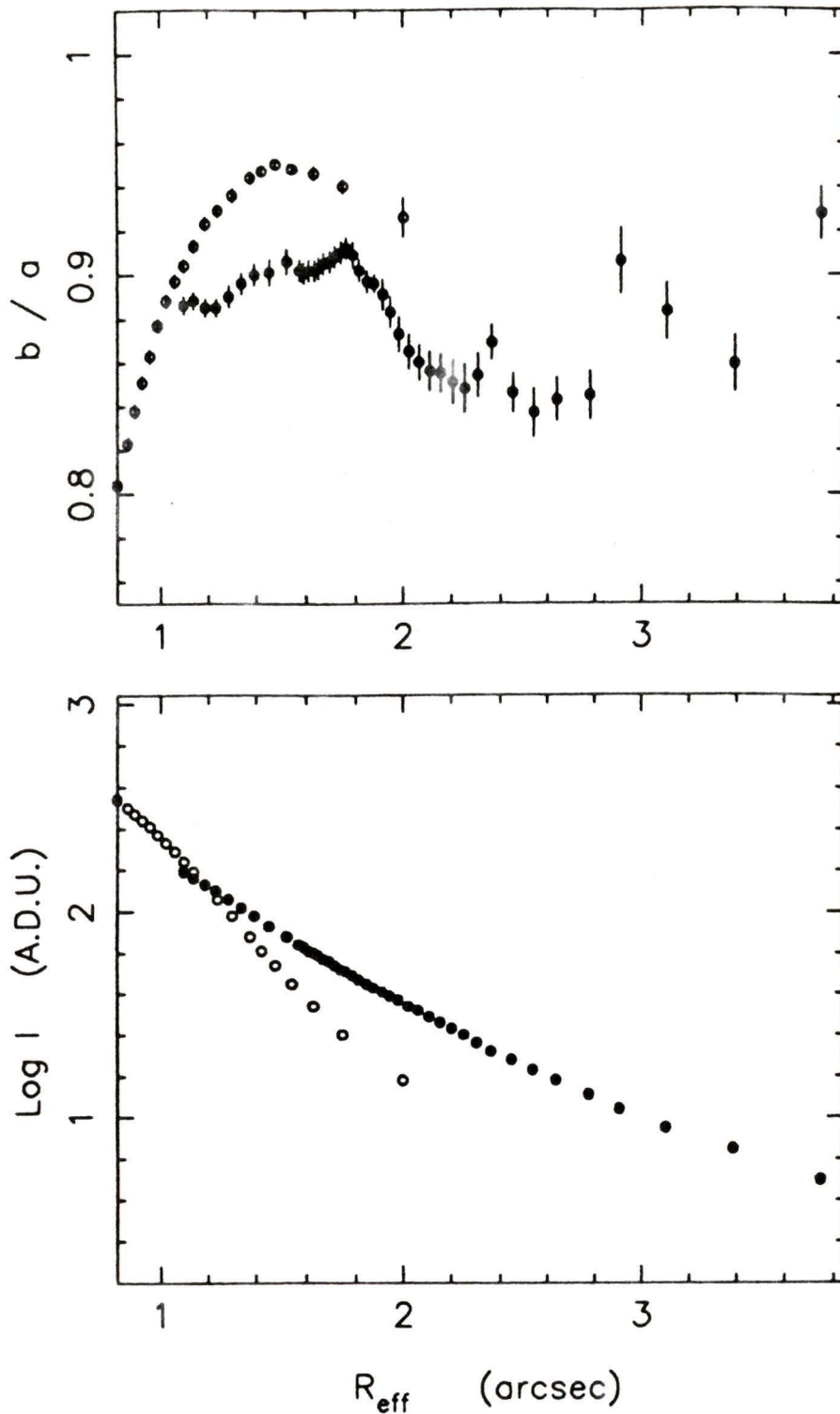


Figure 31: The variation of isophotal axial ratio with effective radius and the intensity profile of G72 (filled symbol) and a field star (open symbol). The observations were made through a B filter and the exposure time was 500s. The isophotal increment is 2 A.D.U. in the wings and 10 - 100 A.D.U. near the core.

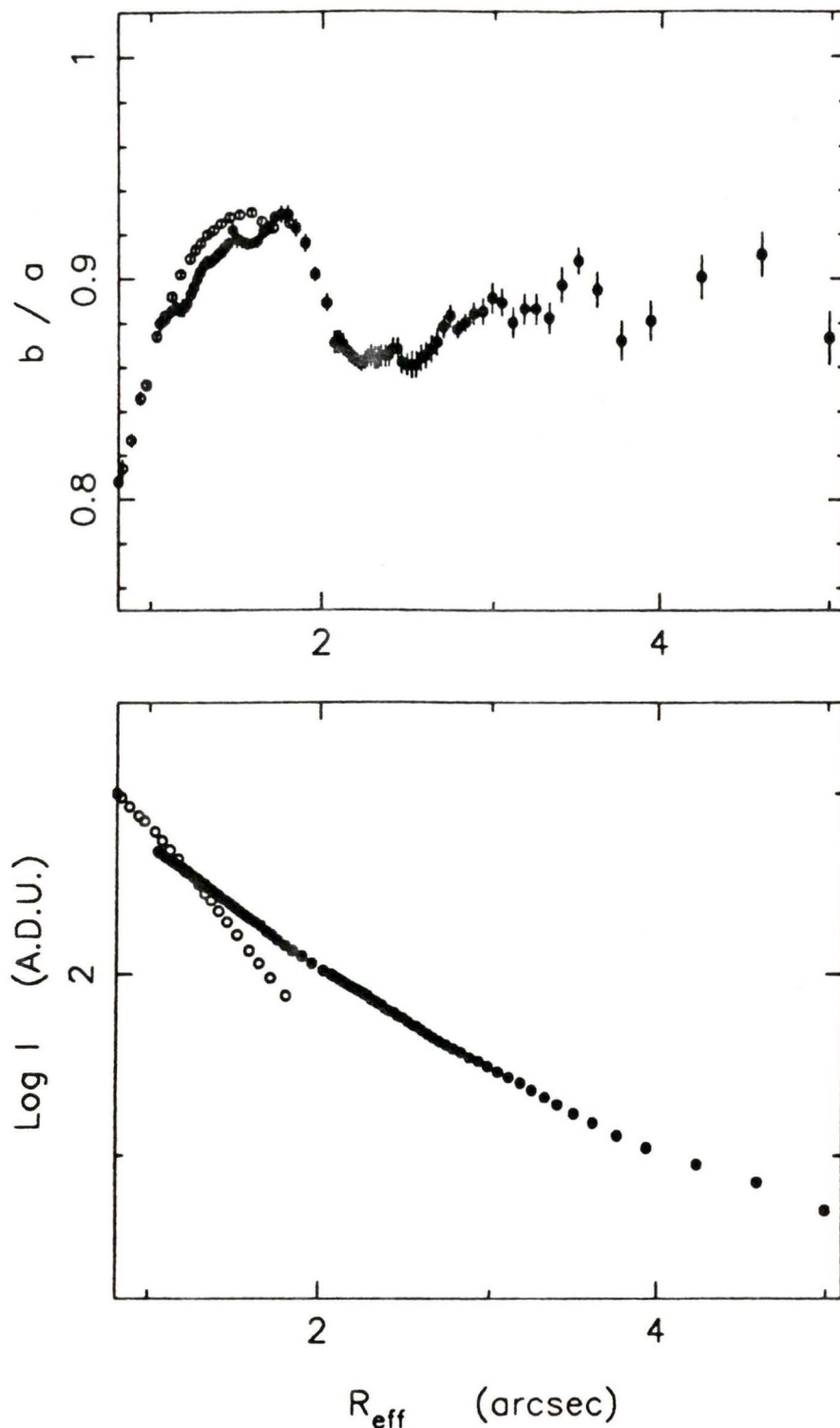


Figure 32: The variation of isophotal axial ratio with effective radius and the intensity profile of G72 (filled symbol) and a field star (open symbol). The observations were made through a B filter and the exposure time was 1000s. The isophotal increment is 2 A.D.U. in the wings and 10 - 100 A.D.U. near the core.

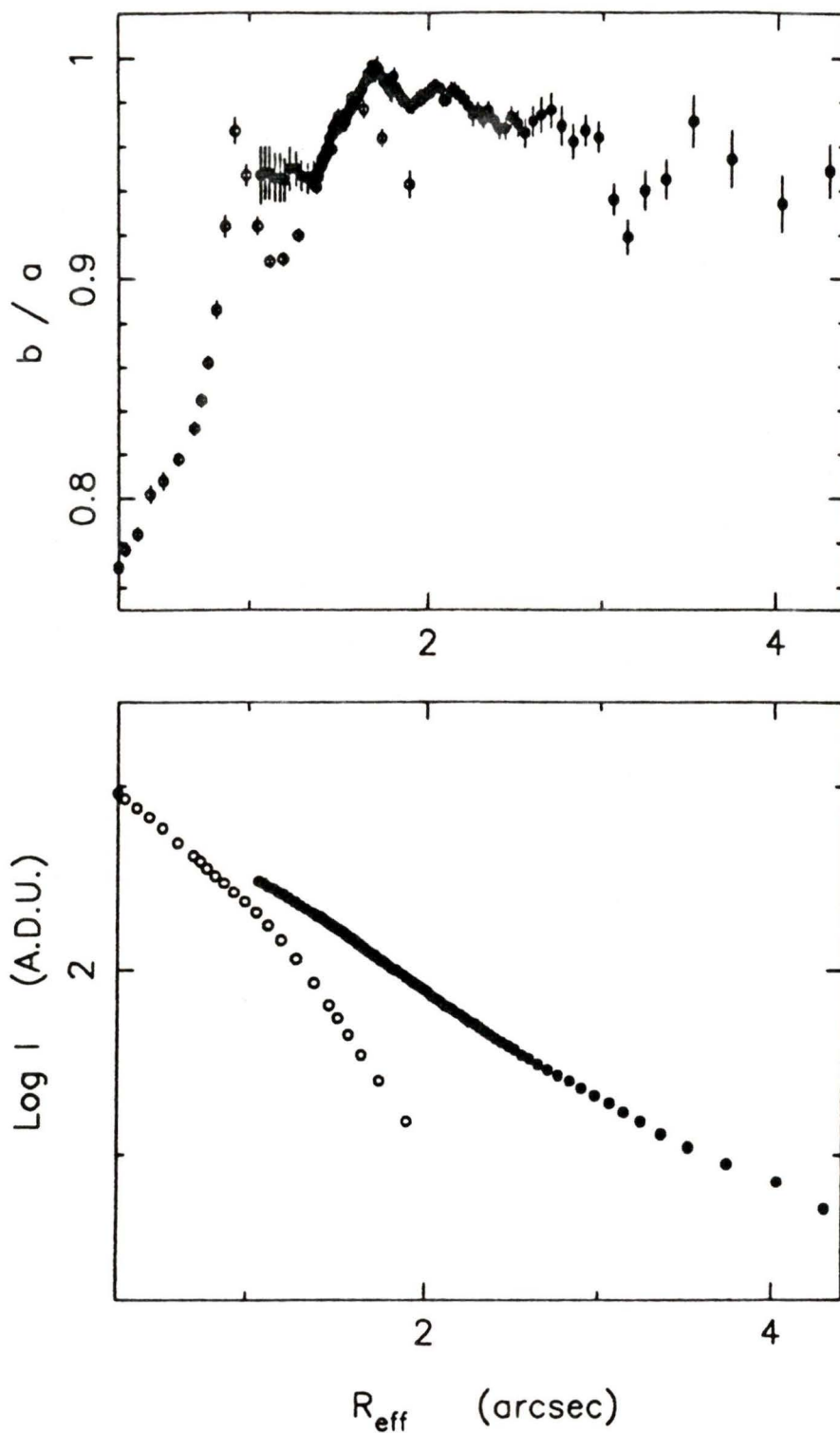


Figure 33: The variation of isophotal axial ratio with effective radius and the intensity profile of G73 (filled symbol) and a field star (open symbol). The observations were made through a B filter and the exposure time was 500s. The isophotal increment is 2 A.D.U. in the wings and 10 - 100 A.D.U. near the core.

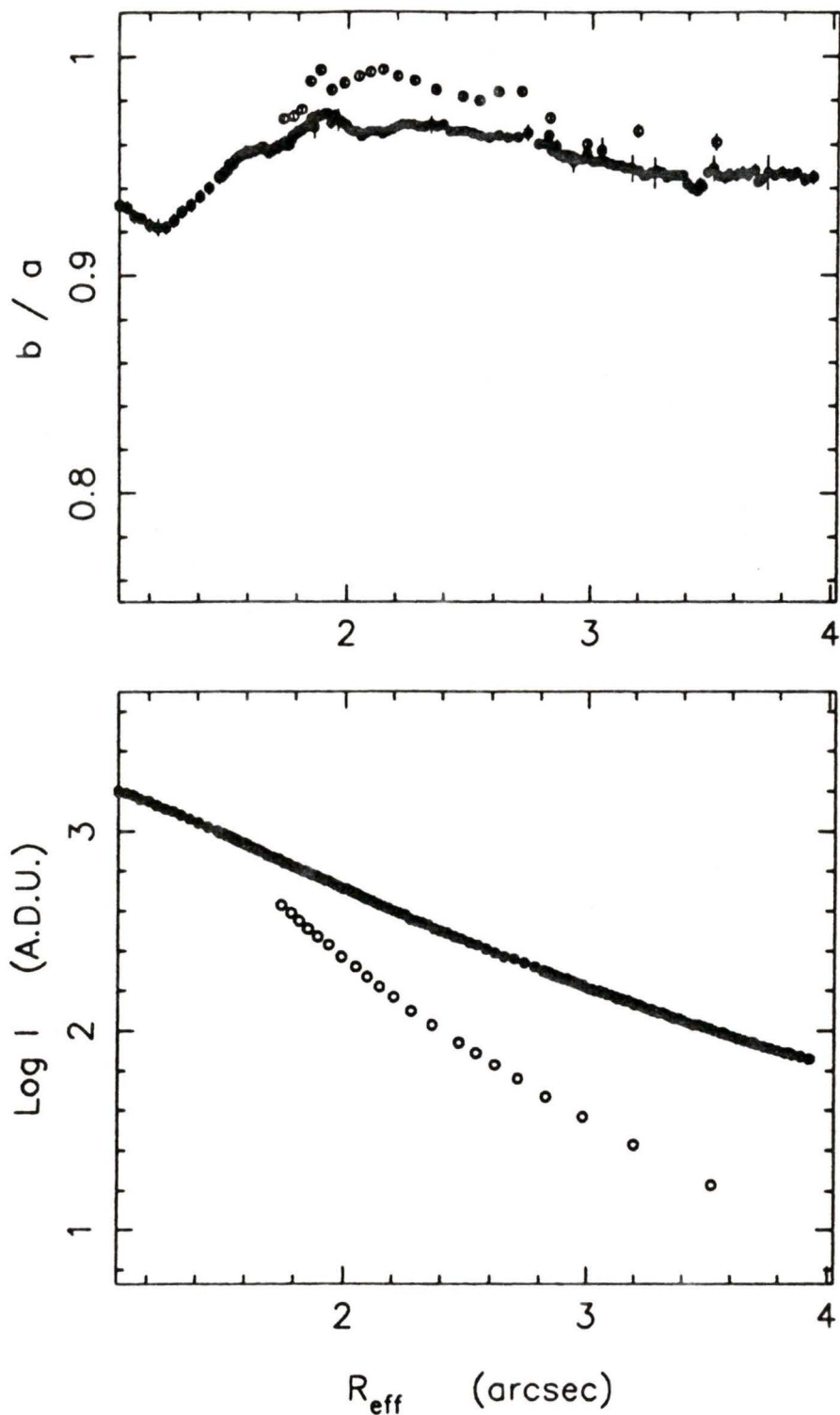


Figure 34: The variation of isophotal axial ratio with effective radius and the intensity profile of G76 (filled symbol) and a field star (open symbol). The observations were made through a B filter and the exposure time was 400s. The isophotal increment is 2 A.D.U. in the wings and 10 - 100 A.D.U. near the core.

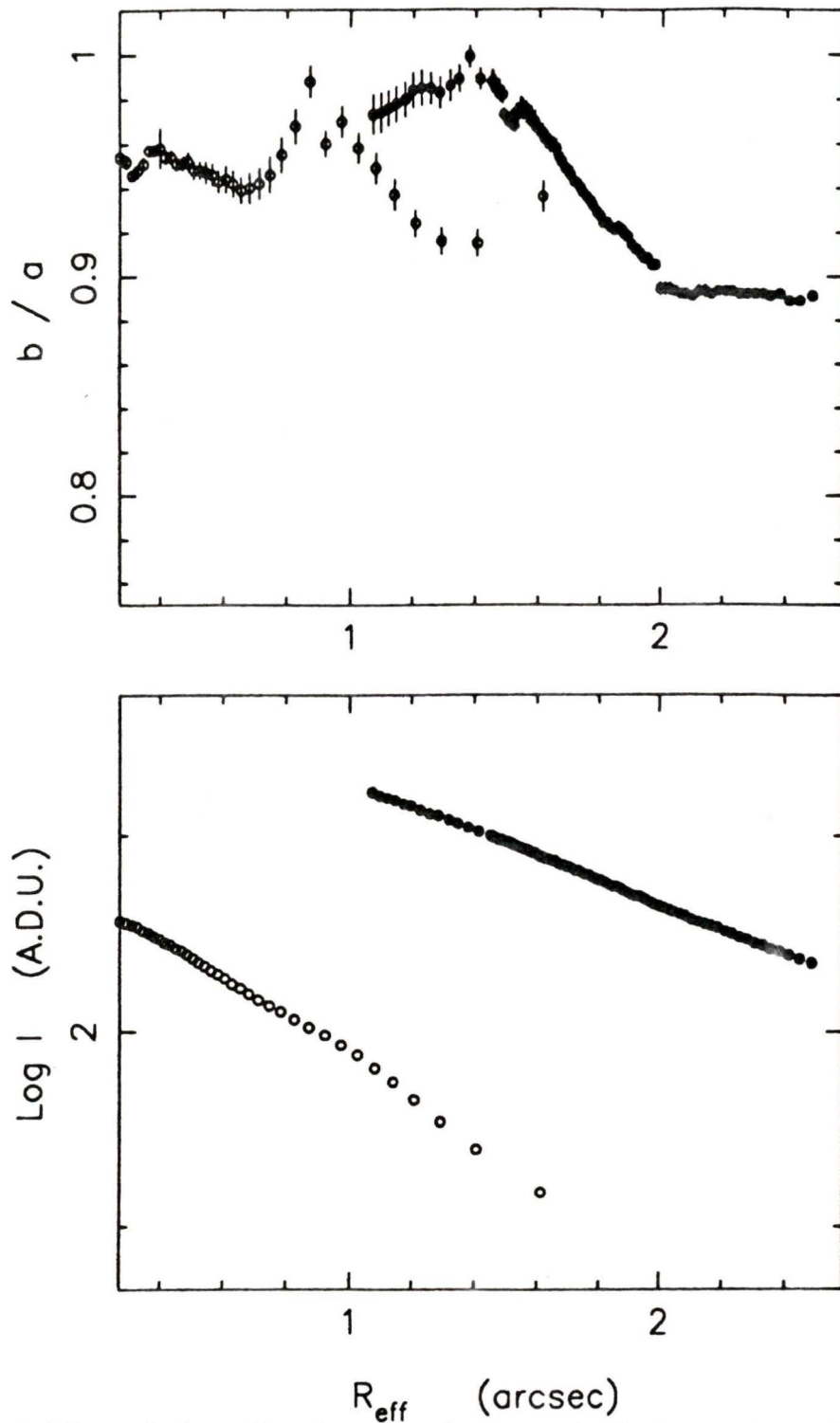


Figure 35: The variation of isophotal axial ratio with effective radius and the intensity profile of G78 (filled symbol) and a field star (open symbol). The observations were made through a B filter and the exposure time was 400s. The isophotal increment is 2 A.D.U. in the wings and 10 - 100 A.D.U. near the core.

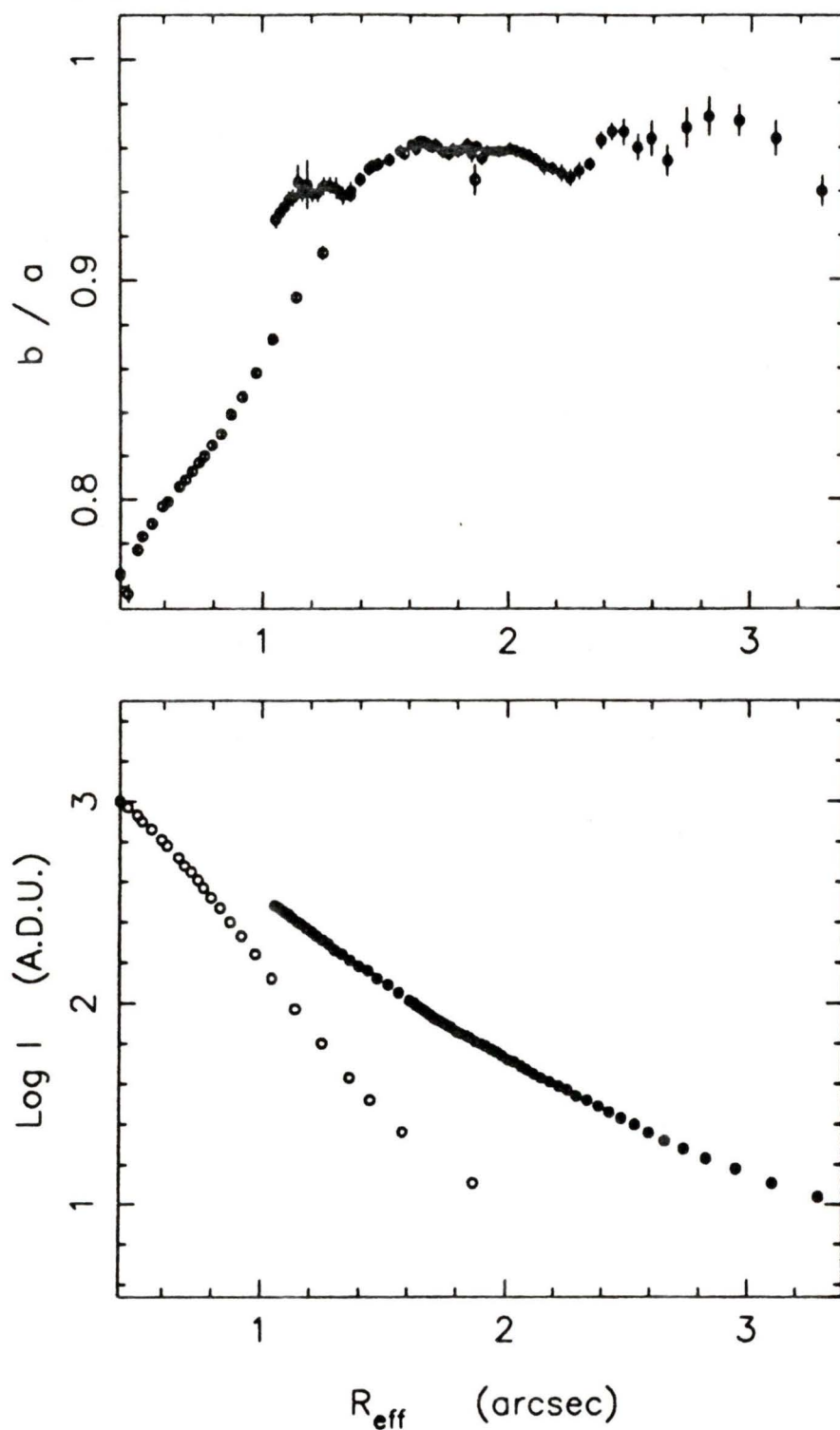


Figure 36: The variation of isophotal axial ratio with effective radius and the intensity profile of G119 (filled symbol) and a field star (open symbol). The observations were made through a V filter and the exposure time was 120s. The isophotal increment is 2 A.D.U. in the wings and 10 - 100 A.D.U. near the core.

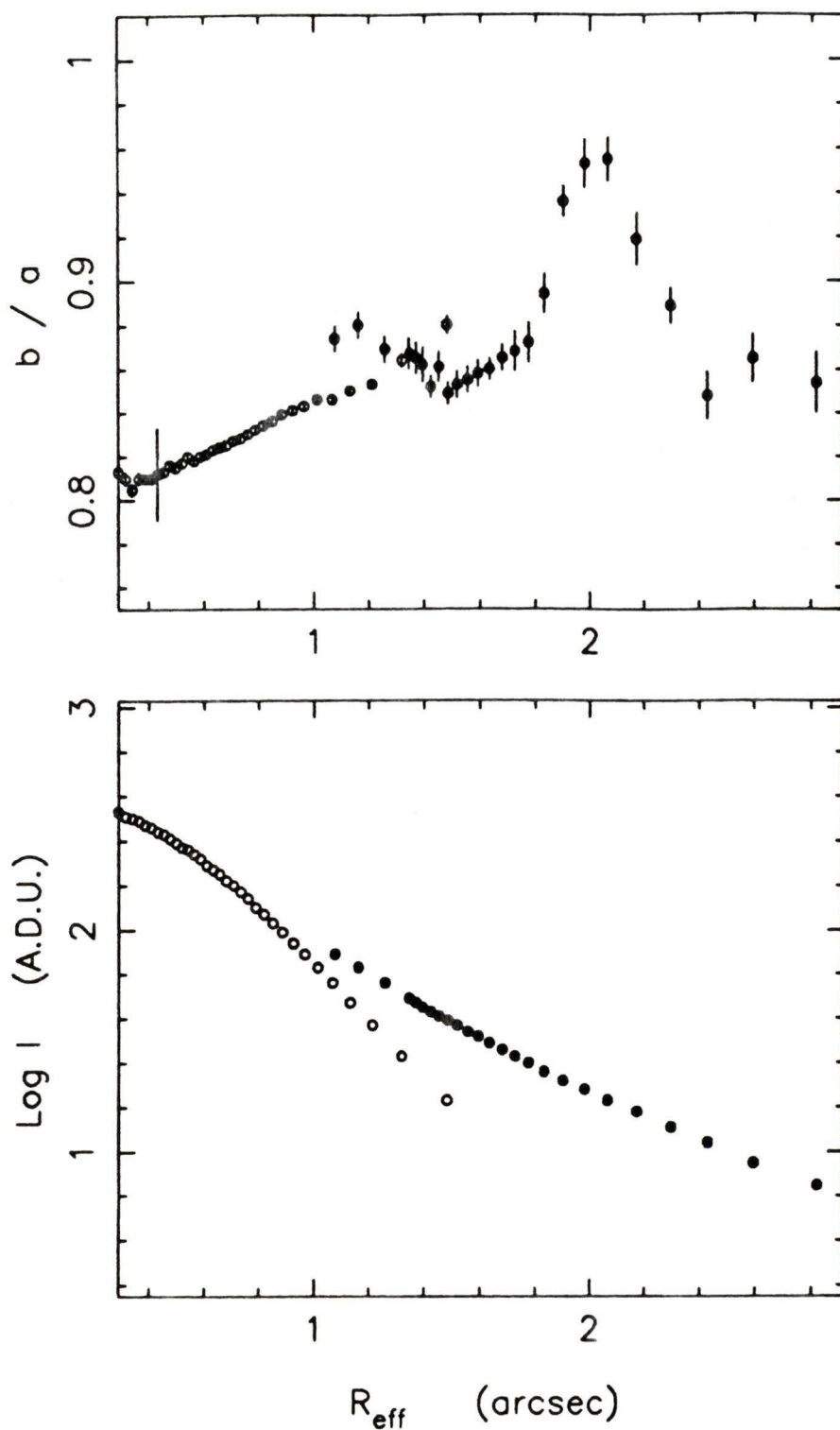


Figure 37: The variation of isophotal axial ratio with effective radius and the intensity profile of G148 (filled symbol) and a field star (open symbol). The observations were made through a V filter and the exposure time was 120s. The isophotal increment is 2 A.D.U. in the wings and 10 - 100 A.D.U. near the core.

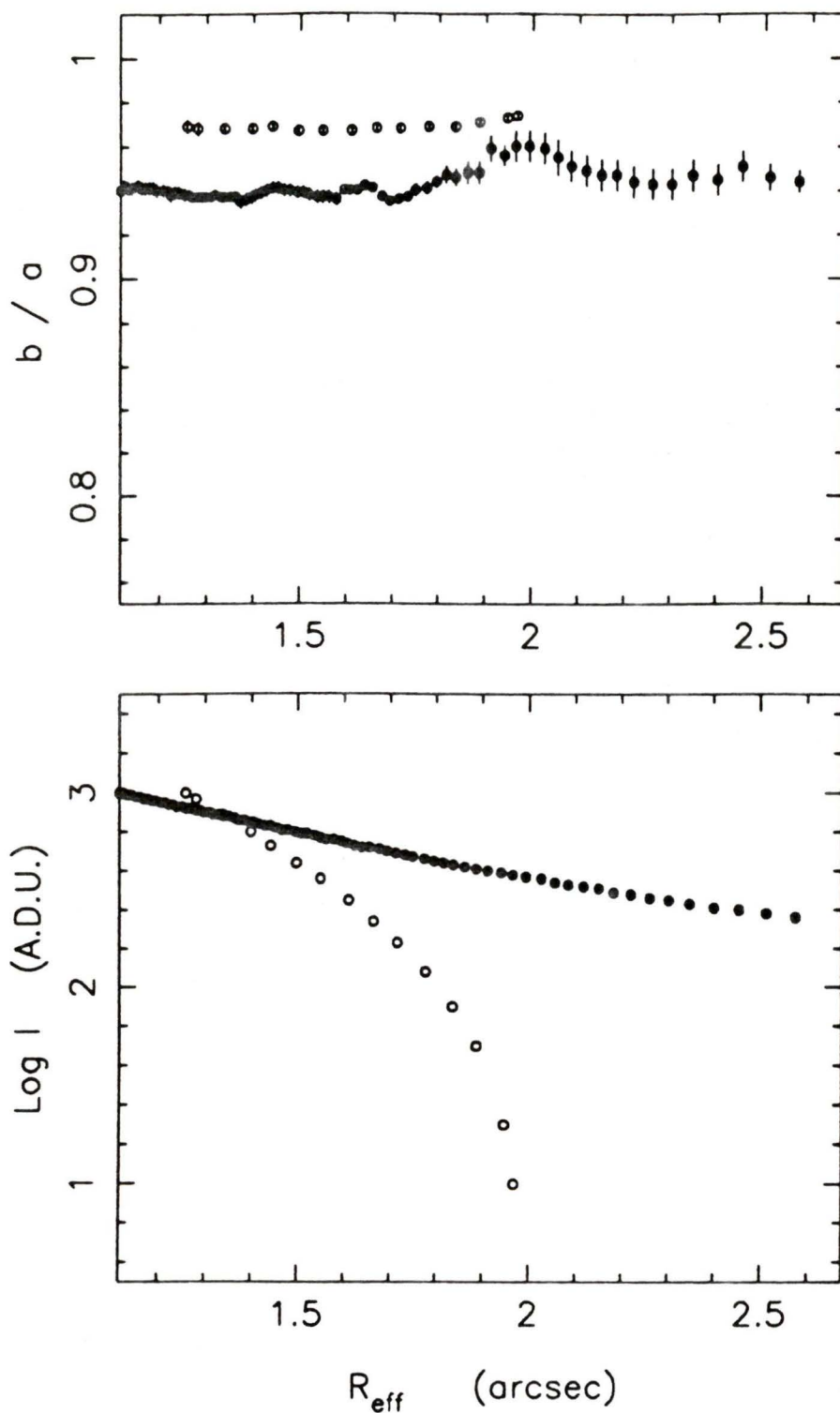


Figure 38: The variation of isophotal axial ratio with effective radius and the intensity profile of G185 (filled symbol) and a field star (open symbol). The observations were made through a B filter and the exposure time was 400s. The isophotal increment is 2 A.D.U. in the wings and 10 - 100 A.D.U. near the core.

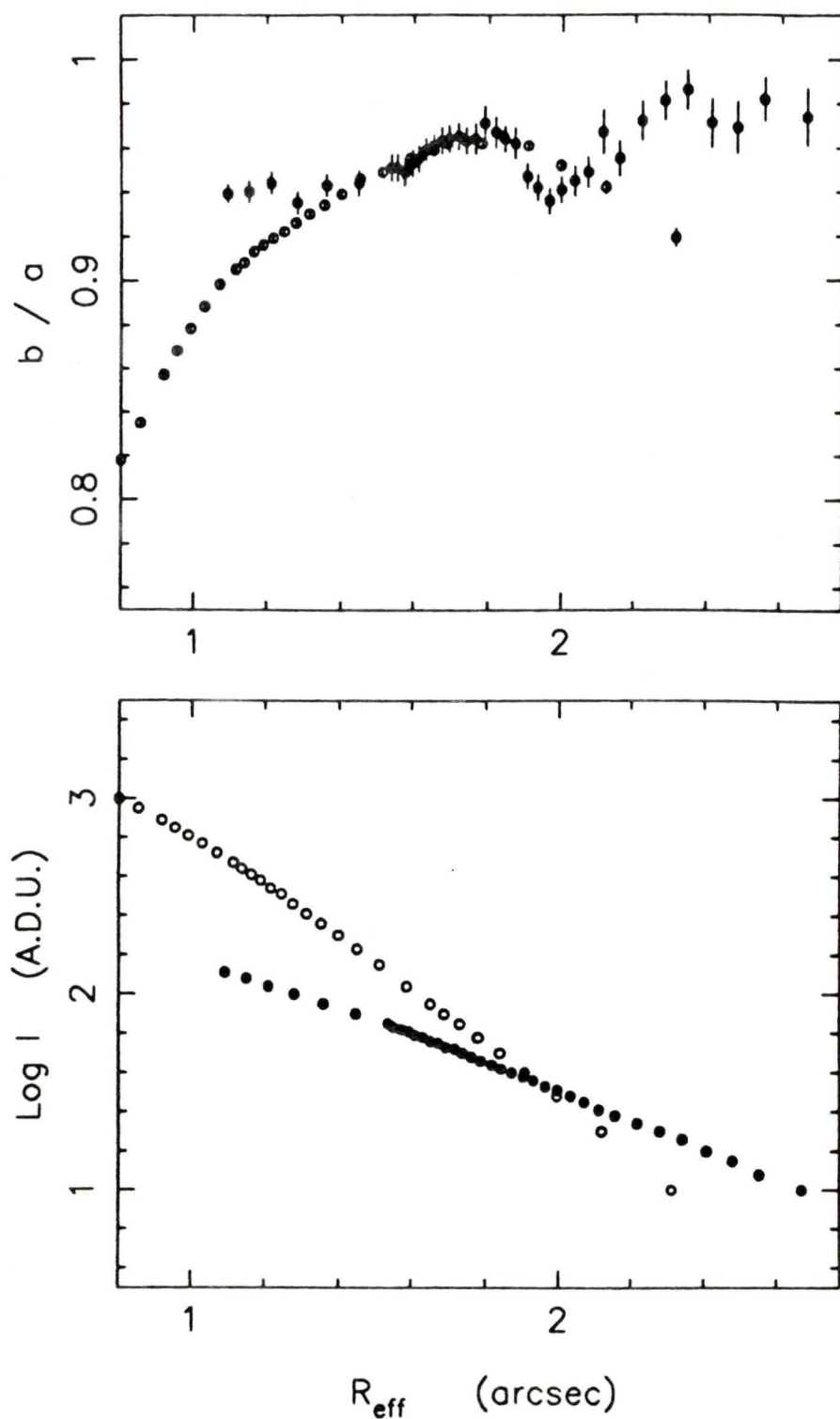


Figure 39: The variation of isophotal axial ratio with effective radius and the intensity profile of G205 (filled symbol) and a field star (open symbol). The observations were made through a B filter and the exposure time was 400s. The isophotal increment is 2 A.D.U. in the wings and 10 - 100 A.D.U. near the core.

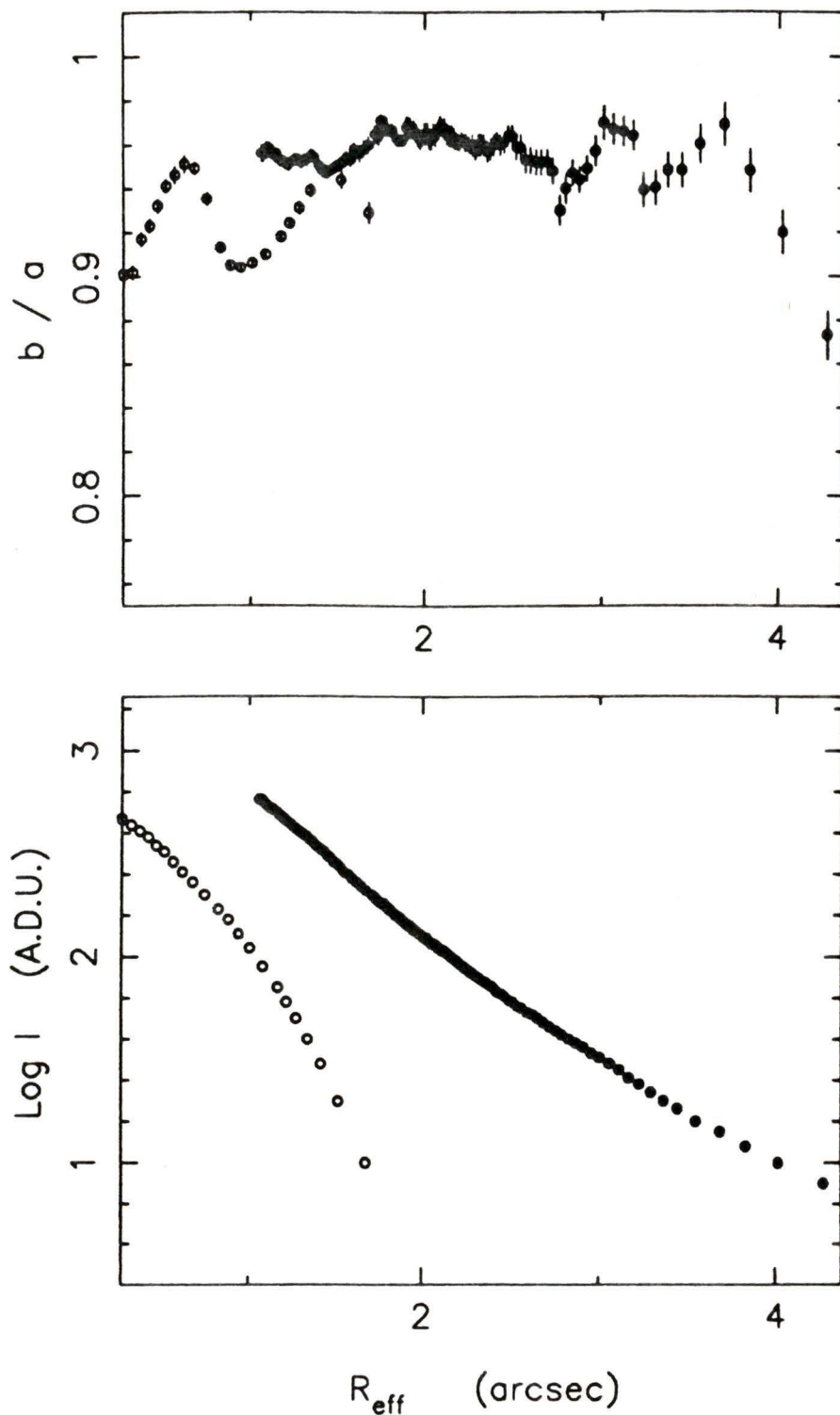


Figure 40: The variation of isophotal axial ratio with effective radius and the intensity profile of G213 (filled symbol) and a field star (open symbol). The observations were made through a B filter and the exposure time was 400s. The isophotal increment is 2 A.D.U. in the wings and 10 - 100 A.D.U. near the core.

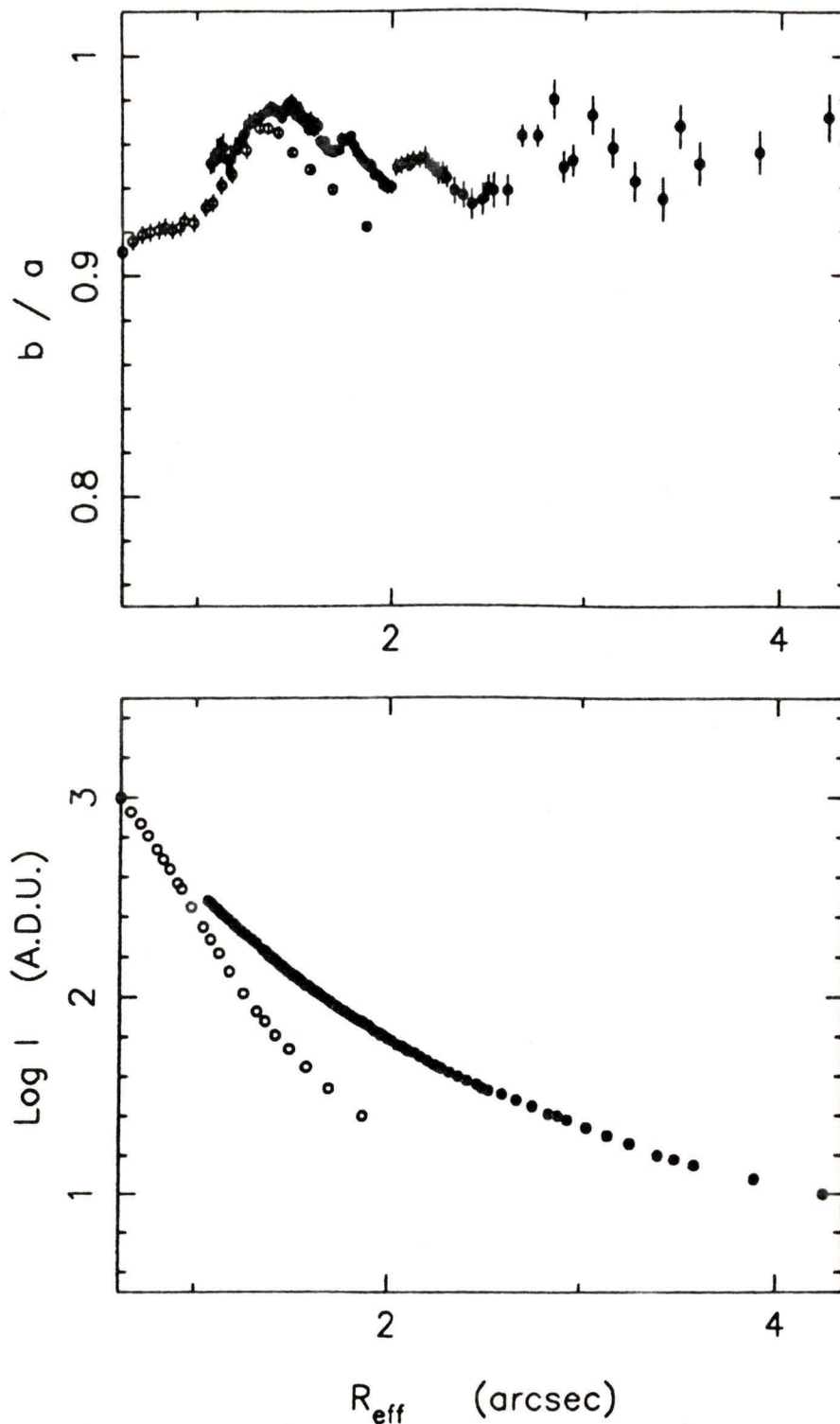


Figure 41: The variation of isophotal axial ratio with effective radius and the intensity profile of G217 (filled symbol) and a field star (open symbol). The observations were made through a V filter and the exposure time was 120s. The isophotal increment is 2 A.D.U. in the wings and 10 - 100 A.D.U. near the core.

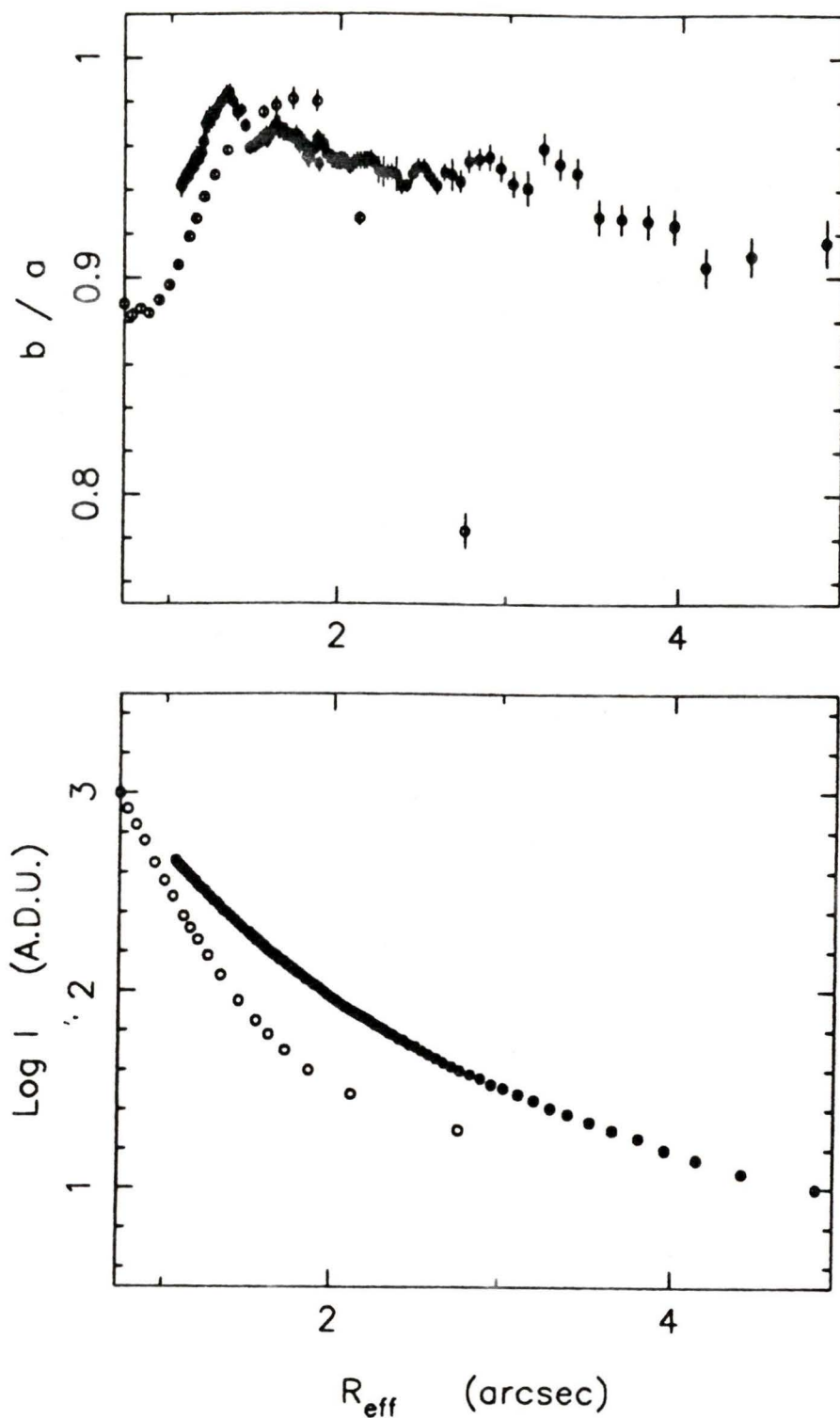


Figure 42: The variation of isophotal axial ratio with effective radius and the intensity profile of G217 (filled symbol) and a field star (open symbol). The observations were made through a V filter and the exposure time was 400s. The isophotal increment is 2 A.D.U. in the wings and 10 - 100 A.D.U. near the core.

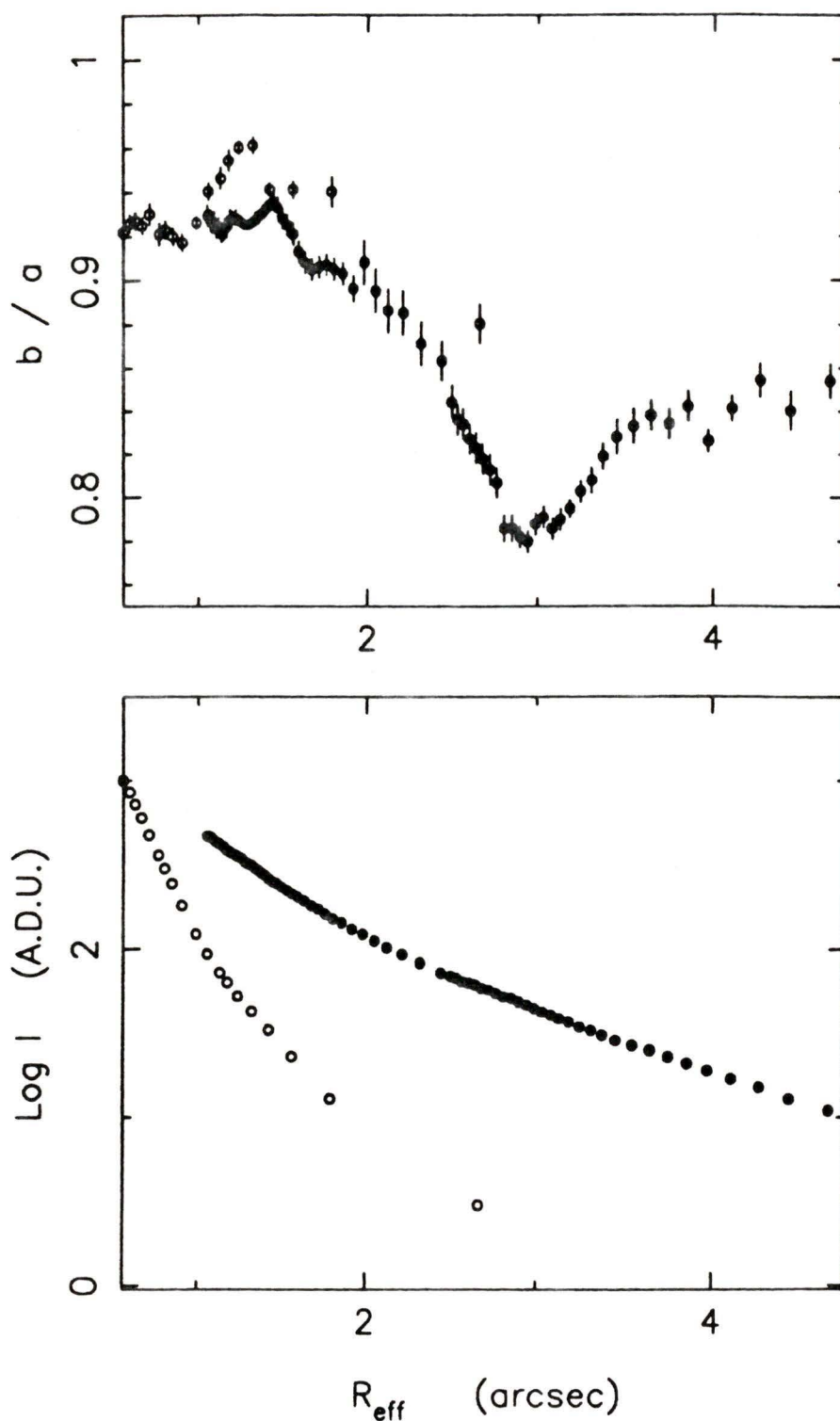


Figure 43: The variation of isophotal axial ratio with effective radius and the intensity profile of G219 (filled symbol) and a field star (open symbol). The observations were made through a V filter and the exposure time was 120s. The isophotal increment is 2 A.D.U. in the wings and 10 - 100 A.D.U. near the core.

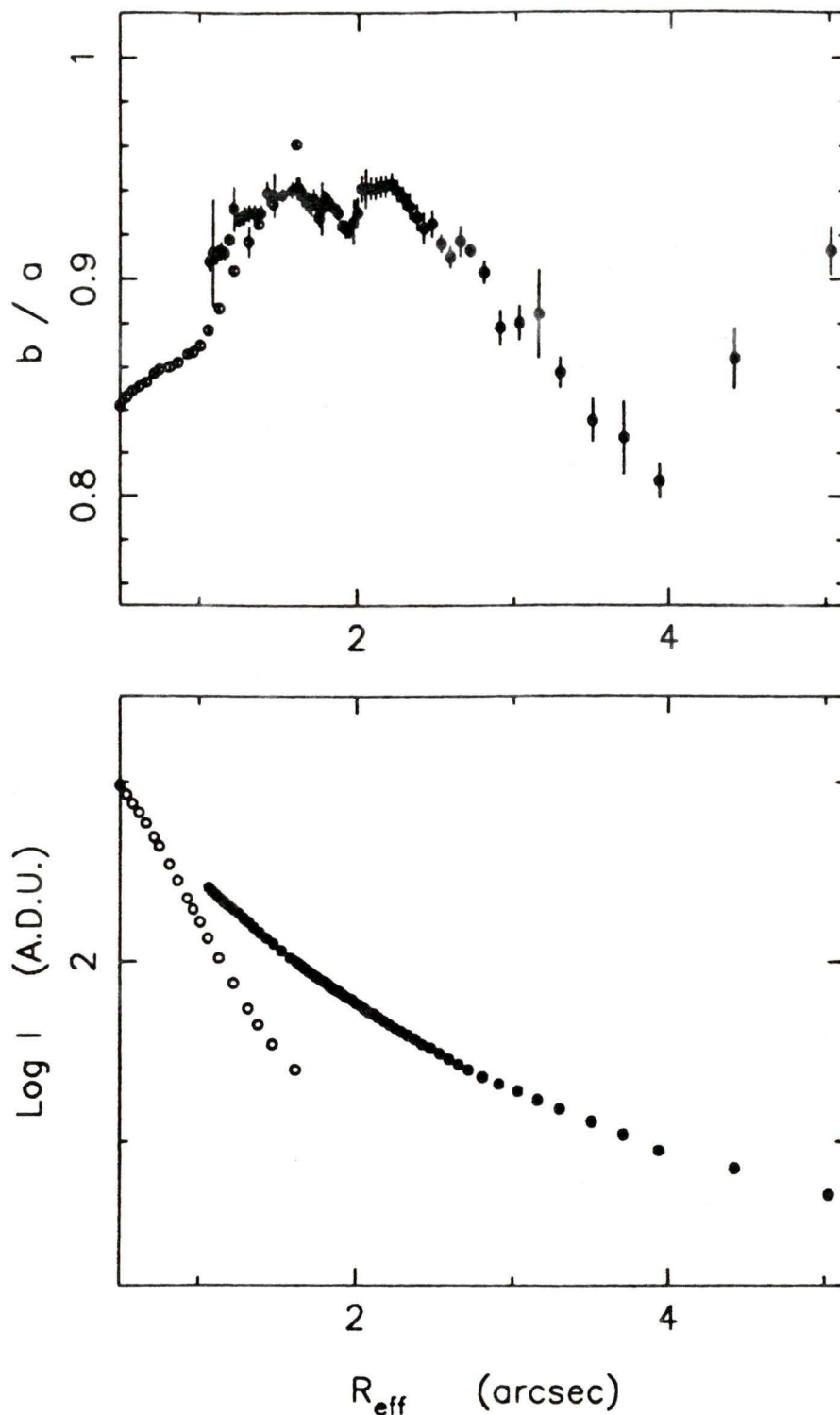


Figure 44: The variation of isophotal axial ratio with effective radius and the intensity profile of G229 (filled symbol) and a field star (open symbol). The observations were made through a V filter and the exposure time was 120s. The isophotal increment is 2 A.D.U. in the wings and 10 - 100 A.D.U. near the core.

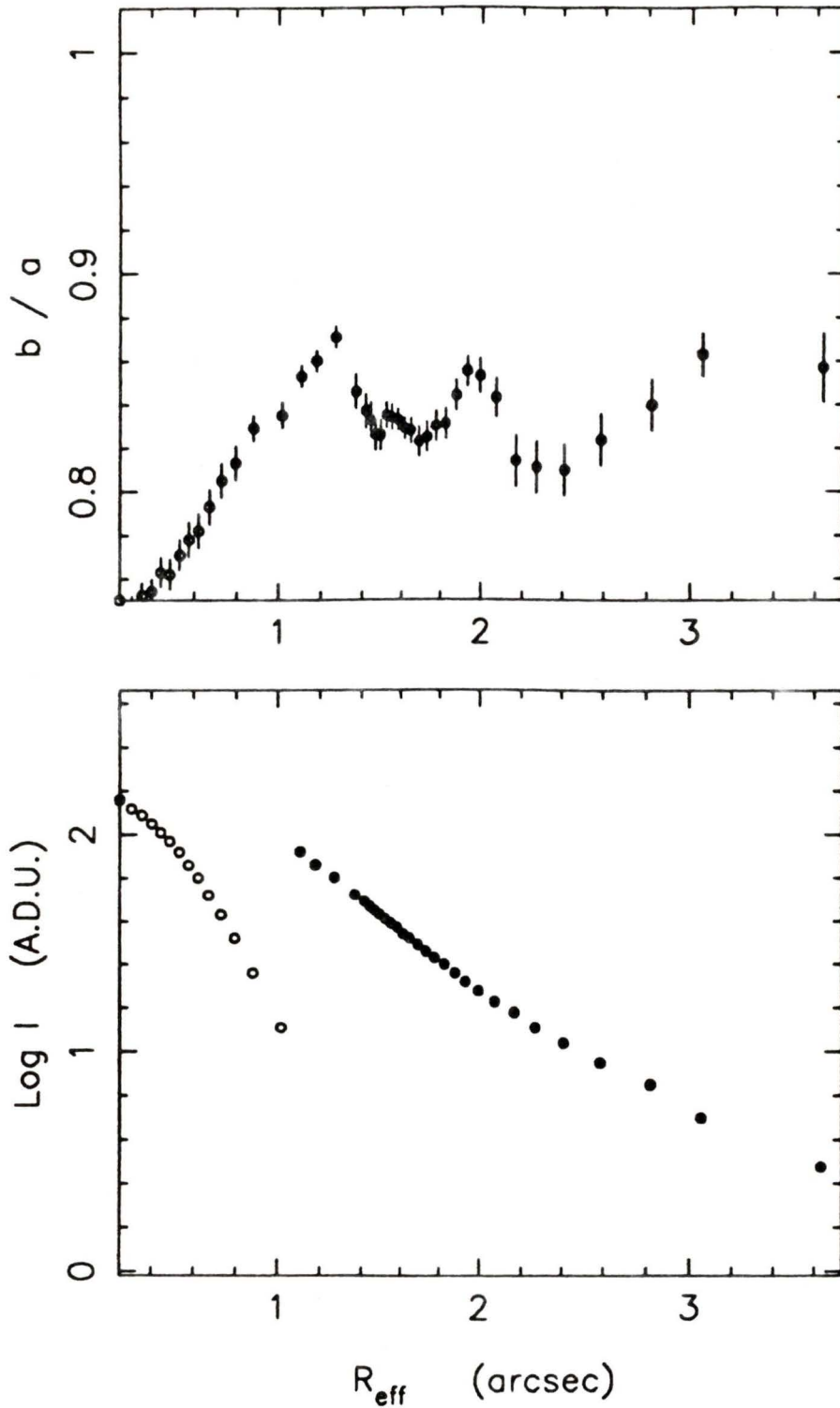


Figure 45: The variation of isophotal axial ratio with effective radius and the intensity profile of G257 (filled symbol) and a field star (open symbol). The observations were made through a V filter and the exposure time was 120s. The isophotal increment is 2 A.D.U. in the wings and 10 - 100 A.D.U. near the core.

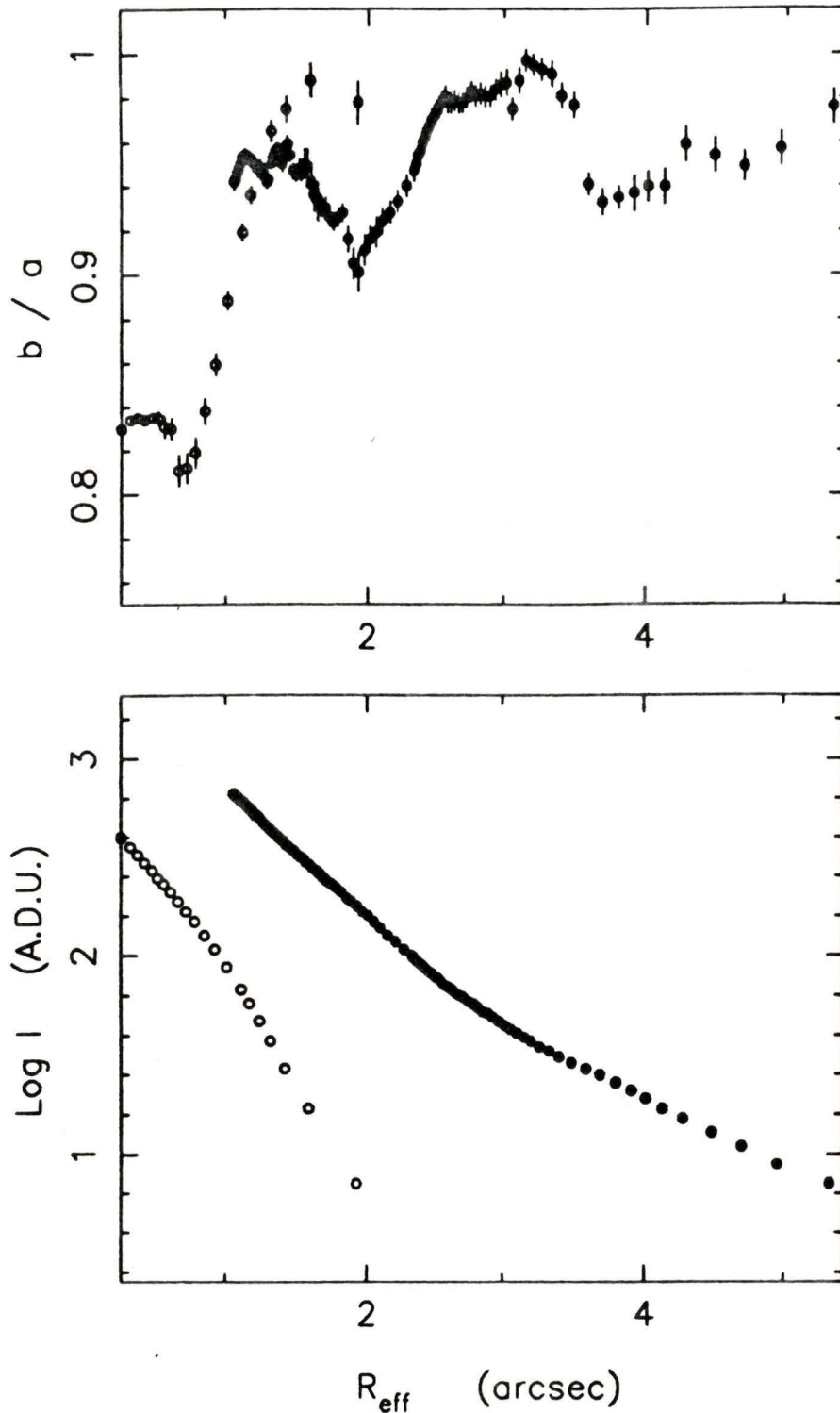


Figure 46: The variation of isophotal axial ratio with effective radius and the intensity profile of G272 (filled symbol) and a field star (open symbol). The observations were made through a B filter and the exposure time was 400s. The isophotal increment is 2 A.D.U. in the wings and 10 - 100 A.D.U. near the core.

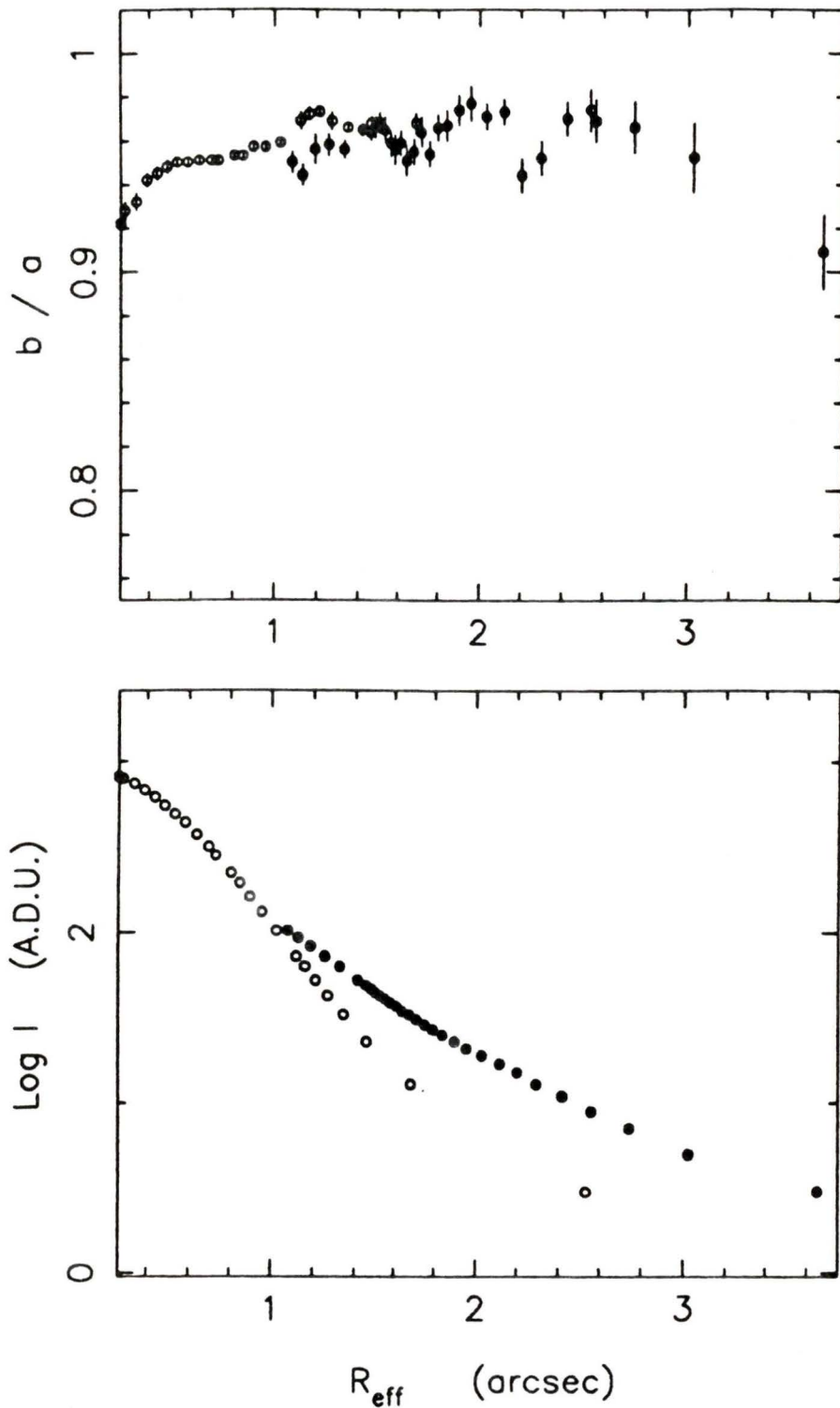


Figure 47: The variation of isophotal axial ratio with effective radius and the intensity profile of G280 (filled symbol) and a field star (open symbol). The observations were made through a V filter and the exposure time was 60s. The isophotal increment is 2 A.D.U. in the wings and 10 - 100 A.D.U. near the core.

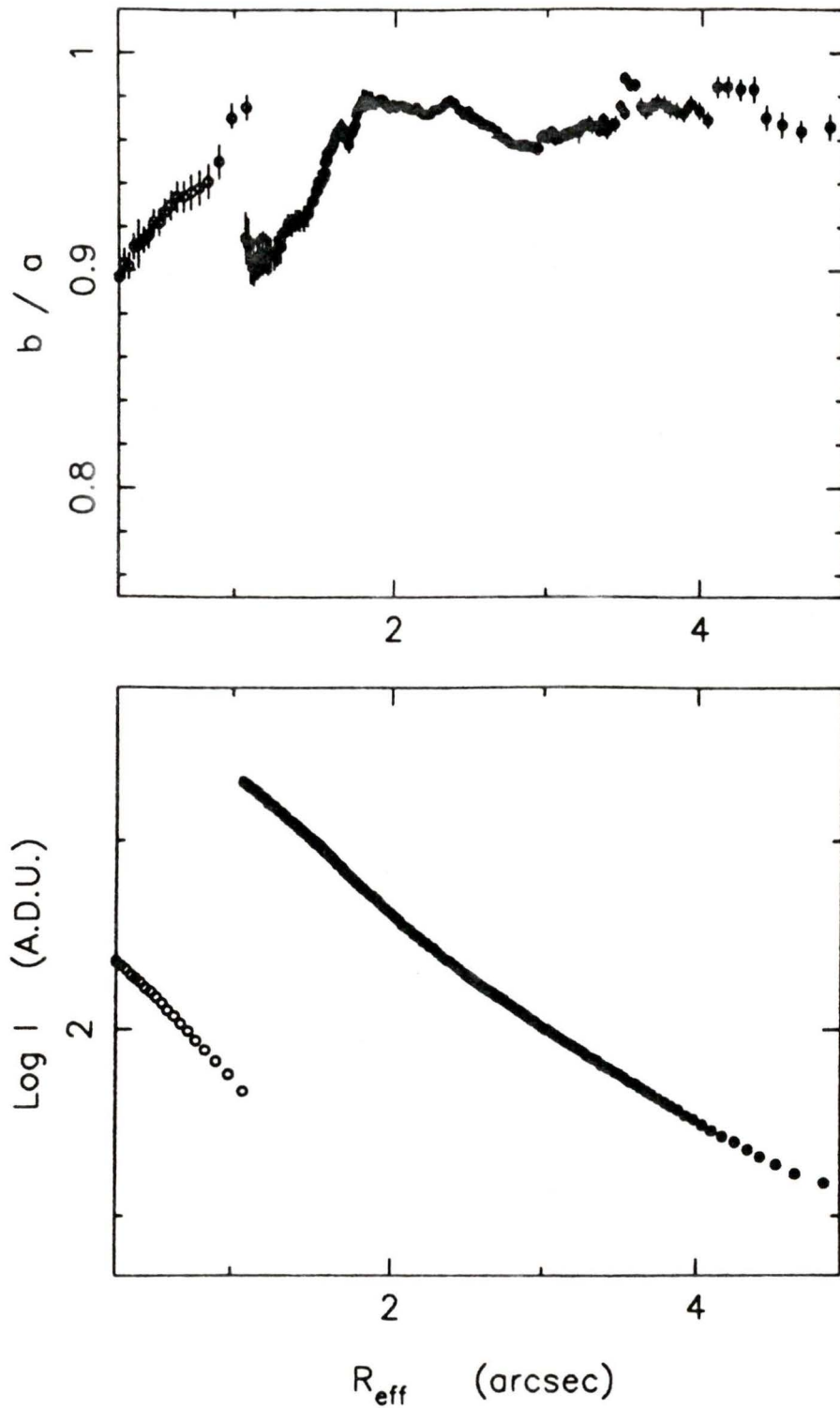


Figure 48: The variation of isophotal axial ratio with effective radius and the intensity profile of G280 (filled symbol) and a field star (open symbol). The observations were made through a B filter and the exposure time was 400s. The isophotal increment is 2 A.D.U. in the wings and 10 - 100 A.D.U. near the core.

Chapter 5

Results

The mean ellipticity and orientation measured for the M31 globular clusters observed and the root mean square deviations of these measurements are listed in Table 3. The number of isophotes, n , and the effective radius of the outermost isophote, $\text{Max } R_{eff}$, are also listed. Cluster orientations are measured north through east on the sky as described in Appendix D. Where possible, the mean cluster shape and position angle of the semi-major axis are computed for isophotes exceeding the critical effective radius of 3.3 arcsecond (see Section 3.1.3). Approximate values are given for those clusters whose outermost isophote does not extend beyond this critical value; these approximate measurements are included in the discussion that follows unless a more accurate measurement is given in Table 3 or otherwise stated. In the case of G217, it is the mean of the measurements listed in Table 3 which is included in the discussion that follows. The least flattened cluster measured with certainty in this sample is G280 ($\langle \epsilon \rangle = 0.024 \pm 0.009$). G1, alias Mayall II, is the most visually flattened globular in the sample; its measured mean ellipticity ($\langle \epsilon \rangle = 0.212 \pm 0.004$) reflects this observation.

Table 3: The Mean Ellipticity and Orientation Measured

Cluster	Exp Time	Filter	PSF ϵ	$\langle \epsilon \rangle \pm \sigma_\epsilon$	Limiting ϵ	$\langle \theta \rangle \pm \sigma_\theta$	Max R_{eff} (arcsec)	n
G1	60	V	0.037	$\sim 0.169 \pm 0.018$	> 0.198	$\sim 143 \pm 4$	2.793	5
	300	B	0.018	0.212 ± 0.004	$\gtrsim 0.243$	125 ± 1	4.595	16
G64	400	V	0.037	0.113 ± 0.016	—	146 ± 7	6.504	11
G72	500	B	0.139	0.107 ± 0.049	< 0.115	6 ± 1	3.748	2
	1000	B	0.202	0.109 ± 0.024	< 0.088	1 ± 7	4.990	9
G73	500	B	0.177	0.055 ± 0.009	< 0.068	—	4.370	4
G76	400	B	0.013	0.055 ± 0.002	$\gtrsim 0.044$	—	3.925	25
G78	400	B	0.064	$\sim 0.107 \pm 0.004$	> 0.068	$\sim 91 \pm 1$	2.484	24
G119	120	V	0.095	$\sim 0.037 \pm 0.011$	< 0.063	—	3.291	9
G148	120	V	0.016	$\sim 0.136 \pm 0.018$	—	$\sim 45 \pm 6$	2.822	4
G185	400	B	0.085	$\sim 0.054 \pm 0.003$	> 0.250	—	2.574	12
G205	400	B	0.153	$\sim 0.024 \pm 0.007$	< 0.078	—	2.669	7
G213	400	B	0.043	0.062 ± 0.032	> 0.133	87 ± 8	4.288	7
G217	120	V	0.109	0.047 ± 0.015	< 0.100	—	4.243	4
	400	V	0.175	0.075 ± 0.013	< 0.089	132 ± 5	4.860	7
G219	120	V	0.147	0.165 ± 0.013	$\gtrsim 0.126$	82 ± 2	4.687	12
G229	120	V	0.047	0.145 ± 0.039	> 0.087	34 ± 2	5.025	5
G257	120	V	0.153	$\sim 0.167 \pm 0.021$	< 0.076	$\sim 12 \pm 2$	3.633	8
G272	400	B	0.077	0.052 ± 0.014	—	—	5.334	10
G280	60	V	0.058	$\sim 0.046 \pm 0.021$	< 0.090	—	3.654	8
	400	B	0.069	0.024 ± 0.009	< 0.024	—	4.807	28

The bounds on cluster ellipticity given in Table 3 were obtained at the outermost isophote ($\text{Max } R_{eff}$) using the Moment method described in Section 3.2. Three of the clusters (G64, G148 and G272) could not be given limiting values with confidence due to the presence of contaminating images within the globular's image; the inclusion of these pixels at large radii would strongly bias the weighted moments used in the calculation of cluster attributes. These images also affect the attributes of the interpolated isophotes and therefore these isophotes were excluded from the computation of the mean shape and orientation of the globular. All the clusters in Table 3 with obtainable bounds on the ellipticity have measured mean flattening within the stated limiting values. A limiting value for cluster orientation could not be specified since the orientation of the point-spread function is unknown (see Section 3.2.2). Also, those globulars with $\langle \epsilon \rangle < 0.055$ have indeterminate orientations.

Figures 28 through 48 illustrate the intensity profile and variation of isophotal axial ratio with effective radius for each M31 globular cluster observed in this project and a stellar image in each field. The open symbol represents the stellar image in each figure and the error bars are calculated from the residuals of the fit of an ellipse to an isophote. In several of the figures, the globular's isophotes are as round or rounder than the stellar isophotes implying the projected cluster shape is circular. The measured ellipticity of these clusters (namely G73, G119, G185, G205, G213, G217, G257 and G280), as stated in Table 3, reflects this observation. The isophotal shape of the remaining clusters in the sample are flatter than the stellar images which implies the cluster flattening is physical and is not an artifact of the observations. Any variation in cluster shape with effective radius can be attributed to the presence of contaminating images or seeing effects.

The mean ellipticity of the globulars measured at various brightness levels and

their root mean square deviations are listed in Table 4. The majority of the ellipticities listed do not exceed 0.055; hence their corresponding orientations are indeterminate. The conversion of each frame from A.D.U./pixel to magnitude/arcsecond² was computed in the manner described in Appendix C. The four brightness intervals were chosen to span the data. Cluster shape was measured only for those brightness intervals in which there were a minimum of four isophotes 1σ above the sky and in which there was not an appreciable variation in isophotal axial ratio due to seeing effects. Also, any isophotes affected by the presence of contaminating images were excluded from the tabulated means. The tendency of isophotal shape to approach that of the point-spread function as brightness increases is clearly demonstrated in Table 4 (e.g., G213).

The mean flattening of the M31 globular clusters observed in this project is 0.094 ± 0.014 (the least certain of two measurements was excluded from this computation). Excluding the approximate measures of ellipticity listed in Table 3, the mean flattening of the sample is 0.097 ± 0.017 . Both of these results are in good agreement with the mean ellipticities reported by Lupton (1989), Staneva *et al.* (1985) and by Spassova *et al.* (1988) for larger samples of globulars (see Table 5).

Lupton has shown that the ellipticities measured in his outer annulus, B, are significantly flatter than those measured at smaller radii in annulus A. Based on this observation, Lupton argues the ellipticity of M31 globular clusters varies with radius. However, the existence of ellipticity variations requires confirmation since Lupton admits seeing “significantly affects” the determination of ellipticity in his annulus A. The isophotes included in the computation of the mean flattenings of the globulars listed in Table 3 are contained within Lupton’s annulus A, with the exception of G64, and the effects of seeing upon the shape of these isophotes has been demonstrated to be negligible for radii exceeding 3.3 arcseconds (see

Table 4: The Mean Ellipticity Measured at Various Brightness Levels

Cluster	Exposure Time (s)	PSF Ellipticity	Mean Ellipticity				Bound on Ellipticity
			22 - 23 mag arcsec ⁻²	21 - 22 mag arcsec ⁻²	20 - 21 mag arcsec ⁻²	19 - 20 mag arcsec ⁻²	
G1	60	0.037	————	————	————	————	>0.198
	300	0.018	————	————	0.212±0.004	————	≈0.243
G64	400	0.037	0.107±0.013	0.103±0.008	~0.080±0.004	————	————
G72	500	0.139	————	~0.143±0.018	~0.142±0.013	————	<0.115
	1000	0.202	0.109±0.036	~0.111±0.023	~0.133±0.006	————	<0.088
G73	500	0.177	0.054±0.010	~0.047±0.018	~0.028±0.003	————	<0.068
G76	400	0.013	————	0.054±0.001	0.055±0.003	————	≈0.044
G78	400	0.064	————	————	~0.110±0.002	————	>0.068
G119	120	0.095	————	————	~0.037±0.007	~0.043±0.004	<0.063
G148	120	0.016	————	————	————	————	————
G185	400	0.083	————	————	————	~0.054±0.003	>0.250
G205	400	0.153	————	~0.025±0.007	~0.027±0.010	~0.041±0.007	<0.078
G213	400	0.043	0.064±0.035	~0.049±0.013	~0.040±0.005	~0.037±0.004	>0.133
G217	120	0.109	————	0.051±0.023	~0.048±0.016	~0.052±0.009	<0.100
	400	0.175	————	0.086±0.016	~0.048±0.014	~0.047±0.006	<0.089
G219	120	0.147	————	0.155±0.011	0.168±0.008	————	≈0.126
G229	120	0.047	————	0.139±0.053	~0.119±0.016	————	>0.087
G257	120	0.153	————	————	~0.147±0.012	~0.180±0.014	<0.076
G272	400	0.077	0.047±0.014	————	————	————	————
G280	60	0.058	————	————	————	~0.036±0.008	<0.090
	400	0.069	0.027±0.010	~0.032±0.008	————	————	<0.024

Table 5: A Comparison of Mean Ellipticities of M31 Globular Clusters

Reference	Range of Ellipticity	$\langle \epsilon \rangle$	Sample Size
This work	0.02 – 0.21	0.10 ± 0.02	17
Lupton (annulus A)	0.00 – 0.24	0.08 ± 0.02	18
Lupton (annulus B)	0.04 – 0.24	0.12 ± 0.01	18
Spassova <i>et al.</i> (SSG)	0.02 – 0.27	0.10 ± 0.04	88
Staneva <i>et al.</i> (SSB)	0.02 – 0.26	0.11 ± 0.01	30

Section 3.1.3). If G64 and the clusters whose measured ellipticity is affected by seeing (*i.e.*, those clusters with approximate measures of flattening) are excluded from the sample, the mean ellipticity of the remaining clusters listed in Table 3 is 0.094 ± 0.016 . This value is not significantly different than Lupton’s mean measure in his annulus B (see Table 5) and suggests ellipticity does NOT increase with cluster radius. This result confirms the earlier work of Staneva *et al.* (SSB) (1985) whose isophotal measure of globular cluster flattening did not reveal ellipticity variations. The M31 globular clusters in their sample were observed during times of good seeing (1 – 1.5 arcseconds which is comparable to Lupton’s 1.08 arcseconds) and the range of isophotal radii for which cluster flattening was measured by SSB had a minimum radius of 1.5 arcseconds, which is smaller than the inner radius of Lupton’s annulus A, and extended beyond the outer radius of Lupton’s annulus B.

A comparison of the individual ellipticities measured with certainty for clusters in Table 3 that are common to Lupton’s (1989) sample is illustrated in Figure 49. The errors in Lupton’s measurements are estimated from his Figure 3. The observing conditions are comparable for the two samples and the isophotes used to compute the mean ellipticities of the clusters listed in Table 3 are contained within

annulus A.

Although the data are sparse, Figure 49 demonstrates the ellipticities listed in Table 3 are intermediate between those measured by Lupton in his A and B annuli. This is not surprising given the results of Table 5. Since Lupton admits seeing “significantly affects” his determination of ellipticity in his inner annulus, A, these results will not be discussed further. Figure 49 suggests Lupton’s measures of ellipticity in his annulus B are systematically larger than those measured in this project. The difference cannot be attributed to seeing effects since simulations indicate seeing does not affect the determination of ellipticity in Lupton’s annulus B (Lupton 1989) nor does it affect the data of this project that have been included in Figure 49 (see Section 3.1.3). Lupton observed a similarly systematic trend towards larger ellipticities in his data when compared with clusters in common with SSB (see Lupton’s figure 5). Contrary to Lupton’s claim, the seeing is comparable for these samples and therefore cannot be responsible for the observed difference in measured flattenings. However, the quality of Lupton’s coadded frames may be responsible for the observed systematic difference in measured ellipticity among these samples of globulars. Since the centers of the cluster images analyzed by Lupton were severely overexposed and the inner parts of the clusters were obliterated by charge bleeding along the axes of the CCD, the quality of the photometry and the accuracy of the determination of image centroids is questionable. An artificial ellipticity would be introduced in the coadded cluster image analyzed by Lupton if the images’ centroids were not accurately identified on the individual frames. Since it is not clear whether this effect was considered in the analysis of Lupton’s data, the ellipticities measured by Lupton will not be discussed further.

A comparison of the mean ellipticity of clusters in Table 3 that are measured with certainty and common to the sample of SSB is illustrated in Figure 50. The

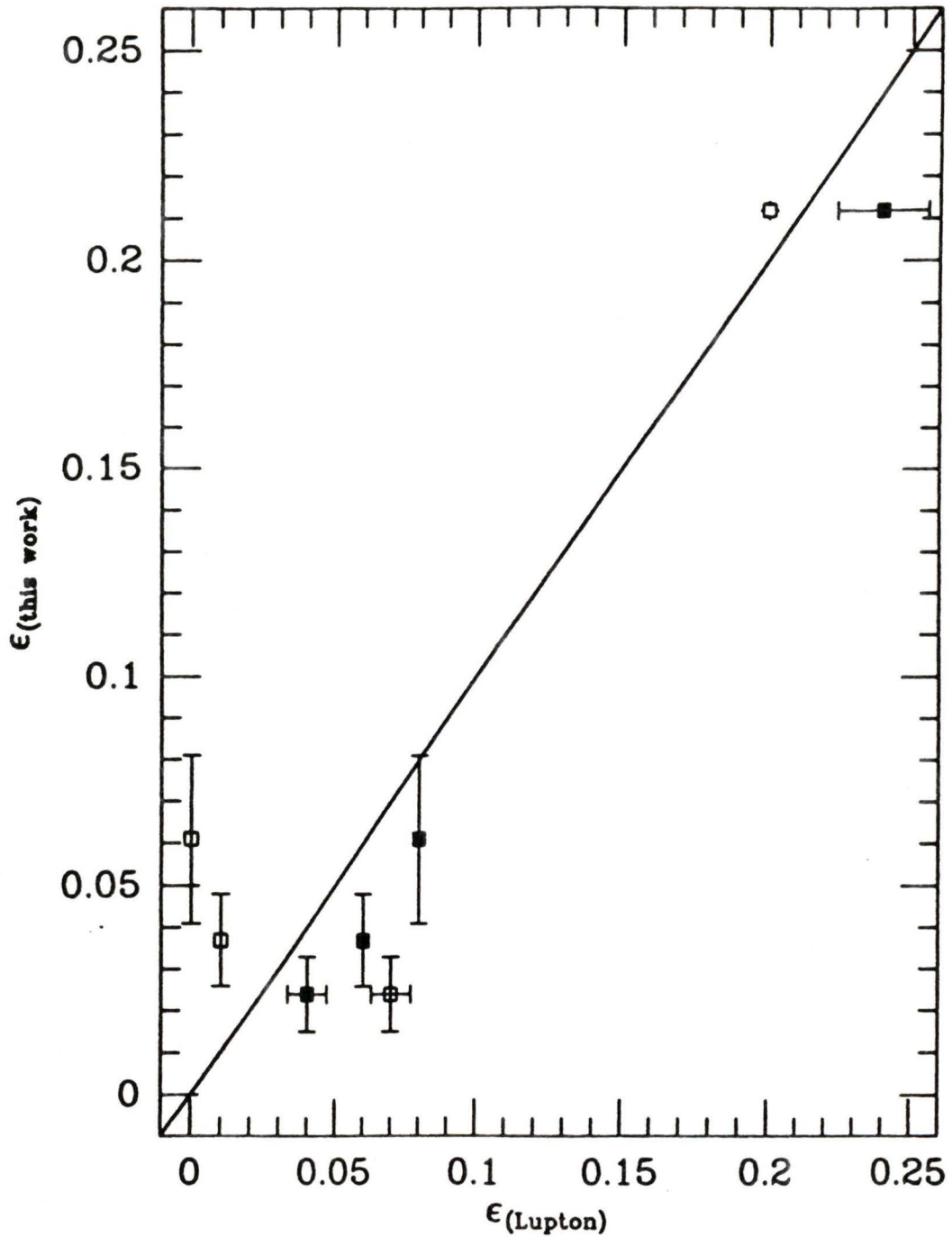


Figure 49: A comparison of the ellipticity of M31 globular clusters that are in common with Lupton (1989). The open symbol represents Lupton's measure at small cluster radii (his annulus A) and the filled symbol represents his measure at large radii (his annulus B). A line of unit slope is drawn.

results reported by Spassova *et al.* (SSG) (1988) duplicate, in part, the results of SSB but are less precise; thus the SSG measure of ellipticity is compared only when a more precise SSB value is unavailable. The measured flattening for Mayall II (Pritchett and van den Bergh, 1984) is included in Figure 50 since it was also observed in B. The probability of correlation of the measures of ellipticity listed in Table 3 with the combined SSB and SSG (SSG+SSB) sample is 99.8%. Since measuring errors exist for both the data in this project and the data of SSG+SSB, a least-squares fit to these data would be erroneous.

In summary, Figures 28 through 48 demonstrate that the flattening measured for each of the M31 globular clusters in this project is not an artifact of the observations but is physical. The mean flattening of the sample of globulars associated with the Andromeda Nebula listed in Table 3 is in good agreement with previous work but cannot substantiate the claim of Lupton (1989) that globular ellipticity varies with cluster radius. When the measured cluster flattenings listed in Table 3 are compared with previous works, the ellipticity measures reported by Lupton (1989) are observed to be systematically larger. This systematic difference can be attributed to the quality of the data in the Lupton's sample; hence these data will not be further discussed in this project.

Chapter 6

Discussion

The globular clusters in orbit about the Milky Way have been demonstrated to be slightly flattened (White and Shawl 1987 and references therein). Axial rotation appears to be the dominant mechanism producing the observed flattening (Pryor *et al.* 1986; Meylan and Mayor 1986, 1985; Mayor *et al.* 1984; Lupton *et al.* 1985). Since the globular clusters associated with the Andromeda Galaxy are similar to the Galactic globulars in size, colour, spatial distribution and range of metallicities (Crampton *et al.* 1985; van den Bergh 1988), a similar range and distribution of cluster ellipticity is expected for these extragalactic clusters.

Figure 51 compares the distribution of ellipticities of the globular clusters associated with the Andromeda Galaxy as measured in this project, with that of the Milky Way (MW) and the Magellanic Clouds. Although there are several sources of globular cluster ellipticity data for the Galaxy and the Large Magellanic Cloud (LMC) (see Table 6), the data in Figure 51 for the Milky Way are from White and Shawl (1987) and the LMC data are from Frenk and Fall (1982). These authors measure cluster flattening at radii which correspond, in the mean, to Lupton's annulus A (Lupton 1989) as do the measures in Table 3. The Small Magellanic

Table 6: Mean Ellipticities of Local Group Globular Clusters

Galaxy	$\langle \epsilon \rangle$	Sample Size	Reference
M31	0.10 ± 0.02	17	This work
Galaxy	0.08 ± 0.01	93	Frenk and Fall (1982)
Galaxy	0.07 ± 0.01	100	White and Shawl (1987)
LMC	0.11 ± 0.07	52	Frenk and Fall (1982)
LMC	0.22 ± 0.07	25	Geisler and Hodge (1980)
LMC	0.13 ± 0.12	25	Geyer and Richtler (1981)
SMC	0.17 ± 0.07	24	Kontizas <i>et al.</i> (1985)

Cloud (SMC) data in Figure 51 are from Kontizas *et al.* (1985). Although the mean error in ellipticity for each of these samples differs, none exceeds the bin size (see Table 6); hence the distribution of ellipticity in the SMC, LMC, Milky Way and M31 as illustrated in Figure 51 cannot be the result of errors in the measuring method employed.

A two-tailed Kolmogorov-Smirnov (K-S) test shows the hypothesis that the M31 globulars whose flattening has been measured with certainty in this project, and the Galactic globular clusters measured by White and Shawl (1987) were drawn from a parent population with the same ellipticity distribution can be rejected at the 90% confidence level. But, this sample of M31 globular clusters is consistent with the hypothesis that they were drawn from a parent population with the same ellipticity distribution as the LMC clusters measured by Frenk and Fall (1982). The LMC globulars have been demonstrated to be significantly flatter than the Galactic globulars (Frenk and Fall 1982; Geisler and Hodge 1980; Geyer and Richtler 1981) and the SMC clusters are significantly flatter than the LMC globulars (Kontizas

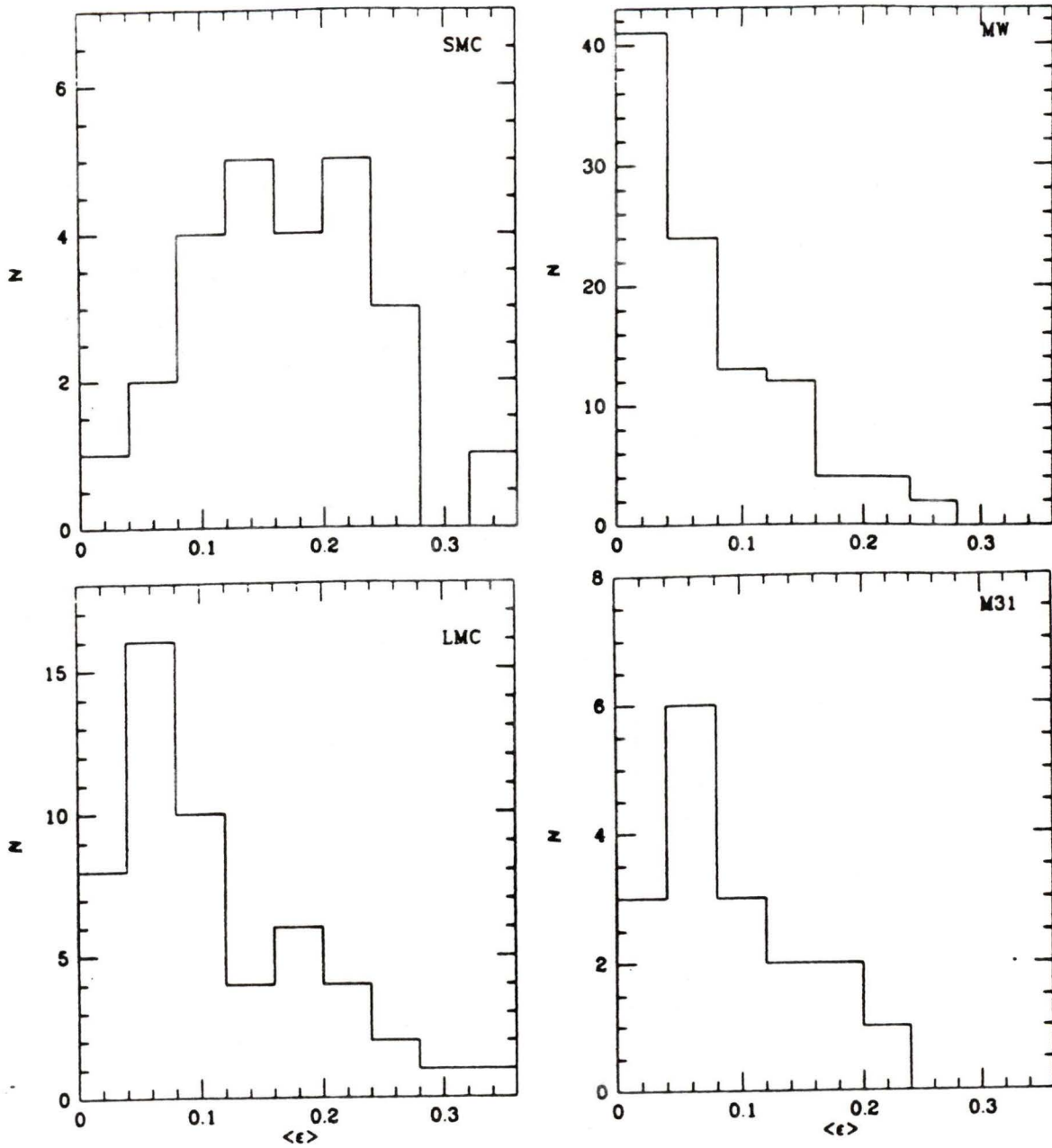


Figure 51: The distribution of M31 globular cluster ellipticity resembles that of the Large Magellanic Cloud (LMC) and not the Small Magellanic Cloud (SMC) nor the Milky Way (MW).

et al. 1985). The results of the K-S tests as applied to the data in this project are consistent with the findings of SSB and SSG. The mean radius at which SSB measure ellipticity for their sample of M31 globulars corresponds to that of the Galactic and LMC samples while the radius at which SSG measured cluster shape is unknown and therefore the results of SSG will not be included in the following discussion in which cluster ellipticities within the Local Group of Galaxies are compared. A two-tailed K-S test applied to the results of SSB shows the hypothesis that the Milky Way and M31 globular clusters were drawn from a parent population with the same ellipticity distribution can be rejected at the 99% confidence level. Although Figure 50 indicates the measures of ellipticity by SSB differ from those of this project, the means of the two samples are not significantly different (see Table 5) which suggests the measuring techniques employed are not necessarily responsible for the discrepancy in the confidence levels indicated by the results of the K-S tests applied to these samples. However, the preferential observation in this project of M31 globulars with magnitudes brighter than 16.1 in blue may be the source of the differences in the confidence levels; that is, there may not be a preponderance of bright, flat globular clusters associated with the Andromeda Galaxy. As Figures 52 and 53 illustrate, there is no evidence in this work to suggest a correlation of M31 globular cluster ellipticity with B or V magnitude. The linear correlation coefficient, r , is -0.48 for B and 0.19 for V which correspond to probabilities of correlation less than 75% and 20% respectively. The apparent magnitudes are from Crampton *et al.* (1985) and the approximate measures of ellipticity in Table 3 were excluded. The absence of a correlation of ellipticity with apparent magnitude is consistent with the work of SSB (and SSG) and reinforces the anomalous nature of the M31 globulars since the brightest globular clusters associated with the Galaxy, NGC 5128, and LMC are also the flattest (van den

Bergh 1984, 1983).

Since the globular clusters associated with M31 are similar in many ways to the Galactic globulars, an obvious and important question is whether selection effects are responsible for the evidence provided by the data in this project, and by SSB, that the M31 globular clusters are flatter than those of the Milky Way at radii comparable to the galactic measures of White and Shawl (1987).

6.1 Selection Effects

The effects of seeing upon the determination of cluster shape are expected to be more problematic for the M31 clusters than those of the Galaxy or Magellanic Clouds since M31 and its globulars are a greater distance from the Milky Way. The mean point-spread function of this work is elliptical in shape (see Table 2) and could therefore affect the measured ellipticities. However, the effects of seeing upon the measures of ellipticity listed in Table 3 have been modelled and determined to be negligible for isophotal effective radii exceeding 3.3 arcseconds (see Section 3.1.3); those clusters whose measured shape have been biased by the seeing profile were excluded from the Local Group comparisons. Also, as Figure 54 illustrates, the measured ellipticity of the M31 globulars in this project do not correlate with right ascension nor declination; hence guiding is not responsible for the observed ellipticity. (Clustering of the points about either of the coordinate axes in Figure 54 would indicate a correlation of measured ellipticity with celestial direction.)

It is not clear whether the effects of seeing have been modelled for the isophotal technique of SSB. However, Figure ?? demonstrates the ellipticities measured by SSB are not the result of guiding errors since the data do not cluster about the coordinate axes in this figure. Also, SSB report the mean ellipticity of their

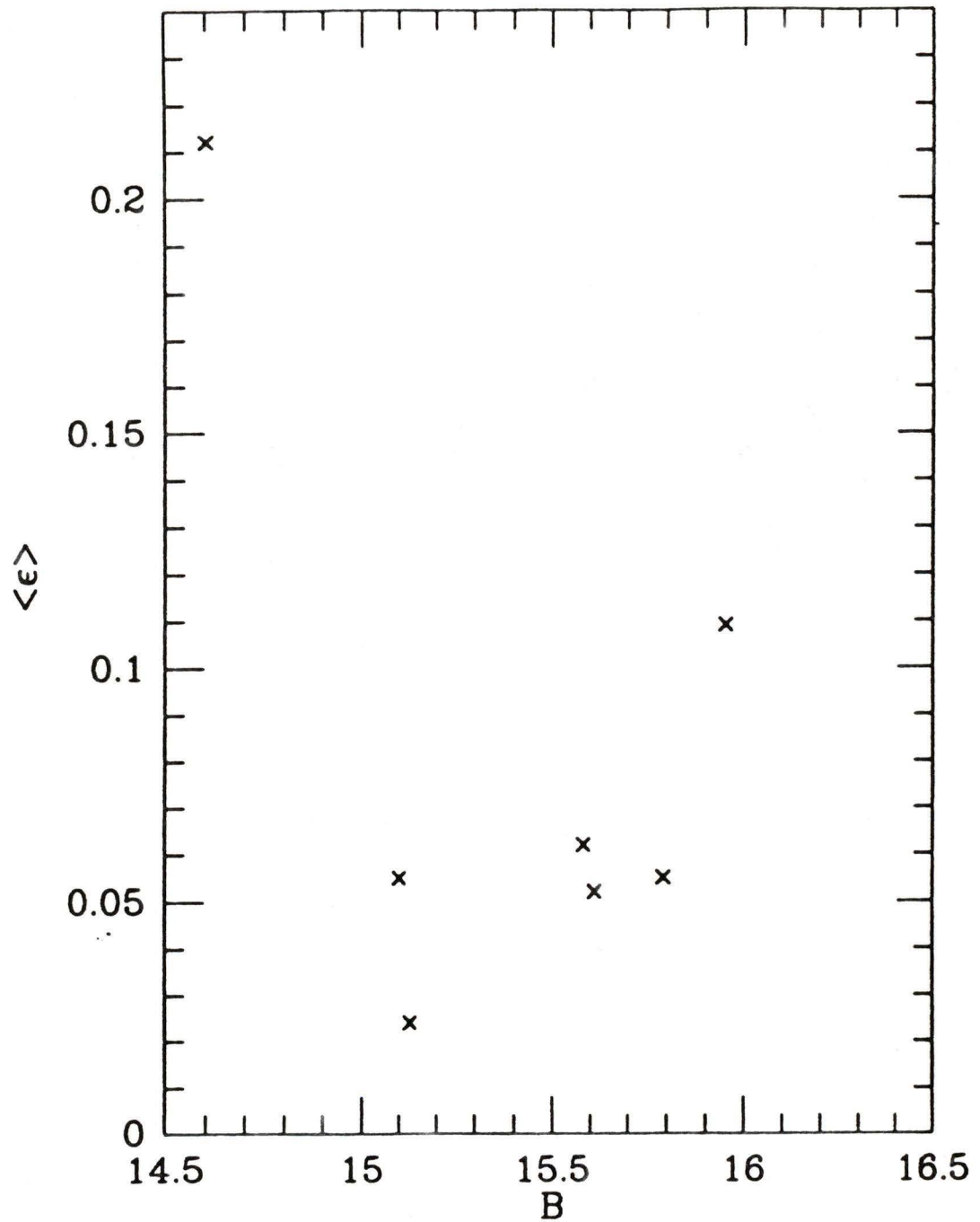


Figure 52: No correlation of ellipticity with B is observed for the M31 globular clusters of this work. The linear-correlation coefficient is -0.48

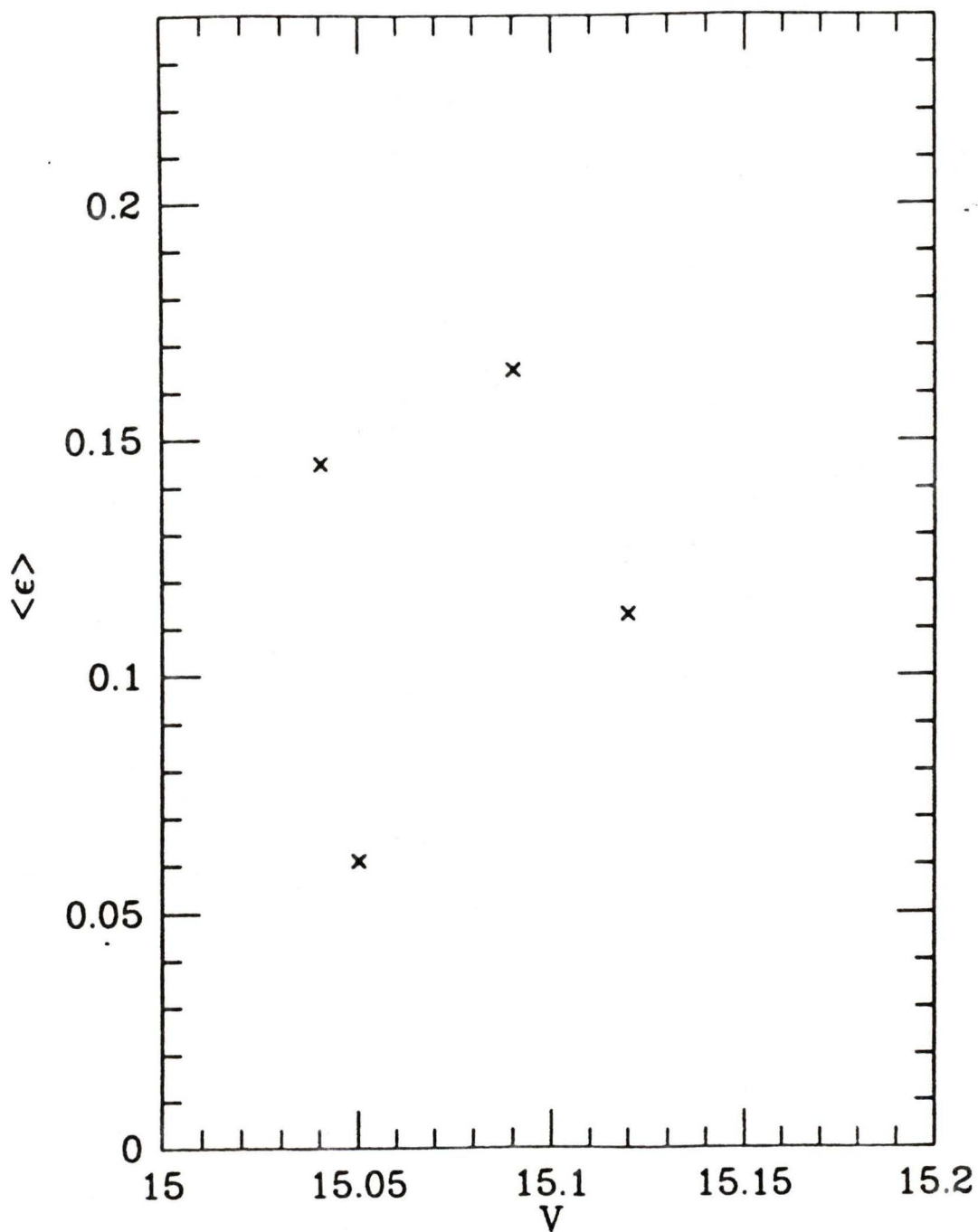


Figure 53: No correlation of ellipticity with V is observed for the M31 globular clusters of this work. The linear-correlation coefficient is 0.19

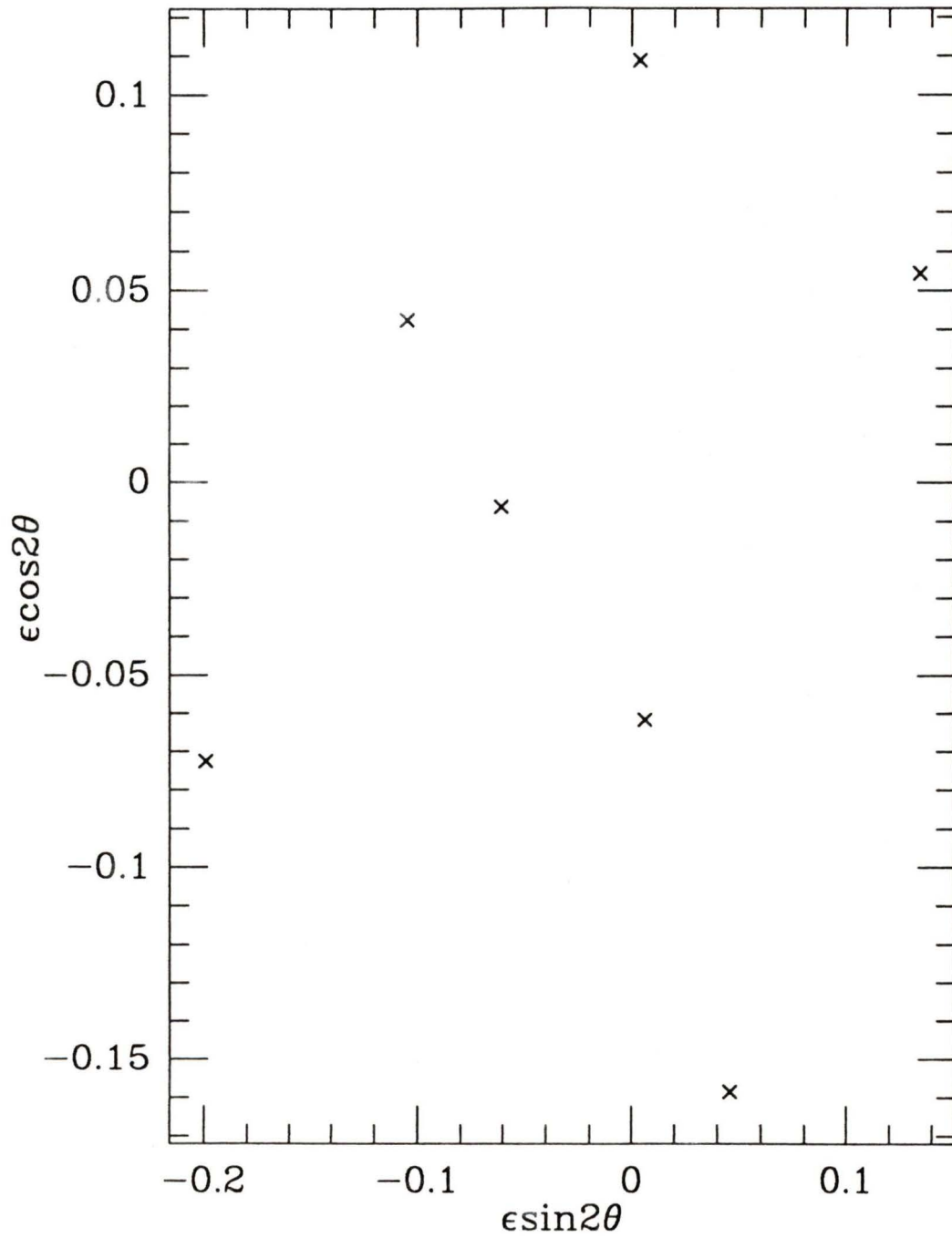


Figure 54: No correlation of measured ellipticity with celestial direction is observed for the the M31 globular clusters in this work.

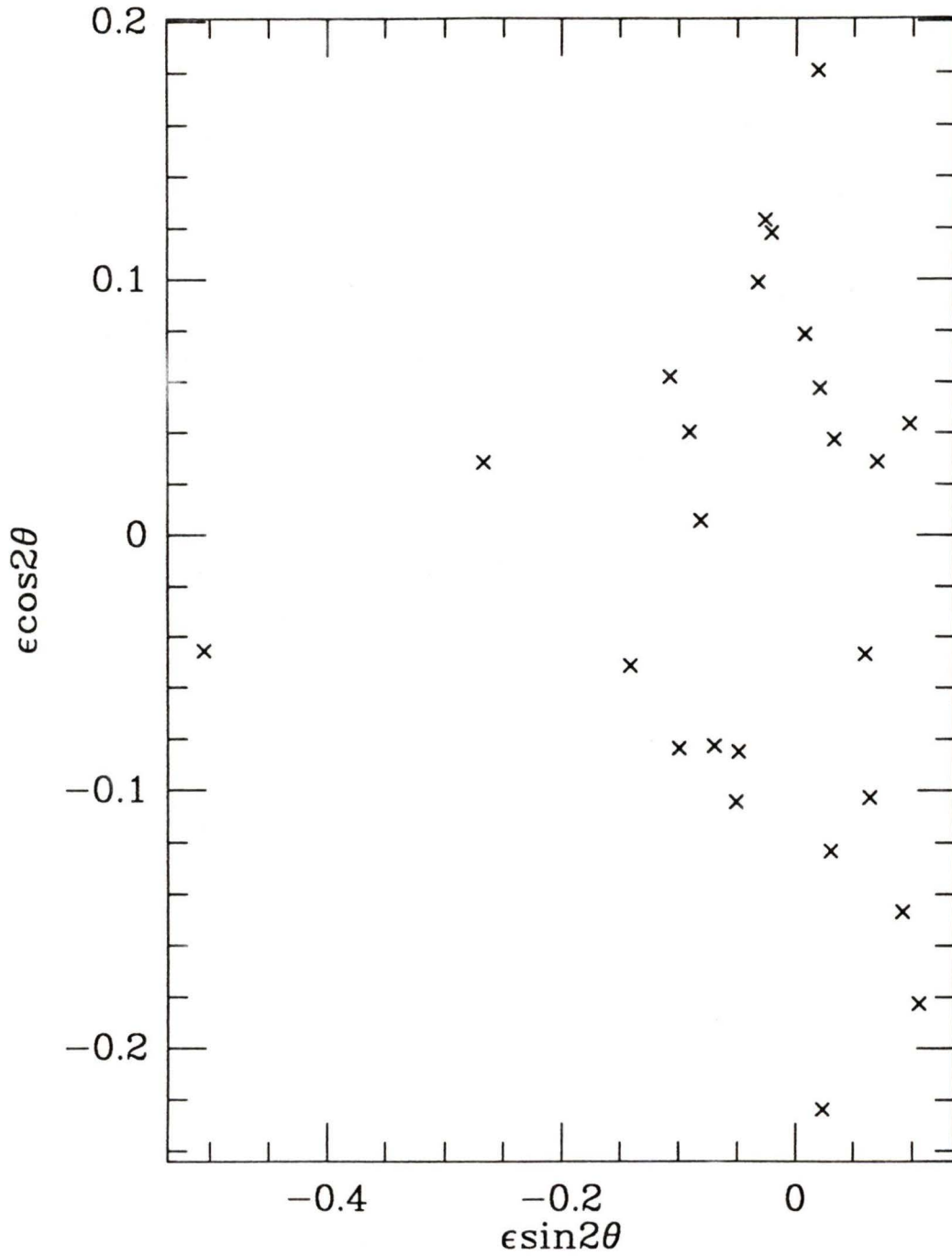


Figure 55: No correlation of ellipticity with celestial direction is observed for the the M31 globular clusters measured by SSB.

point-spread function is $0.02 - 0.03$. Since this value is rounder than the mean of Table 2, the ellipticities measured by SSB should be rounder on average than those values listed in Table 3; yet the mean ellipticity for their sample of globulars is not significantly different than that of this project (see Table 5) and the SSB data result in a stronger rejection of the hypothesis that the M31 and Galactic globular clusters were drawn from a parent population with the same ellipticity distribution. The effects of seeing therefore cannot be responsible for the observed distribution of ellipticity among M31 globular clusters.

Van den Bergh (1984) has demonstrated that patchy foreground absorption increases the measured ellipticity of Galactic globulars. Assuming a value of 3.0 for the ratio of absorption in the visual spectrum, A_V , to the colour excess (van den Bergh 1988), the absorption has been computed for the M31 globular clusters listed in Table 3 and those in the sample of SSB using the colours of Crampton *et al.* (1985). The data are plotted in Figures 56 and 57. The probability of correlation (P_c) is less than 10% for each sample. The measured shape of the M31 globulars are therefore not affected by background absorption. Since the foreground absorption is constant and small (0.3 mag) for these clusters, the effect on the shape of the distribution would be negligible and the apparent anomalous flattening of the M31 clusters would persist.

The Andromeda Galaxy is a massive spiral galaxy consisting of a luminous bulge and a disk. The differential background light contribution of the galaxy to the globular cluster data could produce an erroneous measure of ellipticity. As mentioned in Chapter 4, G185 was the only cluster listed in Table 1 in which a gradient in the background light was observed and subsequently subtracted. Since the outermost isophote describing the shape of this cluster does not extend into the regime where seeing effects are negligible, this cluster was excluded from the

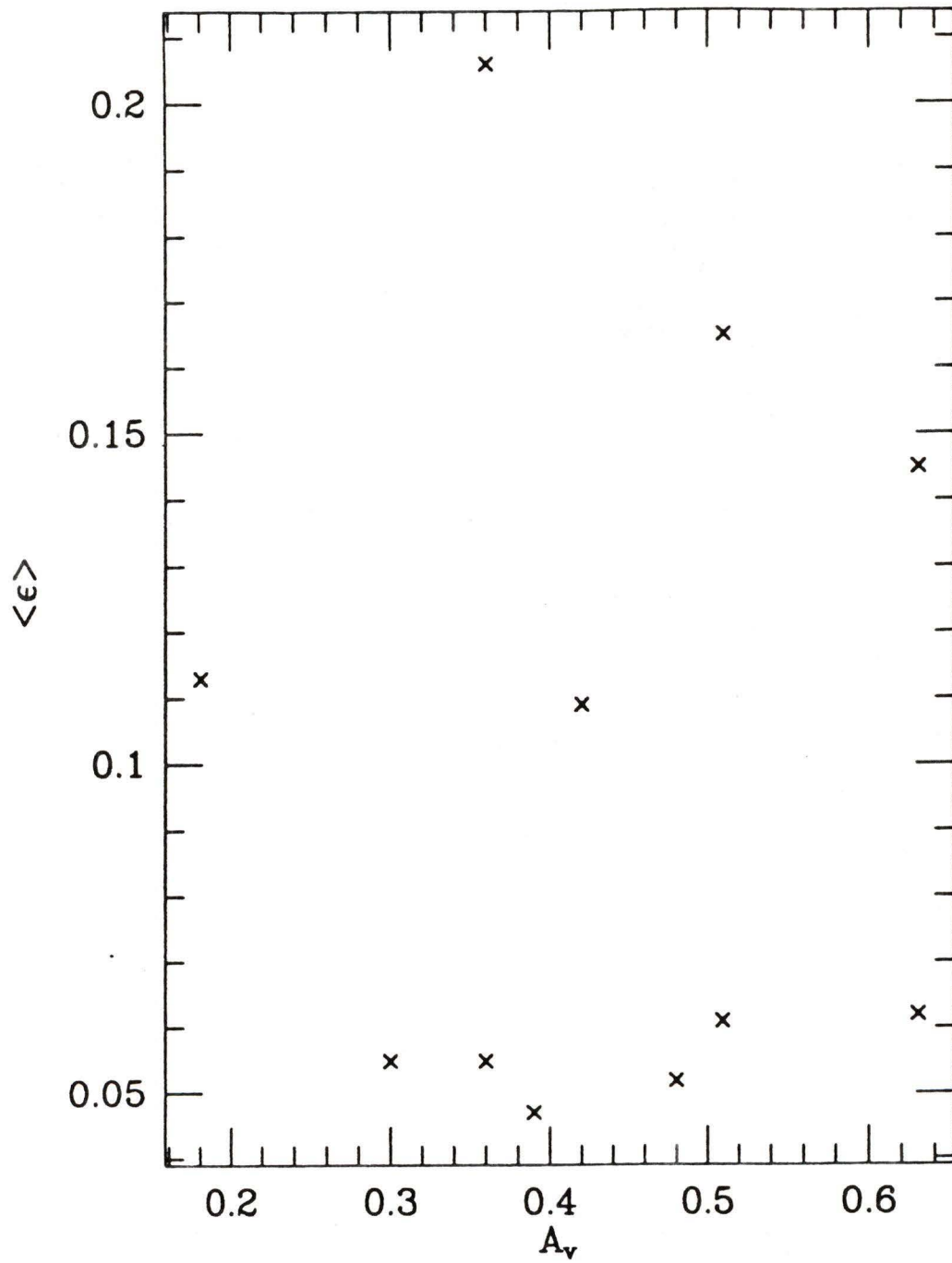


Figure 56: No correlation of ellipticity with absorption is observed for the M31 globular clusters of this work. The linear-correlation coefficient is 0.02

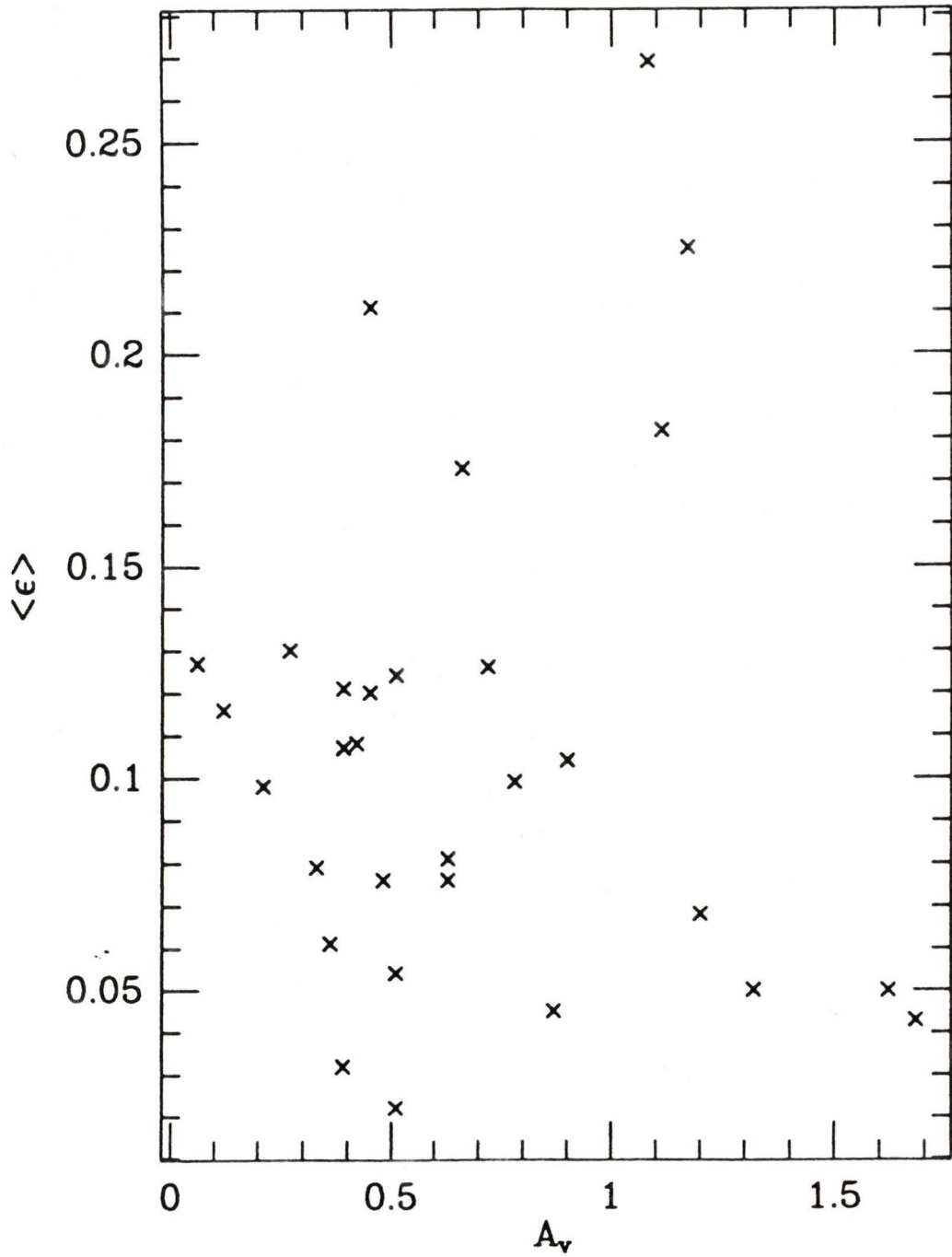


Figure 57: No correlation of ellipticity with absorption is observed for the M31 globular clusters measured by SSB. The linear-correlation coefficient is -0.02

sample compared to the Milky Way data of White and Shawl. Similarly, SSB have anticipated the problem of the brightness gradient in the spiral structure of M31 and have subtracted a background level that compensates for the gradient in background light prior to measuring the globular's ellipticity. Therefore a differential background light contribution does not affect the results of the comparison of the M31 data to the Milky Way data of White and Shawl.

In light of these arguments, selection effects cannot be responsible for the apparent anomaly in the distribution of ellipticities measured for the globular clusters associated with the Andromeda Galaxy and the hypothesis that the M31 and Milky Way globulars are drawn from a parent population with the same ellipticity distribution must be rejected. The level of confidence with which this rejection can be made is weaker for the ellipticity measures of this work than those of SSB, but the preferential observation of bright M31 globular clusters in this project may be responsible for this discrepancy.

Based upon the observed difference in cluster flattening between the Galaxy and the Large Magellanic Cloud, van den Bergh (1984) has argued the cluster-forming processes are likewise different. The radial velocity studies of Pryor *et al.* (1986), Meylan and Mayor (1986, 1985), Mayor *et al.* (1984) and Lupton *et al.* (1985) for some Galactic globular clusters suggest the dominant mechanism flattening the Milky Way globulars is axial rotation. The rotational velocity determined by these authors for Galactic globulars with measured ellipticity is in good agreement with that predicted by King (1961) who has shown that if the total angular momentum of the collection of stars comprising a globular cluster is not zero, then an average rotational velocity can be ascribed to the system. The relation between this rotational velocity, ω , and the overall shape of the system, claims King, is given by:

$$\omega^2 = \frac{16}{15}\pi G\epsilon\rho \quad (32)$$

where G is the gravitational constant, ϵ is the ellipticity of the cluster and ρ is the density of a homogeneous, oblate spheroid and is assumed to be constant. At present, rotational velocity data are not available for the globular clusters associated with the Andromeda Nebula and since these clusters are flatter than those of the Milky Way, perhaps the observed flattening of the M31 globulars is not the result of axial rotation but some other cluster attribute such as mass, age, metal abundance or tidal forces.

6.2 Possible Causes of Flattening

As previously mentioned, van den Bergh (1984, 1983) has drawn attention to the fact that the brightest globular clusters associated with the Large Magellanic Cloud, NGC 5128 and the Galaxy are also the flattest but there is no evidence in this work to suggest a correlation of M31 globular cluster ellipticity with B or V magnitude (see Figures 52 and 53). The absence of a correlation of ellipticity with apparent magnitude is consistent with the work of SSB and of SSG and implies globular cluster mass is not responsible for the observed ellipticity of M31 clusters. It is interesting to note however, that the most massive M31 globular, Mayall II, is one of the flattest (Pritchett and van den Bergh 1984).

Cowley and Burstein (1988) have measured the ultraviolet (UV) flux for 11 M31 globular clusters and they suggest UV flux may correlate with age. If further investigation proves this relation to exist, then Figure 58 which illustrates the absence of a correlation of measured ellipticity with UV flux, would imply the ellipticity of M31 globular clusters does not correlate with age ($P_c < 20\%$). The

approximate measures of ellipticity listed in Table 3 have been excluded from this (and the following) test of correlation.

The intrinsic $(B-V)_o$ colour of the globular clusters in this project have been reported by Elson and Waltherbos (1988). Van den Bergh (1967) has shown that the intrinsic colour of M31 globulars is related to the cluster's metallicity index, which, as Hartwick and Sargent (1974) have pointed out, is a good indicator of metal abundance for globular clusters. Hence, any observed correlation between ellipticity and intrinsic colour would imply a relation between the flattening and the metal abundance of the M31 globular clusters. The probability of correlation is 81% for the M31 globulars in this project (Figure 59) and 64% for the combined SSB and SSG sample (Figure 60). As previously mentioned, the sample of SSB is a more precise subset of the ellipticity measures reported by SSG and therefore, when possible, the more precise SSB measure is substituted for the SSG value. When the sample is divided into "red" ($(B-V)_o > 0.75$) and "blue" ($(B-V)_o \leq 0.75$) globulars, a correlation of cluster shape with cluster metal abundance still is not observed.

If tidal forces are responsible for the observed flattening of M31 globular clusters, then the major axes of the clusters should point preferentially towards the center of the Andromeda Galaxy. The probability of a correlation of ellipticity with axis orientation relative to M31 is $< 65\%$ for the data of this work and $< 85\%$ for SSB (SSG do not report cluster orientations). Figures 61 and 62 illustrate these results; θ is the projected angle between the semi-major axis of the globular and the core of M31. Similarly, no correlation is observed between cluster ellipticity or orientation and cluster projected galactocentric distance (D_p) reported by Crampton *et al.* (see Figures 63 through 66). It should be noted that the implied correlation of ellipticity with D_p in Figure 63 for the clusters listed in Table 3 does not persist

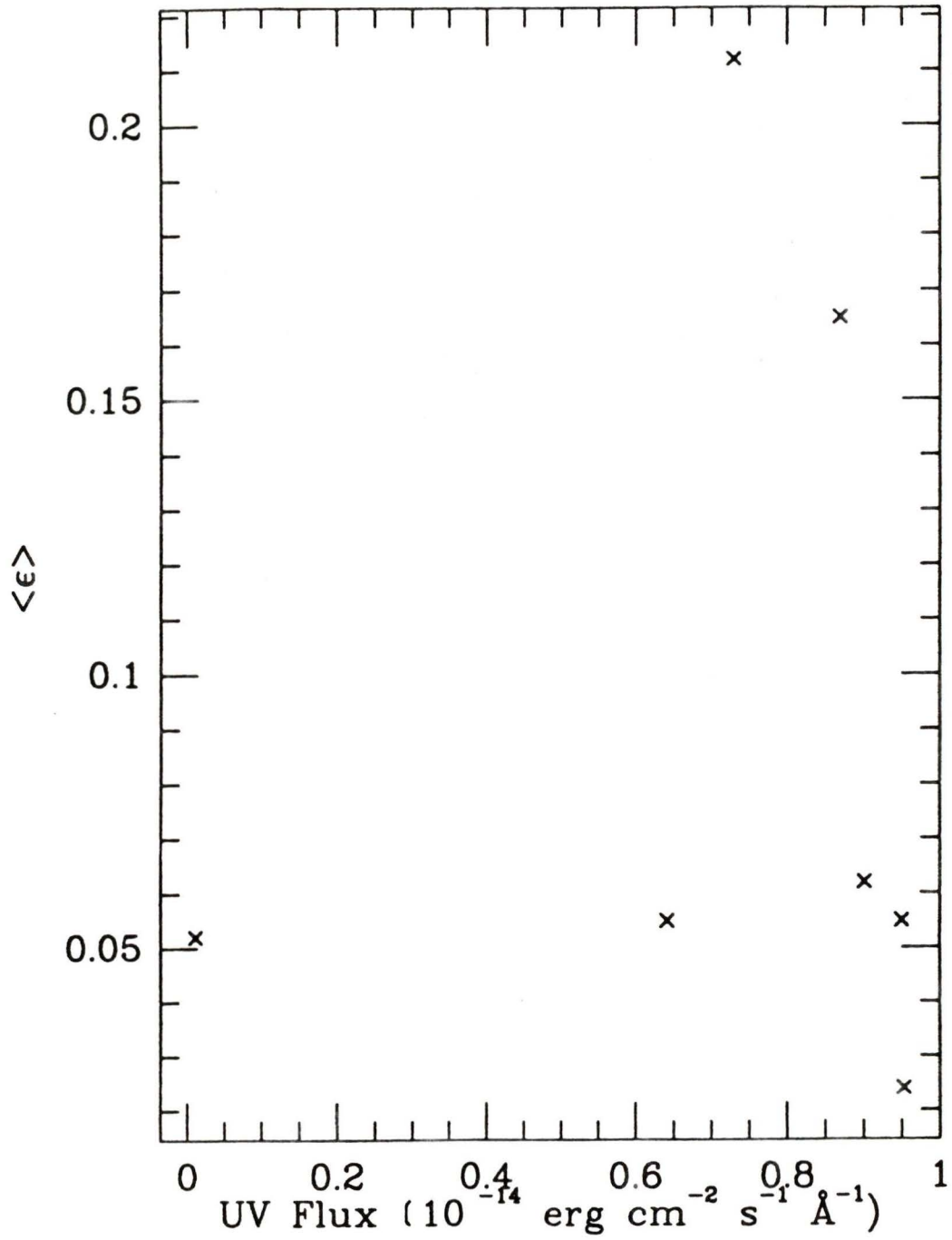


Figure 58: No correlation of ellipticity with UV flux measured by Cowley and Burstein (1988) is observed.

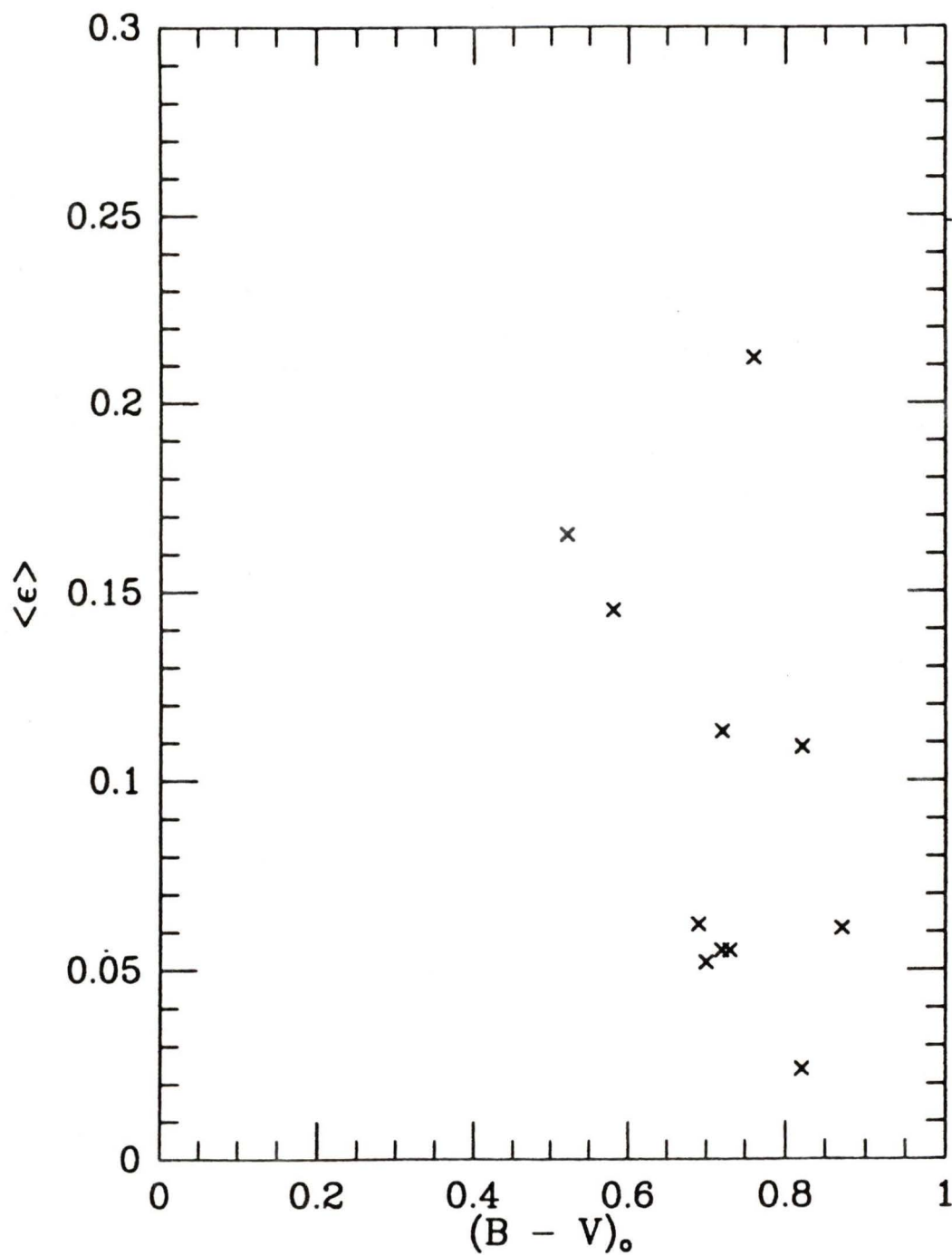


Figure 59: No correlation of ellipticity with intrinsic colour is observed for the M31 globular clusters of this work. The linear-correlation coefficient is -0.43

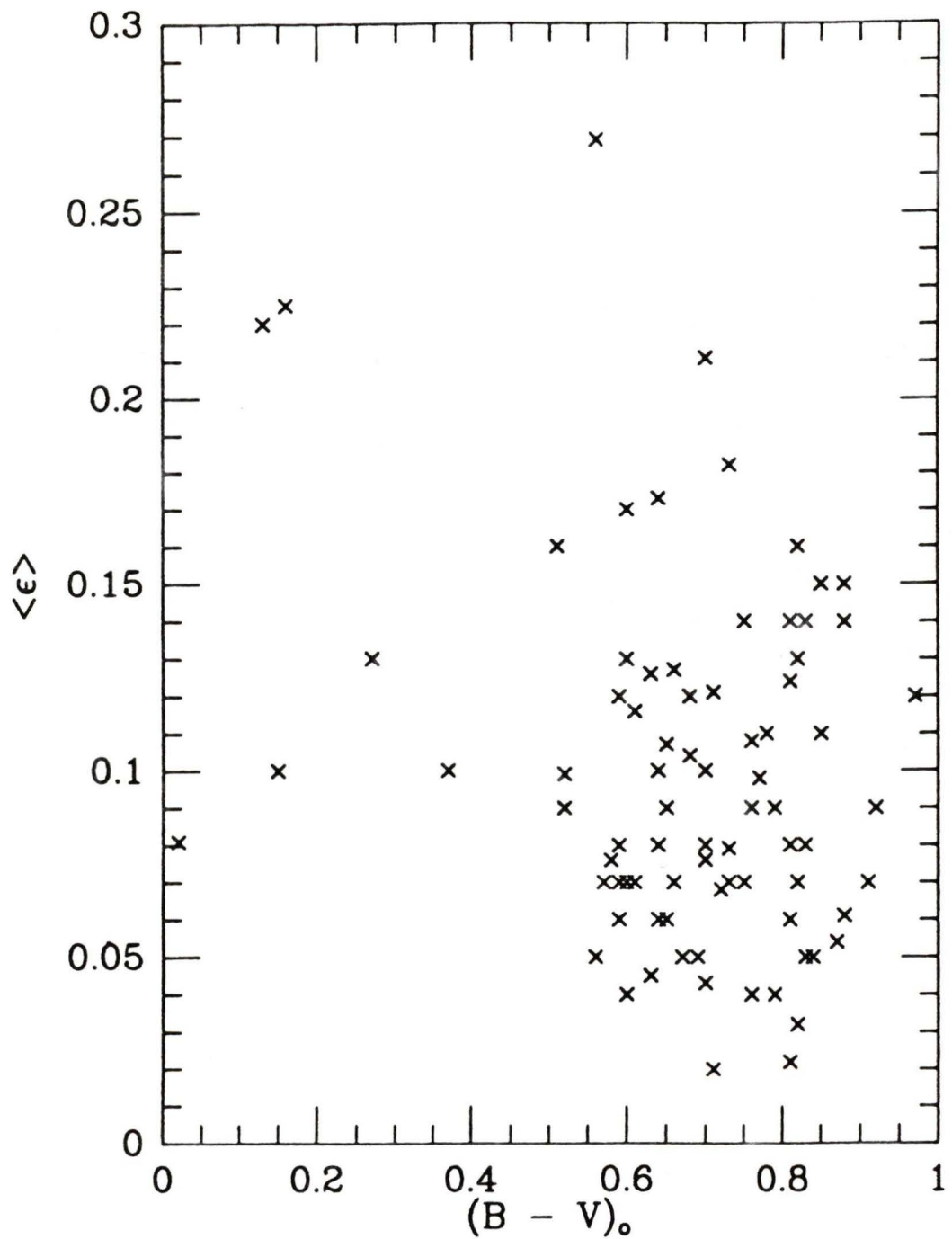


Figure 60: No correlation of ellipticity with intrinsic colour is observed for M31 globular clusters in the combined sample of SSB and SSG. The linear-correlation coefficient is 0.10

when the M31 ellipticity data of SSB and SSG are combined and is probably a selection effect since the absolute magnitude of M31 globulars correlates with D_p (van den Bergh, 1984).

The observed correlation of M31 globular cluster ellipticity measured by SSB and cluster radial velocity (Figure 67) can also be attributed to selection effects. The radial velocity data is primarily from Huchra *et al.* (1982); additional data (5 measurements) are from van den Bergh (1969) which Huchra *et al.* demonstrate to be in good agreement with their measurements. Approximately half the M31 globulars with measured ellipticity also have measured radial velocities; Huchra *et al.* preferentially observed the brightest clusters and the X-ray clusters. Hence, radial velocity data is not available for most of the flat ($\epsilon > 0.15$) faint ($V > 15.5$) M31 globulars. Any comments regarding the existence of a correlation between cluster shape and radial velocity for the M31 globulars must therefore await the compilation of a more complete sample of radial velocity measurements.

The consistent lack of systematic trends of M31 globular cluster ellipticity with observed cluster properties may be the result of projection effects. All the ellipticity measures reported refer to the shape of the globulars as observed on the sky and may not accurately reflect the true cluster flattening. The effect of the projection would be to ‘smear’ the ellipticity measures to larger values thereby suppressing any correlation that may exist. A distinctive feature of this effect would be the noticeable absence of data in a triangular region on each correlation plot. For Figures 52 through 67, this triangular region would have its base along the horizontal axis ($\epsilon = 0.0$) and its height would be measured vertically from the lower right corner. Since there is *not* an absence of data in this triangular region on any of these figures, the consistent lack of systematic trends of M31 globular cluster ellipticity with observed cluster properties is not the result of projection effects. The

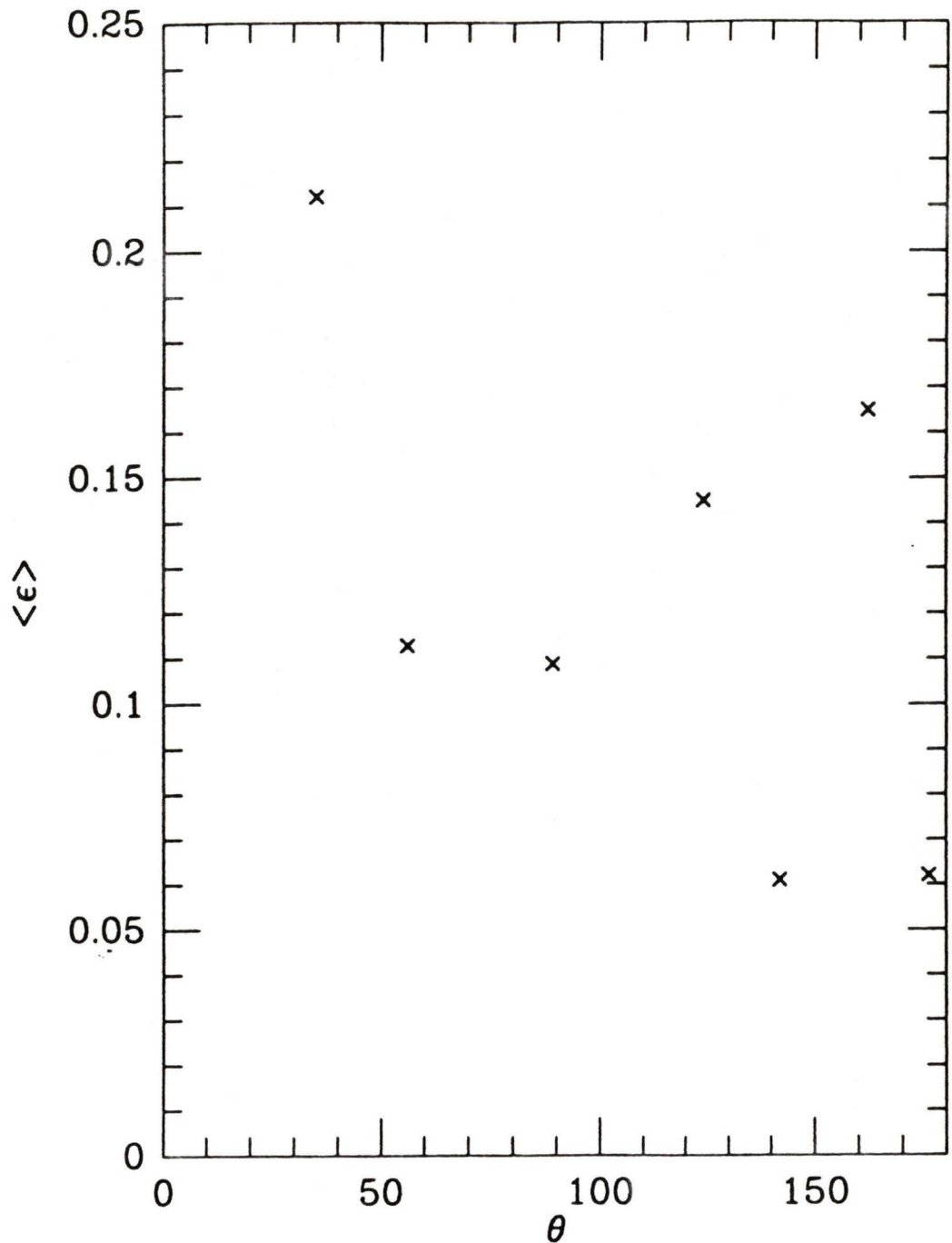


Figure 61: No correlation of ellipticity with orientation is observed for the M31 globular clusters of this work; θ is the projected angle between the semi-major axis of the globular and the core of M31. The linear-correlation coefficient is -0.36

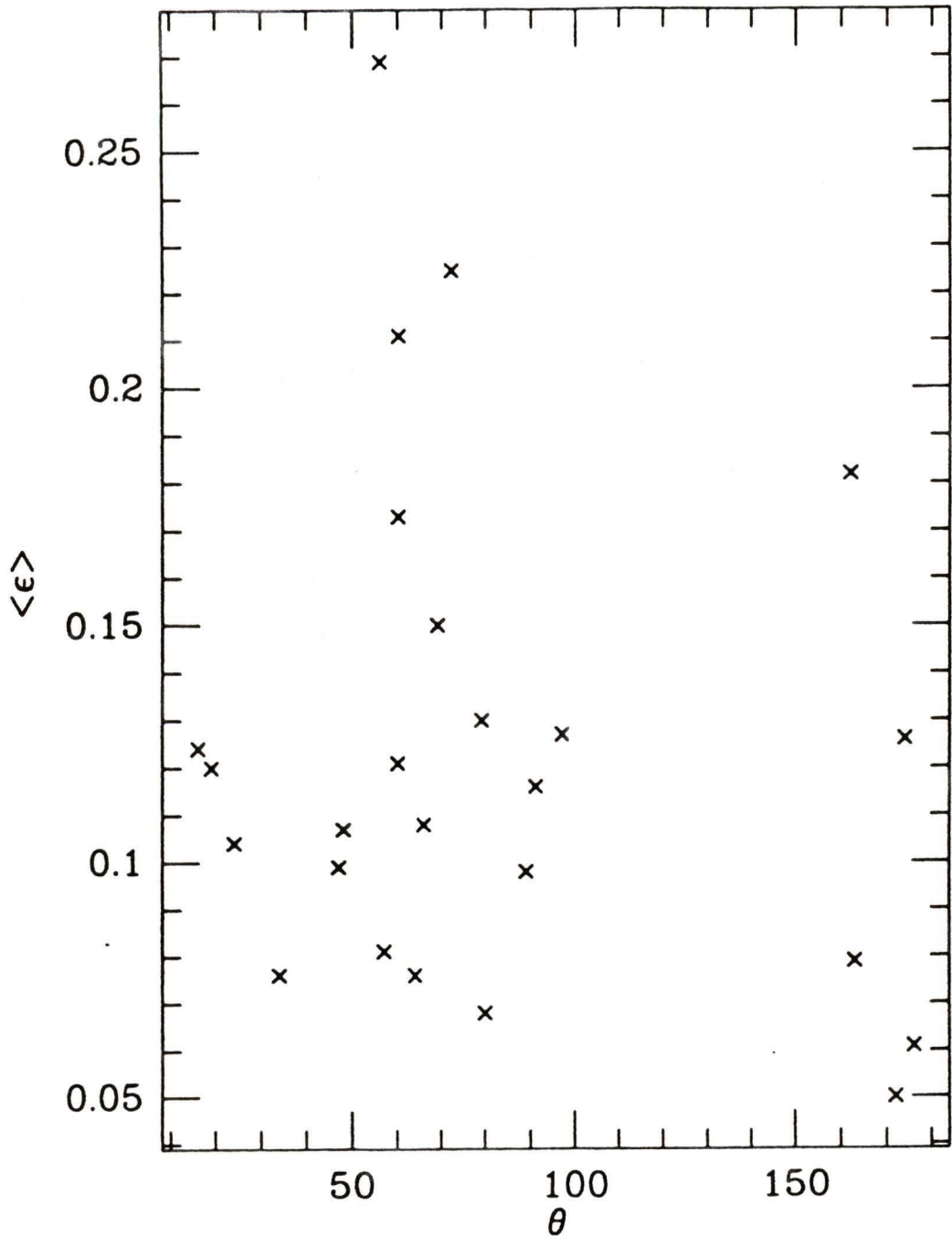


Figure 62: No correlation of ellipticity with orientation is observed for the M31 globular clusters in the sample measured by SSB; θ is the projected angle between the semi-major axis of the globular and the core of M31. The linear-correlation coefficient is -0.31

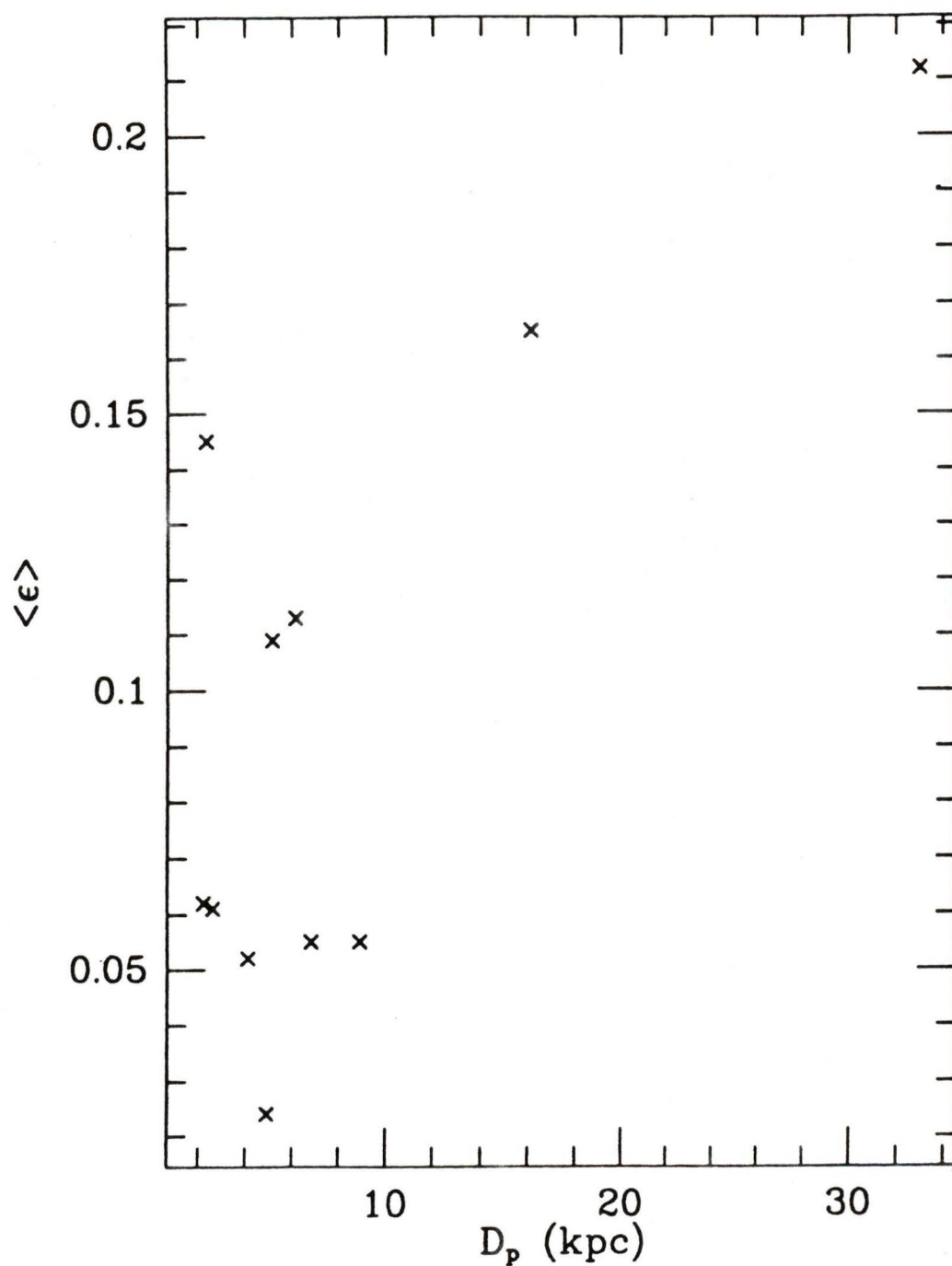


Figure 63: The apparent correlation of ellipticity with projected galactocentric distance is due to selection effects (see text).

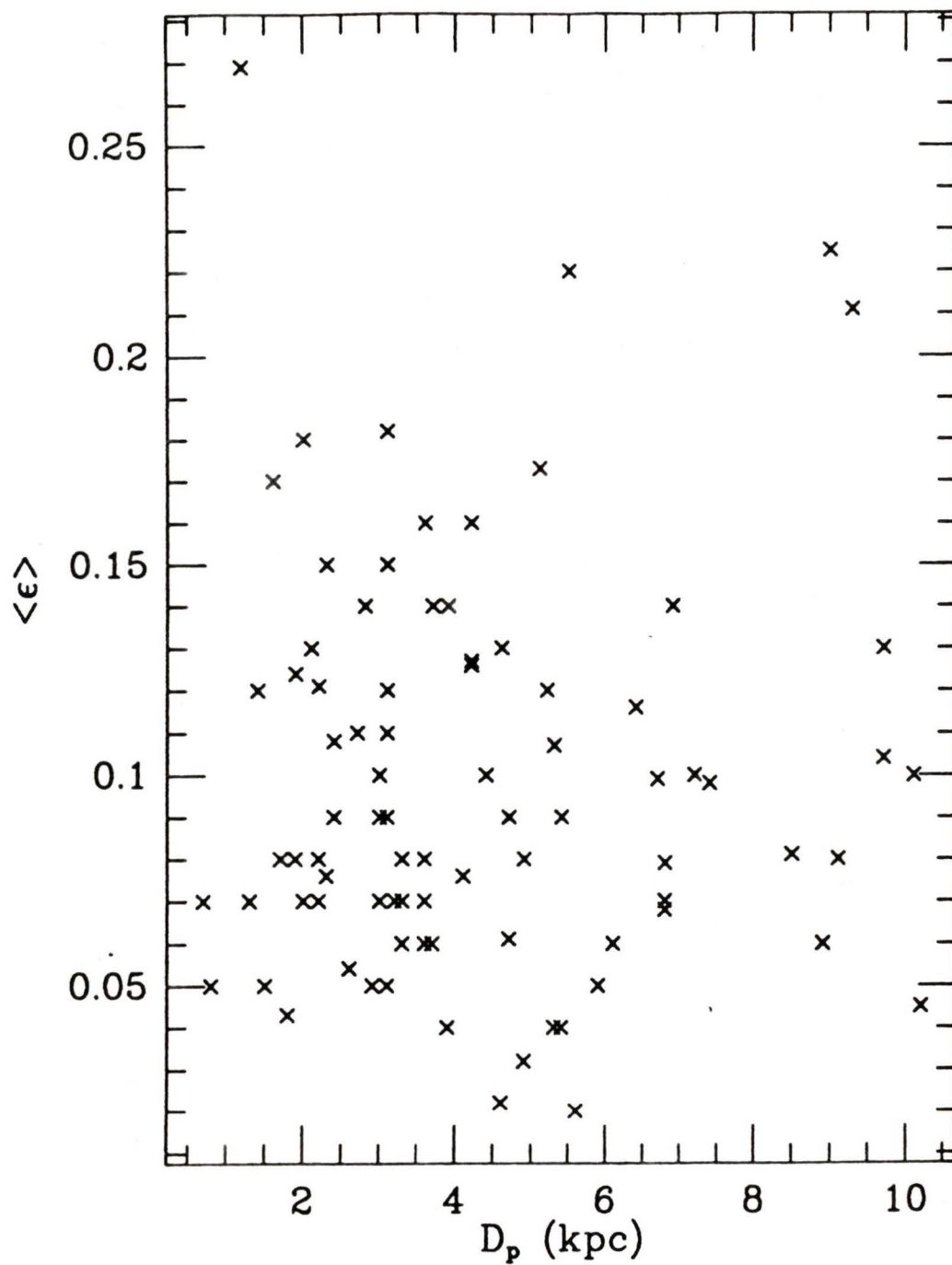


Figure 64: No correlation of ellipticity with projected galactocentric distance is observed for M31 globular clusters when the samples of SSB and SSG are combined. The linear-correlation coefficient is 0.02

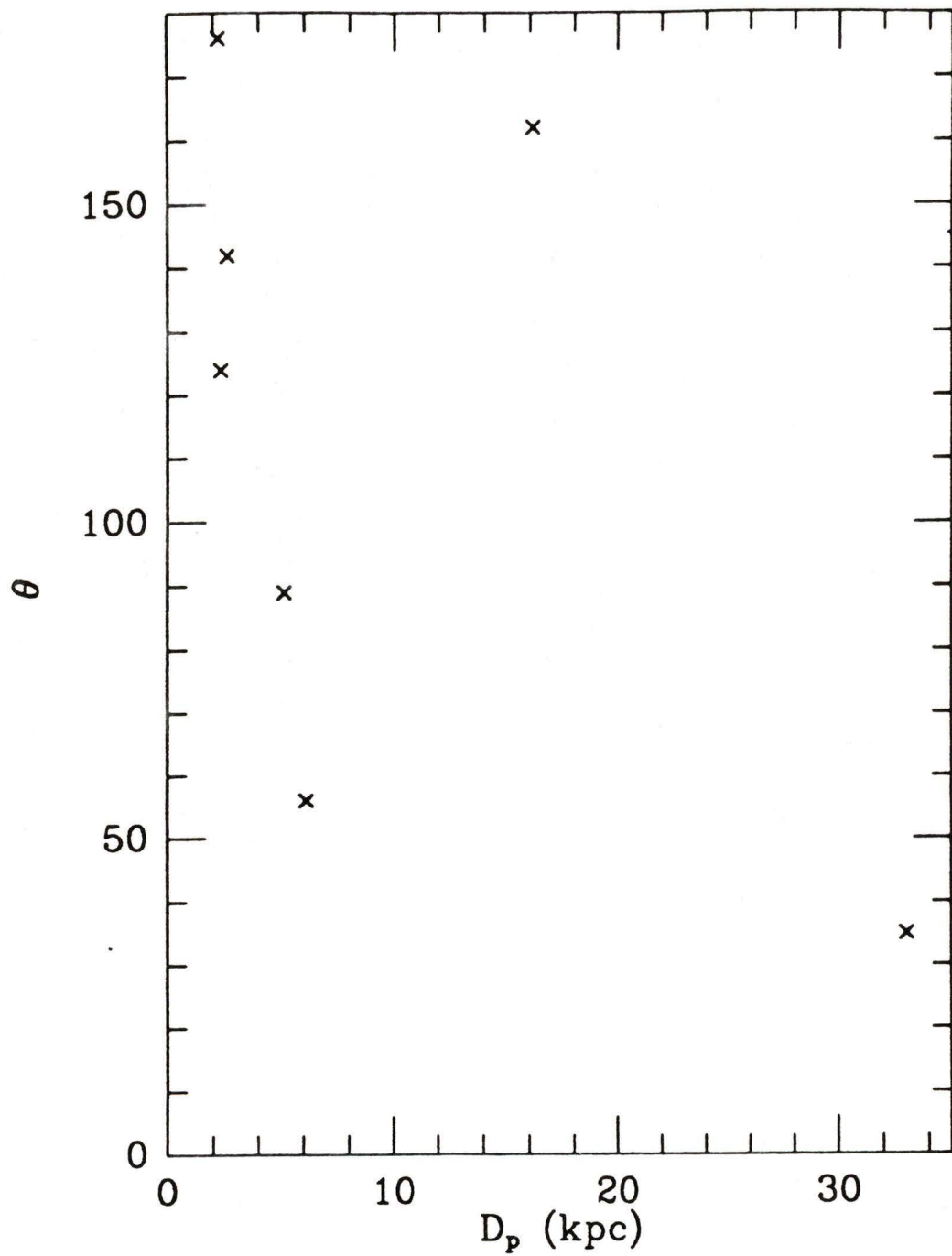


Figure 65: No correlation of the orientation of the semi-major axis with projected galactocentric distance is observed for M31 globular clusters of this work. The linear-correlation coefficient is 0.33

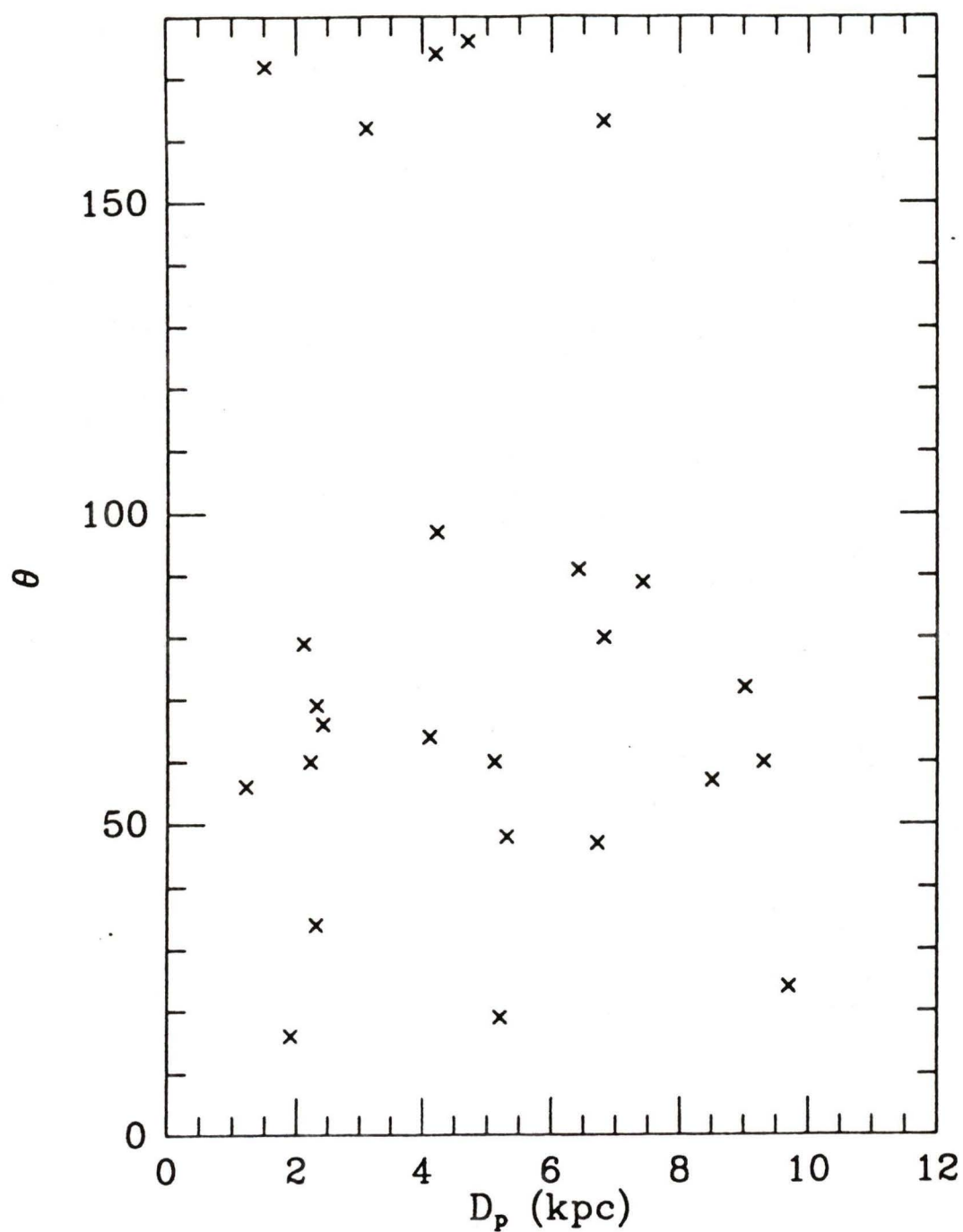


Figure 66: No correlation of the orientation of the semi-major axis with projected galactocentric distance is observed for M31 globular clusters measured by SSB. The linear-correlation coefficient is 0.15

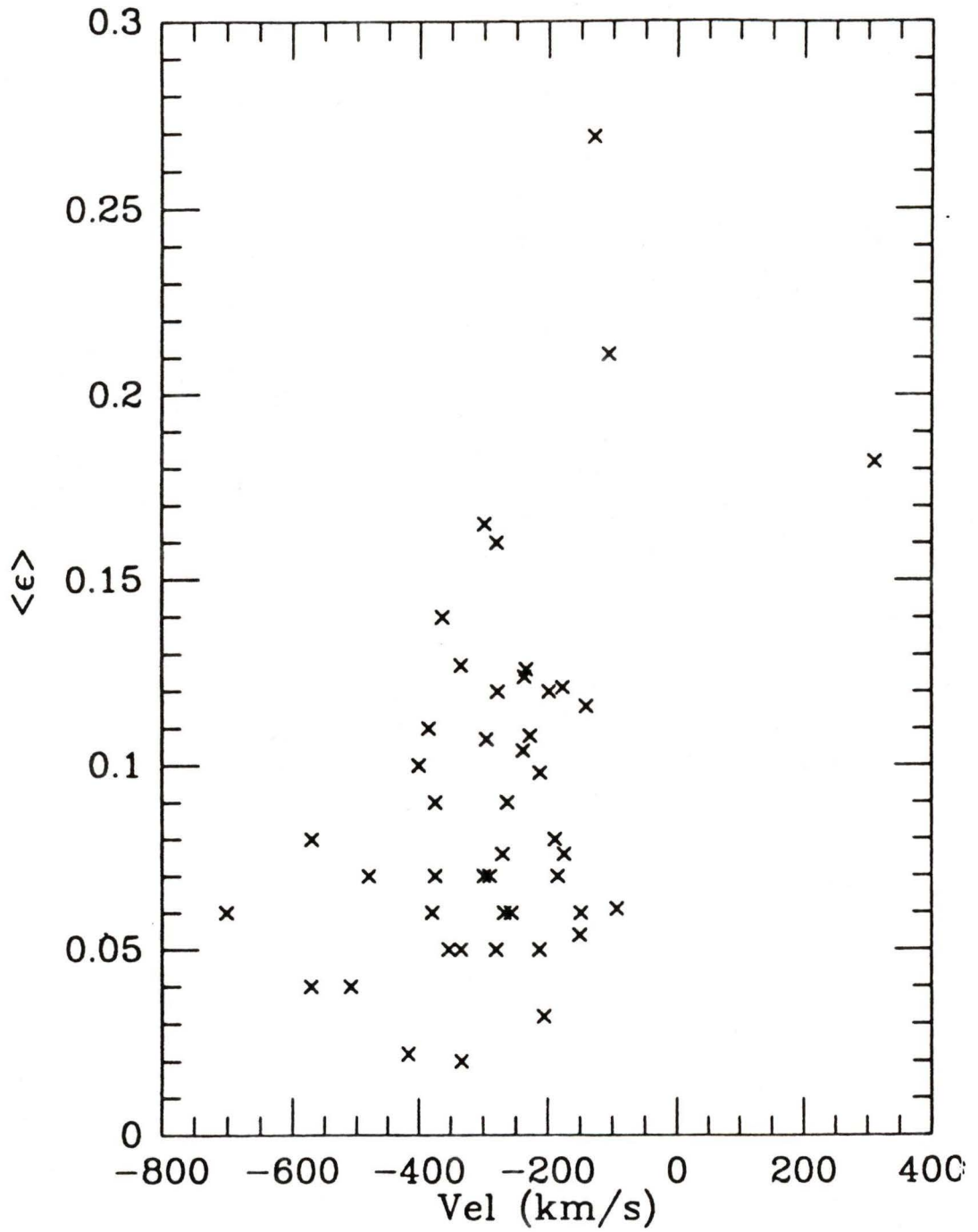


Figure 67: The apparent correlation of ellipticity with radial velocity for the M31 globular cluster sample of SSB is due to selection effects (see text).

flattening may, however, be due to some property of the parent galaxy.

Geisler and Hodge (1980) have suggested the gravothermal shock heating which occurs during each passage of a globular cluster through the disk of its parent galaxy may be important in evaporating outer stars of globulars and reducing their ellipticity. The heating results from the inward acceleration of cluster stars perpendicular to the plane of the galaxy's disk. This acceleration, due to the disk's gravitational force, increases the average stellar energy thus providing an important heat source for the cluster which may increase the rate of evaporation of the outer stars. Since this energy change occurs in a brief transient pulse, the heating process is called a shock and massive galaxies, as a result of their large gravitational force, should therefore have rounder globular clusters. It has been shown that the LMC globular clusters are significantly flatter than the Galactic globulars (White and Shawl 1987; Frenk and Fall, 1982; Geisler and Hodge 1980) and the SMC clusters are significantly flatter than the LMC globulars (Kontizas *et al.* 1985). These results are in good agreement with the gravothermal shock heating hypothesis of Geisler and Hodge (1980) since the LMC is intermediate in mass between the SMC and Milky Way (Allen, 1973). Since the Andromeda Nebula is approximately three times more massive than the Milky Way (Allen 1973), the M31 globular clusters should be at least as round as the Galactic ones if not rounder. However, the M31 clusters have been demonstrated to be more elliptical than those of the Milky Way. Hence the addition of the M31 data makes the hypothesis of Geisler and Hodge that globular ellipticity correlates with parent-galaxy mass untenable. The proposed correlation of globular cluster shape with parent-galaxy luminosity in the sense that luminous galaxies have flatter globulars (van den Bergh and Morbey, 1984) also becomes untenable with the addition of the M31 data since the Milky Way is more luminous than the Andromeda Nebula (Allen 1973).

The complete lack of systematic trends in M31 globular cluster ellipticity suggests axial rotation of a magnitude exceeding that observed for the Galactic clusters may be responsible for the flattening of the globulars associated with the Andromeda Galaxy. However, the numerical simulations of Aarseth and Binney (1978) demonstrate that for galaxies and clusters of galaxies, elliptical surface density contours will result from the collapse of initially aspherical slowly (or non-) rotating clouds. Davis *et al.* (1983) provide observational evidence which supports the conclusion that there need not be a connection between flattening and rotation for elliptical galaxies. Specifically, Davis *et al.* observe faint elliptical galaxies are rapidly rotating but no correlation between galaxian ellipticity and magnitude is observed. The authors claim observational errors and selection effects are not responsible for the absence of a correlation and suggest an anisotropic velocity dispersion is responsible for the flattening of these galaxies. This lack of a systematic trend of ellipticity with magnitude is reminiscent of the M31 globular cluster data and King (1962) has demonstrated that the brightness distribution of elliptical galaxies are adequately represented by a King globular cluster model. Therefore, an anisotropic velocity dispersion may be responsible for the anomalous flattening of the globular clusters associated with the Andromeda Galaxy but spectroscopic data of these M31 globulars are required to verify cluster axial rotation is not the dominant flattening mechanism.

Chapter 7

Conclusion

In conclusion, the mean ellipticity and orientation of the semi-major axis of each M31 globular cluster listed in Table 1 was measured by an isophotal technique and is within the limiting value obtained by an intensity-weighted moment technique. The ellipticity of this sample of globulars ranges from 0.024 to 0.212 with a mean of 0.097 ± 0.017 which is in good agreement with previous work. A variation of ellipticity with cluster radius is not observed and it is suggested the variation reported by Lupton (1989) is the result of seeing effects.

The distribution of ellipticities measured for the globular clusters associated with the Andromeda Galaxy resembles that of the LMC globulars and a two-tailed Kolmogorov-Smirnov test confirms the M31 globulars are more elliptical than those of the Galaxy. This observation contradicts the hypotheses of Geisler and Hodge (1980) and of van den Bergh and Morbey (1984) that globular cluster shape correlates with parent-galaxy mass and luminosity. Selection effects and observational errors are not responsible for the measured flattening of the M31 globulars.

The absence of systematic trends in the ellipticity of M31 globular clusters with

observed globular properties cannot be attributed to projection effects and suggests axial rotation of a magnitude exceeding that observed for the Galactic globulars and/or anisotropic velocities of cluster stars is responsible for the measured shape of M31 globulars. The compilation of rotational velocity data for these M31 clusters with measured ellipticities would determine whether axial rotation is the dominant flattening mechanism as it appears to be for the globular clusters associated with the Milky Way Galaxy.

References

- Aarseth, S. J. and Binney, J. 1978, *M.N.R.A.S.*, **185**, 227.
- Allen, C. W. 1973 *Astrophysical Quantities*, third edition (London: Athlone Press) p. 287.
- Battistini, P., Bònoli, F., Braccisi, A., Pecci, F. Fusi, Malagnini, M. L. and Marano, B. 1980, *A. A. Suppl. Ser.*, **42**, 357.
- Bracewell, R. N. 1965, in *The Fourier Transform and its Applications*, (New York: McGraw-Hill) p. 194.
- Christian, C. 1988, *CFHT Information Bulletin*, No. 18, p. 4.
- Cowley, A. P. and Burstein, D. 1988, *A. J.*, **95**, 1071.
- Crampton, D., Cowley, A. P., Schade, D., and Chayer, P. 1985, *Ap. J.*, **288**, 494.
- Davis, R. L., Efstathiou, G., Fall, S. M., Illingworth, G., and Schechter, P. L. 1983, *Ap. J.*, **266**, 41.
- Eccles, M. J., Sim, M. E., and Tritton, K. P. 1983, in *Low Light Level Detectors in Astronomy*, (Cambridge: Cambridge University Press) p. 4.
- Elson, R. A. W. and Walterbos R. A. M. 1988, *Ap. J.*, **333**, 594.
- Frenk, C. S. and Fall, S. M. 1982, *Mon. Not. R. astr. Soc.*, **199**, 565.

- Geisler, D. and Hodge, P. 1980, *Ap. J.*, **242**, 66.
- Geyer, E. H. and Richtler, T. 1981, in *Astrophysical Parameters for Globular Clusters*, I.A.U. Colloquium No. 68 (NY: L. Davis Press Inc.), p. 239.
- Geyer, E. H., Hopp, U. and Nelles, B. 1983, *Astron. Astrophys.*, **125**, 359.
- Hartwick, F. D. A. and Sargent, W. L. W. 1974, *Ap. J.*, **190**, 283.
- Hodge, P. W. 1981, *Atlas of the Andromeda Galaxy*, (Seattle: University of Washington Press).
- Hubble, E. 1932, *Ap. J.*, **76**, 44.
- Huchra, J., Stauffer, J., and van Speybroeck, L. 1982, *Ap. J.*, **259**, L57.
- King, I. 1961, *A. J.*, **66**, 68.
- King, I. 1962, *A. J.*, **67**, 471.
- Kontizas, E., Dialetis, D., Prokakis, T., and Kontizas, M. 1985, *Astron. Astrophys.*, **146**, 293.
- Kontizas, E., Kontizas, M., Sedmak, G., and Smareglia, R. 1989, *A. J.*, **98**, 590.
- Lupton, R. L. 1989, *A. J.*, **97**, 1350.
- Lupton, R., Gunn, J. E. and Griffin R. F., 1985, in *Dynamics of Star Clusters*, I.A.U. Symposium 113, ed. by J. Goodman and P. Hut (Dordrecht:Reidel), p. 93.
- Mayall, N. U. and Eggen, O. J. 1953, *P.A.S.P.*, **65**, 24.)
- Mayor, M. *et al.* 1984, *A. A.*, **134**, 118.
- Meylan, G. and Mayor, M. 1985, in *Dynamics of Star Clusters*, I.A.U. Symposium 113, ed. by J. Goodman and P. Hut (Dordrecht: Reidel), p. 93.
- Meylan, G. and Mayor, M. 1986, *A. A.*, **166**, 122.
- Press, W. H., Flannery, B. P., Teukolsky, S. A., and Vetterling W. T. 1986, *Numerical Recipes*, Cambridge University Press, p. 100.
- Pritchett, C. 1979, *Ap. J.*, **231**, 354.
- Pritchett, C. J. 1988, private communication.

- Pritchett, C. and van den Bergh, S. 1984, *P.A.S.P.*, **96**, 804.
- Pryor, C., McClure, R. D., Fletcher, J. M., Hartwick, F. D. A., Kormendy, J. 1986, *A. J.*, **91**, 546.
- Richer, H., 1988. private communication.
- Sargent, W. L. W., Kowal, C. T., Hartwick, F. D. A., and van den Bergh, S. 1977, *A.J.*, **82**, 947.
- Spasova, N. M., Staneva, A. V., 1984. *Sov. Astron. Lett.*, **10**, 114.
- Spasova, N. M., Staneva, A. V. and Golev, V. K. 1988, in *The Harlow-Shapley Symposium on Globular Cluster Systems in Galaxies*, I.A.U. Symposium 126, J. E. Gindlay and A. G. Davis Philip eds., (Dordrecht: Kluwer), p. 569. (SSG)
- Staneva, A. V., Spasova, N. M., and Baev P. V. 1985, *Sov. Astron. Lett.*, **11**, 375. (SSB)
- Trumpler, R.J. and Weaver H.F. 1953, in *Statistical Astronomy* (NY:Dover) p.29.
- Valdes, F., Tyson, J. A., and Jarvis, J. F. 1983, *Ap. J.*, **271**, 431.
- van den Bergh, S. 1967, *A. J.*, **72**, 70.
- van den Bergh, S. 1969, *Ap. J. Supp. Ser.*, **19**, 145.
- van den Bergh, S. 1983, *P.A.S.P.*, **95**, 839.
- van den Bergh, S. 1984, *P.A.S.P.*, **96**, 329.
- van den Bergh, S. and Morbey, C. L. 1984 *Ap. J.*, **283**, 598.
- van den Bergh, S. 1988, private communication.
- Vaucouleurs, G. de. 1953, *Mon. Not. R.A.S.*, **113**, 134.
- Vetešnik, M. 1962, *Bull. Astron. Inst. Czech.*, **13**, 180.
- White, R. E., and Shawl, S. J. 1987, *Ap. J.*, **317**, 246.

Appendix A

Seeing is defined as the blurring of an image caused by turbulence in the atmosphere. It is measured by the apparent angular size of a point source; in this context, a star is effectively a point source (Eccles *et al.* 1983). Seeing is only one source of blurring that produces the spread in stellar images; spherical aberration and guiding errors also contribute to the smearing of point sources. Henceforth, the combined effects of seeing, spherical aberration, and guiding which contribute to the blurring of stellar images will be referred to as “seeing”. Seeing is a rather variable quantity even at one site and must be computed individually for each observation.

Initially the seeing for each CCD frame was determined by visually examining the intensity profile of the brightest stellar images that were unsaturated and relatively isolated on the frame. The width of the profile was measured (in pixels) at an intensity corresponding to one half the maximum intensity of the profile. This measurement is often referred to as *the full width at half maximum* (FWHM). This visually determined width is an estimate of the seeing for the frame. A more accurate determination of the seeing was obtained using this estimate as an initial

guess in the stellar photometry reduction program DAOPHOT written by P. B. Stetson of the Dominion Astrophysical Observatory. This program computes the seeing for a frame by iteratively fitting the stellar intensity profile with a Gaussian distribution and computing the FWHM (in pixels) of the Gaussian in the axial directions of the frame once the residuals have been minimized. Ideally the seeing in each direction is equivalent but as Table 2 indicates, the seeing for the data in this project can be described by an elliptical Gaussian function.

In order to convert the seeing from units of “pixels”, or CCD “picture element” units, to arcseconds, the scale of the telescope must be determined for the detector employed when the observations were made.

In this project, the 1985 observations were made using the RCA1 (320×512) CCD detector at the prime focus of the 3.6m Canada-France-Hawaii Telescope. At this focus, the focal ratio, or f-ratio, is 4.2 (Pritchett, 1988) (*i.e.*, the ratio of the focal length of the objective mirror to the aperture of the telescope is 4.2) hence the focal length of the objective is 15.12m. Each pixel of the RCA1 CCD detector is $30 \mu\text{m}$ in length on each side. Therefore, the angular size of one side of a pixel is 1.98×10^{-6} radians or 1.14×10^{-4} degrees which corresponds to ~ 0.4119 seconds of arc on the sky .

The 1987 observations employed in this project were obtained using the RCA2 (640×1024) CCD detector at the prime focus of the 3.6m Canada-France-Hawaii Telescope. Each pixel of this detector is $15 \mu\text{m}$ in length on each side – half that of the RCA1 detector. The 1987 observations were averaged over 2×2 blocks of pixels so that the size of the frame was reduced by a factor of two resulting in a frame 320×512 square pixels which corresponds to the 1985 data. The angular size of one side of a pixel of these reduced frames is therefore the same as that derived for the RCA1 detector, namely ~ 0.4119 seconds of arc on the sky.

Appendix B

Since the identification of the globular clusters in each of the CFHT CCD frames could not be determined using the known celestial coordinates of the clusters but instead were based upon visual comparisons with published finder charts, it was suggested (Richer, 1988) that the objects identified for this project as globular clusters associated with M31 may be foreground optical double stars or background elliptical galaxies, not clusters. To test the first of these hypotheses, the objects which were assumed to be M31 globular clusters were subjected to the star-finding routines of DAOPHOT, a digital stellar photometry reduction program written by Peter B. Stetson of the Dominion Astrophysical Observatory. If the supposed globular clusters were indeed two (or more) foreground stars whose images overlapped producing an extended image on the CCD frame, then the star-finding routines of DAOPHOT would identify the centroid and the magnitude of two (or more) objects within the image. For each observation, the stellar images used to determine the characteristic point-spread function for the frame were completely subtracted by the reduction program indicating the stellar profile was accurately determined. In addition, each image assumed to be a globular cluster was found to have only

one centroid. Therefore, none of the images identified as M31 globular clusters are overlapping foreground stellar images.

The radial velocity data of Huchra *et al.* (1982) addresses the the possibility that the presumed clusters listed in Table 1 are background elliptical galaxies. Their data have demonstrated that these nebulous objects are indeed associated with the Andromeda Nebula and are not background elliptical galaxies.

Appendix C

The integrated intensity of each M31 globular cluster observed in this project was computed using aperture photometry on the CCD frame. That is, the median background intensity in an annulus around the globular was subtracted from the cluster's image prior to integration. The number of photons per pixel (f_2) corresponding to unit apparent magnitude, m_2 , was determined using

$$m_1 - m_2 = -2.5 \log \frac{f_1}{f_2}$$

where m_1 is the integrated apparent magnitude of the globular (Crampton *et al.* 1977) and f_1 is the integrated flux measured. Using this magnitude scale, the number of photons per pixel corresponding to a given magnitude was then computed using the above equation, where f_1 was the scale of the frame for unit apparent magnitude m_1 , and m_2 was the given magnitude. This flux was converted to a brightness using the linear scale of the detector, namely, 0.4119 arcsec/pixel (see Appendix A).

Vita

Surname: **Markle**

Given Names: **Laura Marie**

Place of Birth: **Scarborough, Ontario**

Date of Birth: **November 7, 1962**

Educational Institutions Attended:

York University, Ontario

1982 to 1987

University of Victoria, B. C.

1987 to 1989

Degrees Awarded:

B. Sc. 1987

York University

B. Ed. 1987

York University

Partial Copyright License

I hereby grant the right to lend my thesis (the title of which is shown below) to users of the University of Victoria Library, and to make single copies only for such users, or in response to a request from the library of any other university or similar institution, on its behalf or for one of its users. I further agree that permission for extensive copying of this thesis for scholarly purposes may be granted by me or a member of the university designated by me. It is understood that copying or publication of this thesis for financial gain shall not be allowed without my written permission.

Title of Thesis:

The Ellipticity of M31 Globular Clusters



Author: Markle, Laura Marie

November 1, 1989

Appendix D

The orientation of the semi-major axis of the ellipse, which was fitted to an isophote by the image processing software package R2D2, was measured in an anticlockwise direction from the horizontal axis of the CCD frame. In order to determine the orientation with respect to the celestial coordinate system, the direction of increasing right ascension and declination were determined for each CCD frame by visual comparison of the frames with the finder charts in Hodge's Atlas of the Andromeda Galaxy (1981). The offset of the CCD axes from these celestial axes was computed for the 1985 data of this project using the orientation of G1 measured by Pritchett and van den Bergh (1984). For the 1987 data of this project, the orientation of G217 measured by Spassova *et al.* (1988) was used to compute the offset. Addition of these offsets to the orientations measured by the isophotal method described in Section 3.1.1 permitted the measurement of the orientation of the semi-major axis from North through East on the sky.